

REPORT DOCUMENTATION PAGE

Form Approved
OMB No. 0704-0188

Public reporting burden for this collection of information is estimated to average 1 hour per response, including the time for reviewing instructions, searching existing data sources, gathering and maintaining the data needed, and completing and reviewing the collection of information. Send comments regarding this burden estimate or any other aspect of this collection of information, including suggestions for reducing this burden, to Washington Headquarters Services, Directorate for Information Operations and Reports, 1215 Jefferson Davis Highway, Suite 1204, Arlington, VA 22202-4302, and to the Office of Management and Budget, Paperwork Reduction Project (0704-0188), Washington, DC 20503.

1. AGENCY USE ONLY (Leave blank)	2. REPORT DATE	3. REPORT TYPE AND DATES COVERED
	February 16, 1996	Final 4/01/93 - 9/30/95
4. TITLE AND SUBTITLE		5. FUNDING NUMBERS
Advanced X-ray Analytical Instrumentation Research		2301/BS 61102F
6. AUTHOR(S)		Dr. Brian J. Cross, Dr. Jonathan A. Kerner and Mr. Edward D. Franco
7. PERFORMING ORGANIZATION NAME(S) AND ADDRESS(ES)		8. PERFORMING ORGANIZATION
Advanced Research and Applications Corporation (ARACOR) 425 Lakeside Drive Sunnyvale, California 94086-4701		AFOSR-TR-96 0110
9. SPONSORING/MONITORING AGENCY NAME(S) AND ADDRESS(ES)		10. SPONSORING/MONITORING AGENCY REPORT NUMBER
Air Force Office of Scientific Research - NE 110 Duncan Avenue, Suite B115 Bolling AFB, DC 20332-0001		F49620-93-C-0013
11. SUPPLEMENTARY NOTES		
12a. DISTRIBUTION/AVAILABILITY STATEMENT		
APPROVED ROB PUBLIC RELEASE: DISTRIBUTION UNLIMITED 19960320 072		
13. ABSTRACT (Maximum 200 words)		
<p>The purpose of this research was to build prototype x-ray fluorescence instrumentation to support the manufacturing of semiconductor devices for Air Force and commercial interests. Thin films of titanium nitride were chosen as the target application upon which the requirements and design were based. A state-of-the-art energy-dispersive x-ray detector and electronics were used, and a new design of focusing wavelength-dispersive spectrometer, with limited scanning, was built. Multilayer optics were designed and fabricated to distinguish nitrogen from titanium x rays.</p> <p>Another key requirement was for small-spot analysis. A new transmission-target x-ray tube, which used a thin-film molybdenum anode deposited directly on a thin beryllium window, was built and tested. We were able to demonstrate the predicted performance for analysis spot diameters of about 1 mm, with a performance gain of about ten times any other instrumentation currently available. This tube technology was operated at low power (only 10 watts), with a close-coupled geometric design that more than compensated for the low source flux. We have demonstrated the analysis of single-layer thin TiN films to the requirements of industry.</p>		
14. SUBJECT TERMS		15. NUMBER OF PAGES
Semiconductor thin-film analysis, x-ray fluorescence, transmission-target x-ray tube, energy-dispersive spectrometer, wavelength-dispersive spectrometer		126
		16. PRICE CODE
17. SECURITY CLASSIFICATION OF REPORT	18. SECURITY CLASSIFICATION OF THIS PAGE	19. SECURITY CLASSIFICATION OF ABSTRACT
UNCLASSIFIED	UNCLASSIFIED	UNCLASSIFIED
20. LIMITATION OF ABSTRACT		
UNCLASSIFIED		

SECURITY CLASSIFICATION OF THIS PAGE

CLASSIFIED BY:

DECLASSIFY ON:

SECURITY CLASSIFICATION OF THIS PAGE

FINAL TECHNICAL REPORT

Advanced X-ray Analytical Instrumentation Research

Prepared for:

AFOSR/NE Directorate of Physics and Electronics
Project Officer: Dr. Howard Schlossberg
110 Duncan Avenue, Suite B115
Bolling AFB, DC 20332-0001

Prepared by:

Dr. Brian J. Cross, Dr. Jonathan A. Kerner and Mr. Edward D. Franco
Advanced Research and Applications Corporation (ARACOR)
425 Lakeside Drive
Sunnyvale, California 94086-4701

February 1996

The views and conclusions contained in this document are those of the authors and should not be interpreted as necessarily representing the official policies or endorsements, either expressed or implied, of the Air Force Office of Scientific Research or the U.S. Government.

ARACOR PROPRIETARY INFORMATION-NOT TO BE DISTRIBUTED WITHOUT PRIOR PERMISSION



ARACOR

425 LAKESIDE DRIVE, SUNNYVALE, CA 94086

TABLE OF CONTENTS

<u>Section</u>		<u>Page</u>
1.0	INTRODUCTION.....	1
1.1	PROGRAM OBJECTIVES.....	1
1.2	PROGRAM MODIFICATIONS.....	1
1.3	BACKGROUND.....	2
1.3.1	Semiconductor Analysis Requirements.....	2
1.3.2	Previous Work.....	7
2.0	TECHNICAL APPROACH.....	9
3.0	ALTERNATIVE APPROACHES	11
3.1	X-RAY SOURCE DESIGN.....	11
3.1.1	Requirements	11
3.1.2	Summary of Previous Work.....	11
3.1.3	Make/Buy Decision.....	13
3.2	MULTILAYER OPTICS.....	14
3.2.1	Requirements	14
3.2.2	Summary of Previous Work.....	15
3.2.3	Make/Buy Decision.....	16
3.3	ADVANCED DETECTORS.....	16
3.3.1	Requirements	16
3.3.2	Summary of Previous Work.....	17
3.3.3	Make/Buy Decision.....	18
4.0	INSTRUMENTATION DESIGN	20
4.1	X-RAY SOURCE DESIGN.....	20
4.1.1	Thermal Calculations.....	20
4.1.2	Materials Issues	26
4.1.3	Specifications.....	29
4.2	WAVELENGTH-DISPERSIVE SPECTROMETER.....	29
4.2.1	Optic Design	29
4.2.2	Multilayer Design	29
4.2.3	Detector Design	39
4.2.4	Motion Control and Design Layout.....	42
4.2.5	Specifications.....	45
4.3	ENERGY-DISPERSIVE SPECTROMETER.....	45
4.3.1	Detector Design and Fabrication.....	45
4.3.2.	Specifications.....	48

TABLE OF CONTENTS (continued)

<u>Section</u>	<u>Page</u>
4.4 INTEGRATION ISSUES.....	50
4.4.1 Source-Sample-Spectrometer Geometries.....	50
4.4.2 Materials Issues	52
4.4.3 System Integration and Design.....	54
4.4.4 System Specifications.....	54
5.0 INSTRUMENTATION ASSEMBLY AND EVALUATION.....	56
5.1 X-RAY SOURCE	56
5.1.1 Subcontract Work.....	56
5.1.2 Component Evaluation	57
5.1.3 System Integration.....	72
5.2 WAVELENGTH-DISPERSIVE SPECTROMETER.....	72
5.2.1 Subcontract Work.....	72
5.2.2 Detector Evaluation	72
5.2.3 Multilayer Evaluation	76
5.2.4 Optic Evaluation and System Integration	82
5.3 ENERGY-DISPERSIVE SPECTROMETER.....	88
5.3.1 Purchased Components.....	88
5.3.2 System Integration.....	89
5.3.3 EDS Detector/Electronics Evaluation.....	91
5.4 SYSTEM INTEGRATION.....	92
5.4.1 Integration Issues	92
5.4.2 System Performance	96
6.0 RESULTS AND DISCUSSION	103
6.1 SYSTEM EVALUATION.....	103
6.1.1 Performance vs. Requirements	103
6.2 APPLICATION TO SEMICONDUCTOR MATERIALS' ANALYSIS	107
6.2.1 Application to TiN Analysis.....	107
6.2.2 Quantitative TiN Thin-Film Analysis.....	107
7.0 CONCLUSIONS AND RECOMMENDATIONS.....	112
8.0 REFERENCES.....	114

LIST OF FIGURES

<u>Figure Caption</u>	<u>Page</u>
1.3.1 Calculated nitrogen fluorescence production efficiency	5
1.3.2 Dependence of the measurement time on the sample analysis size	5
2.1 System cross-sectional view, with WD and ED spectrometers	9
2.2 System plan view.....	10
3.1.1 Anode assembly for Herglotz tube.....	13
4.1.1 Temperature profile for Mo on Be at 1, 5, and 10 watts.....	21
4.1.2 Model to calculate temperature distribution in anode/window.....	22
4.1.3 Temperature in anode as a function of radius and depth, z	23
4.1.4 Evaporation rate of Mo as a function of temperature.....	23
4.1.5 Peak temperature on anode as a function of power loading and spot diameter.....	24
4.1.6 Heat transfer from chamber lid as a function of temperature difference.....	26
4.1.7 Concept for transmission target x-ray tube close coupled to sample.....	26
4.1.8 Geometry governing spot size and flux onto sample	27
4.1.9 Penetration of electrons into an anode at 20 kV	28
4.2.1 Reflectivity of Monel/Ti multilayer measured at Cu-K.....	32
4.2.2 Parameter fits to four diffraction orders from Monel/Ti multilayer	33
4.2.3 Simulated reflectivity for multilayer of Figure 4.2.1.....	34
4.2.4 Measured 1st order integrated reflectivity as a function of d-spacing.....	34
4.2.5 Reflectivity of Monel/Ti multilayer at N-K and Ti-L.....	35
4.2.6 Plot used to infer reflectivity for a single wavelength of x rays	36
4.2.7 Roughness of multilayer deduced from reflectivity at N-K.....	36
4.2.8 Reflectivity of Ux/Sc multilayer measured at Cu-K.....	37
4.2.9 Simulated reflectivity for multilayer of Figure 4.2.8.....	38
4.2.10 Reflectivity of Ux/Sc multilayer at N-K and Ti-L.....	39
4.2.11 Detector and window used for detection of N-K, Ti-L.....	40
4.2.12 Melting point of boron hydrides as a function of boron content	40
4.2.13 Density of boron hydrides as a function of boron content	41
4.2.14 Predicted thickness dependence of boron hydride transmittance.....	41
4.2.15 Geometry describing transmittance of window support grid	42
4.2.16 Layout for wavelength dispersive spectrometer.....	43
4.2.17 Design drawing of wavelength dispersive spectrometer	44

LIST OF FIGURES (continued)

<u>Figure Caption</u>	<u>Page</u>
4.3.1 Required Si(Li) detector geometry	46
4.3.2 Actual geometry of Si(Li) detector.....	47
4.3.3 Detection efficiency of Si(Li) detector for low-energy x rays	49
4.4.1 Top down view of available ports on vacuum chamber.....	50
4.4.2 Detail of sample stage translation.....	51
4.4.3 Vacuum system for main chamber and proportional counter detector.....	53
5.1.1 System used to regulate hydrogen flow through the brazing chamber.....	56
5.1.2 Geometry used for initial evaluation of focal spot size and count rate.....	58
5.1.3 Focal spot size derived from edge scan of silicon wafer.....	58
5.1.4 Change in focal spot with polarity change on filament.....	59
5.1.5 Spectrum of aluminum plate taken with PIN-diode detector.....	59
5.1.6 Spectrum of silicon wafer taken with PIN-diode detector.....	60
5.1.7 Count rate dependence on voltage and anode current.....	60
5.1.8 Count rate for silicon normalized to power loading on anode.....	61
5.1.9 Comparison of measured and predicted count rates from samples.....	62
5.1.10 Monte-Carlo simulation of 20 kV electrons in a 1-micron molybdenum film	63
5.1.11 Monte-Carlo simulation of 25 kV electrons in a 1-micron molybdenum film	64
5.1.12 Count rate variation from tube #1 run overnight.....	65
5.1.13 Photograph of x-ray tubes and pinhole photo geometry	66
5.1.14 Pinhole photographs of focal spot for the three x-ray tubes.....	66
5.1.15 Appearance of a copper peak in the silicon spectrum from x-ray tube #3	67
5.1.16 Comparison of x-ray tube efficiencies for exciting Ni-K x rays	68
5.1.17 Possible mechanism for effect of filament polarity on observed count rates.....	69
5.1.18 Count rate vs. tube current at 5 kV for tube #3	70
5.1.19 Tube stability test.....	71
5.2.1 Detector bias as a function of operating gas pressure.....	73
5.2.2 Predicted efficiency of detector for soft x rays.....	73
5.2.3 Initial spectrum collected with detector using TiN sample	74
5.2.4 Change in peak position with mirror substrate covered with copper foil	75
5.2.5 Predicted scatter of bremsstrahlung from x-ray tube to detector	76
5.2.6 Parameters used to model angle of incidence along surface of multilayer.....	77
5.2.7 Required d-spacing gradient for Monel/Ti multilayer.....	78
5.2.8 Sputtered profiles determined from optical density measurements.....	79
5.2.9 Diffraction pattern from thin W film used to determine film thickness.....	79
5.2.10 Convergence of d-spacing to desired value for Monel/Ti multilayer.....	80

LIST OF FIGURES (continued)

<u>Figure Caption</u>	<u>Page</u>
5.2.11 Redesign of multilayer d-spacing gradient.....	81
5.2.12 Convergence of d-spacing for W/Ti multilayer.....	82
5.2.13 Schematic diagram showing adjustments used to align optic mirror.....	82
5.2.14 Predicted efficiency of Monel/Ti with incorrect d-spacing gradient	83
5.2.15 Spectra collected with Monel/Ti multilayer from silicon and TiN	84
5.2.16 N-K and Ti-L emission from TiN sample measured with Si(Li) detector.....	85
5.2.17 Predicted efficiency of W/Ti multilayer with d-spacing offset	87
5.2.18 Spectra collected with W/Ti multilayer from silicon and TiN.....	88
5.2.19 Combined N-K and Ti-L signal as a function of mirror position.....	89
5.3.1 Fe-55 spectrum for Amptek XR-100T PIN-diode detector.....	93
5.4.1 Variation in signal with stage height and detector position.....	94
5.4.2 Variation in signal near stage maximum.....	95
5.4.3 Scans of copper wire at three different stage heights	95
5.4.4 Extrapolation of sample spot size as a function of stage position.....	96
5.4.5 Dependence of sample spot size on sample-collimator separation.....	97
5.4.6 Estimate of focal spot diameter derived from measured spot diameters	97
5.4.7 Spectra of boron and carbon samples collected with the Si(Li) detector	98
5.4.8 Spectrum from silicon wafer fit by a gaussian curve	98
5.4.9 Geometry used to predict count rates for C-K and Si-K fluorescence	99
6.1.1 Comparison of figure of merit for prototype instrument with goal	104
6.2.1 Plot of Ti-K count rate against TiN film thickness.....	110
6.2.2 TiN/Si repeatability measurements.....	111

LIST OF TABLES

<u>Table</u> <u>Caption</u>	<u>Page</u>
1.3.1 Representative TiN-based semiconductor thin-film stacks.....	3
4.1.1 Analogy between electrostatics and heat flow as per Condon (1967)	21
4.1.2 Summary of tube and power supply specifications.....	29
4.2.1 Cu-K diffractometer data for Ux/Sc multilayers	37
4.2.2 Reflectivity data for Ux/Sc multilayers using N-K radiation.....	38
4.2.3 Specifications of the wavelength-dispersive spectrometer	45
4.3.1 Specifications of Si(Li) detector.....	48
5.2.1 WDS throughput calculations	86
5.4.1 Si(Li) detector efficiency based on Si deadlayer and Au contact absorption	99
5.4.2 Count rates from silicon.....	100
5.4.3 Count rates from carbon	100
5.4.4 Combined T-L and N-K count rates from thick TiN sample.....	101
5.4.5 N-K count rates from thick TiN sample.....	101
6.1.1 Predicted vs. measured WDS system performance for N-K x rays.....	106
6.2.1 Analysis of Intel TiN standards	108
6.2.2 Measured count rates of Ti-K in TiN thin films on silicon.....	109

ACKNOWLEDGMENTS

There are many people who contributed to the success of this project. In particular, I would like to acknowledge the help from the co-authors of this report. Dr. Jonathan Kerner was responsible for most of the modeling tasks in this project, the experimental multilayer fabrication and characterization, and was the major contributor for the characterization of the x-ray tube and wavelength-dispersive spectrometer, and the complete integrated system. Mr. Edward Franco also made many contributions to the overall project, particularly in the design of the wavelength-dispersive spectrometer. Other valuable contributors included Dr. Jerel Smith, who did most of the early modeling of the heat-flow characteristics of transmission-target tubes, and Mr. Cary Pincus who contributed to the design of the x-ray tube. Mr. William Hershy (ARPES), the subcontractor for the tube fabrication, made major contributions to the final design and fabrication of the x-ray source. Also, I would like to acknowledge the help from Mr. Howard McKinney in collaborating on the design of the wavelength-dispersive spectrometer. This project was also supported by Ms. Genevieve Tewart and Ms. Evelyn Hoover, who provided invaluable support for graphics and editing services.

I would also like to thank the many people in industry (IBM, Motorola, Intel, et al.) who contributed to the requirements from semiconductor companies for technology to monitor their fabrication process. In particular, Dr. Mike Madden and Mr. Bruce Fruechting, of Intel, made many suggestions, and kindly loaned ARACOR some calibrated TiN thin-film standards for analysis with our prototype instrument.

FOREWORD

This Final Technical Report was prepared by Advanced Research and Applications Corporation (ARACOR), Sunnyvale, California, for the Air Force Office of Scientific Research (AFOSR). It documents work done under AFOSR Contract Number **F49620-93-C-0013**, and ARACOR Project Number **898**, for the project period of April 1, 1993 through September 30, 1995.

This project was entitled "Advanced X-ray Analytical Instrumentation," and was under the direction of Dr. Brian J. Cross, the Principal Investigator.

This program was conducted under the cognizance of Dr. Howard Schlossberg, of the AFOSR/NE, Directorate of Physics and Electronics, 110 Duncan Avenue, Suite B115, Bolling AFB, DC 20332-0001.

EXECUTIVE SUMMARY

The purpose of this research was to define, design and implement prototype x-ray fluorescence (XRF) instrumentation to support the manufacturing of semiconductor devices for Air Force and commercial interests. Thin films of titanium nitride (TiN) were chosen as the target application upon which the requirements and design were based. Complex film stacks, containing more than one titanium-based layer, required that low-energy XRF measurements (of Ti-L and N-K x rays) be made, in addition to the more conventional higher-energy Ti-K x rays. The measurements of the latter were achieved with a state-of-the-art Si(Li) detector and electronics. A new design of focusing wavelength-dispersive spectrometer (WDS), with a limited scanning range (to distinguish N-K from Ti-L x rays) was required to support the remaining measurements. Multilayer optics were designed, fabricated and installed in the WDS, and then used to test the feasibility of this application. Although the method has not yet been proven, it appears plausible that this technique can be used to make these measurements in the future.

Another key requirement was for small-spot analysis (with a diameter in the range 0.1 mm to 1 mm). A new design of transmission-target x-ray tube was built and tested. This comprised a thin-film molybdenum anode deposited directly on a thin beryllium window. Although the small-spot requirements have not yet been met, we were able to demonstrate the predicted performance for analysis spot diameters of about 1 mm, using the Si(Li) detector, with a performance gain of about ten times any other instrumentation currently available. This tube technology was operated at the relatively low power of only 10 watts, with a close-coupled geometric design that more than compensated for the low-flux source. We have demonstrated the capability to analyze single-layer thin TiN films to the requirements of industry.

Future work is required to complete the demonstration of the WDS unit, and to reduce the size of the x-ray source on the target. We believe both of these steps are still feasible, and would then expect to be able to demonstrate complete feasibility for the TiN and other semiconductor thin-film applications. We believe this will play an extremely important role in the future development of custom or standard semiconductor devices for both military and commercial applications. After demonstrating this feasibility, we then expect to move to *in-situ* analysis, in the future, to provide the real-time feedback necessary for new and special process development.

This work involved, in addition to the Principal Investigator, the following ARACOR personnel: Dr. Jonathan Kerner, Mr. Edward Franco, Dr. Jerel Smith and Mr. Cary Pincus. In addition, this project was supported by the subcontractors, Mr. William Hershyn (ARPES), for tube developments, and Mr. Howard McKinney (McKinney and Associates), for development of the wavelength-dispersive spectrometer. At this time, no publications have been submitted, or papers presented.

1.0 INTRODUCTION

1.1 PROGRAM OBJECTIVES

The original goal of the three-year program was to develop and demonstrate innovative x-ray analytical instrumentation concepts responsive to Air Force needs. The specific technical objectives of the program were defined as follows:

Objective 1. Demonstrate an x-ray analytical instrument concept that non-intrusively measures the thickness and constituency of thin-film structures used in semiconductor devices.

Objective 2. Demonstrate an x-ray non-destructive inspection instrument concept that detects incipient corrosion in airframe structures.

Technical objective 1 was targeted at BPSG (boro-phospho-silicate glass) films. These program objectives were modified, as described in Section 1.2. The sole deliverable from this project is this Final Report describing the approach, progress to date, and experimental results obtained using the instrumentation.

1.2 PROGRAM MODIFICATIONS

The objectives for this program were changed from the original ones for several reasons. First and foremost, the project funding was cut from a three-year to a one-year program. As a result of this, Objective 2 (building a corrosion monitor prototype) was dropped from the program. These changes in the objectives were reviewed with Dr. Howard Schlossberg, the AFOSR Project Officer, in 1994.

Secondly, discussions with Wright Patterson Air Force Base and commercial semiconductor suppliers (e.g., Intel, IBM and Motorola), showed that the primary industry interest was no longer in BPSG films, but other key semiconductor films such as Ti, TiN, W and AlCu. Consequently, our approach was to include a solid-state energy-dispersive detector, as well as a wavelength-dispersive (WD) spectrometer using x-ray multilayer optics. Although the WD spectrometer can be used for boron and oxygen analysis (with a change in the multilayer optic), the primary objective was now targeted at the analysis of TiN thin films, where the stoichiometry (as determined from the nitrogen K α signal) is important as well as film thickness. The WD spectrometer optics are required to discriminate the wavelengths of nitrogen K α and titanium L α x rays. The remaining elements in the thin films were to be determined from a state-of-the-art solid-state energy-dispersive detector.

The key objective for this project remained that of demonstrating an XRF (x-ray fluorescence) instrument prototype for the measurement of the thickness and composition of semiconductor thin films on silicon wafers. The key research components of this project included the development of an innovative miniature transmission x-ray tube with a small-spot (less than 1 mm) collimation, a wavelength-dispersive spectrometer for light-element analysis using multilayer optics, and the evaluation of state-of-the-art low-energy x-ray detectors.

1.3 BACKGROUND

1.3.1 Semiconductor Analysis Requirements

The electronics' requirements of Air Force weapons systems are satisfied by a large variety of high performance logic and application-specific integrated circuit (ASIC) components used for computing, communication, radar sensing, optical imaging, and signal and data processing. In an era of shrinking defense budgets, these integrated circuits must be developed rapidly and manufactured cost-effectively, even for low-volume production. These requirements are not well served by traditional IC manufacturing, oriented to large volume production of single commercially attractive IC's. In response to these requirements, a joint Air Force/DARPA flexible manufacturing initiative has led to the development of a revolutionary technology for one-wafer-at-a-time semiconductor fabrication, that supports versatile and rapid IC prototyping and manufacturing [Kinsella, 1991, Doering, 1994]. New process-control sensors play a key role in the flexible manufacturing concept [Davis, 1992]. These sensors need to be implemented close to the production line (rather than in a quality assurance laboratory), to provide near real-time measurements that allow fabrication processes to be developed, maintained, or rapidly changed in response to IC production needs.

The required tolerances, on process control for semiconductor fabrication, are extremely tight. For example, the 1σ requirements for the thickness control of some films can be as little as a few Ångstroms (less than 1% relative). The properties of these films are extremely dependent on their thickness (and sometimes their composition). For example, the anti-reflective properties of TiN films change dramatically with a change of a few Ångstroms in thickness. The re-flow properties of BPSG films are very dependent on the composition (boron and phosphorus). The uniformity of W and Al-Cu films are critical to forming a constant film resistivity for different die across a silicon wafer. Also, the end-user value of an 8-inch microprocessor wafer can be as high as \$250,000 and so the consequences of a process out of control can be very expensive, especially where products consist of many layers to form a complex integrated circuit.

XRF has emerged as a leading metrology tool for the semiconductor industry, to measure the thickness and composition of opaque metal films. The competitive technique of film-resistivity

measurement is not a direct thickness gauge and requires contact with the film. The non-destructive and non-contact nature of XRF analysis is favored for measurement on device wafers where contact with the wafer could damage the film and also generate particles. In addition, XRF is capable of measuring transparent film thicknesses (to sub-monolayer levels) and the composition of thin or bulk materials.

We decided to focus on TiN films, to specify the analytical requirements of this prototype system. This was because of the importance of this material to the semiconductor industry, and because of several technical challenges in their analysis. TiN is both a common diffusion barrier layer, and an anti-reflective coating, used during the inter-level metallization part of semiconductor fabrication. Table 1.3.1 shows representative metal-layered structures found in current semiconductor fabrication.

Table 1.3.1. Representative TiN-based semiconductor thin-film stacks.

Case 1.	TiN	400 to 600 Å	Anti-reflection coating (ARC)
	Al	3,000 to 15,000 Å	Contacts
	Ti	1,000 to 1,500 Å	Sacrificial Diffusion Layer
Case 2.	TiN	400 to 600 Å	Anti-reflection coating
	Ti	1,000 to 1,500 Å	Contacts
	TiN	400 to 600 Å	Passive Diffusion Barrier Layer
	Al	3,000 to 15,000 Å	Contacts

For device or patterned wafers, these measurements need to be made on bonding pads or special test structures (e.g., in areas on the wafer known as “scribe” lines). Microprocessors have about 400 pads with 50 µm spacing; DRAMs have about 16 pads with 500 µm spacing; ASICs are between these values (although more like the DRAM case). Thus the measurement spot should ideally be about 30 µm to meet the microprocessor test requirements using bond pads. Larger measurement spot sizes are possible for DRAMs and monitor wafers. Also, it is possible to use the scribe lines (areas between die), where there are typically areas available of about 150 µm or more in width, and much greater length. Therefore the initial goal was for an analysis spot size of 30 µm or less in diameter, with the next best solution of 150 µm or less.

In addition to the sample analysis area, the precision is extremely important. As noted previously, it is important to know the thickness with a precision of better than 1% (1σ) to control the index of refraction of the anti-reflection TiN layer. Wafer throughput is also a key factor in determining the economic viability of a production tool. Currently, these measurements are performed, using XRF, within a time period of 100 to 200 seconds. For a thin TiN film of 400 Å, a 1% precision translates into 4 Å. However, we had been advised that next generation products could require a

precision of 0.25% (i.e., 1 Å in 400 Å), so our initial target was to try and achieve this level of precision.

For the ideal case (where the signal is much greater than the background), it follows from Poisson counting statistics that to obtain a measurement precision of 1 Å in a 400-Å film, using N-K x rays, that a total of about 160,000 nitrogen counts are required. Poisson counting statistics are simply the square root of the total number of counts. Assuming for these thin films that the number of N-K counts is linear with thickness, then the relative (1σ) precision from 160,000 counts is 0.25%, which would correspond to 1 part in 400 for thickness.

Required Signal Levels

Based upon some initial considerations of optimum geometries for the x-ray source and detectors, an estimate was made of the expected signal levels. The work presented here is, again, for the nitrogen signal, as it was perceived to be the most difficult to successfully accomplish. The N-K signal level, S , was estimated with the following formula:

$$S = \Phi \times \Omega_S \times \Omega_D \times \epsilon_D \times P \times \tau \quad (1.3.1)$$

where: S is the signal level (counts)
 Φ is the fluorescent production efficiency at constant voltage (photons/sr²-W-s)
 Ω_S is the source solid angle subtended by the sample (steradians)
 Ω_D is the sample solid angle subtended by the detector (or collection optic) (steradians)
 ϵ_D is the detector efficiency factor
 P is the x-ray tube power (W)
 τ is the measurement time (s)

The N-K fluorescence-production efficiency, F , was estimated, as a function of voltage, using an incident spectrum composed of Mo-L characteristic emissions and bremsstrahlung predicted for the transmission-anode tube designs developed later in this project. This production efficiency is shown in Figure 1.3.1 for 400- and 600-Å-thick TiN films.

The dependence of the measurement time, to achieve 1 Å precision on the desired sample examination area, for two detector solid angles, is shown in Figure 1.3.2 under the following (initial) assumptions:

- 1) Tube Power: 10 W, limited by our objective to rely on passive cooling.
- 2) Detector efficiency: 30%, including absorption by state-of-the-art thin windows.
- 3) Source-to-sample distance: 4.5 mm, representative of the close-coupled source-to-sample distances made possible with a transmission anode x-ray tube.

- 4) TiN film thickness: 600 Å, a value between the range of 400 to 1000 Å typical of these applications.
- 5) Tube potential: 10 kV.

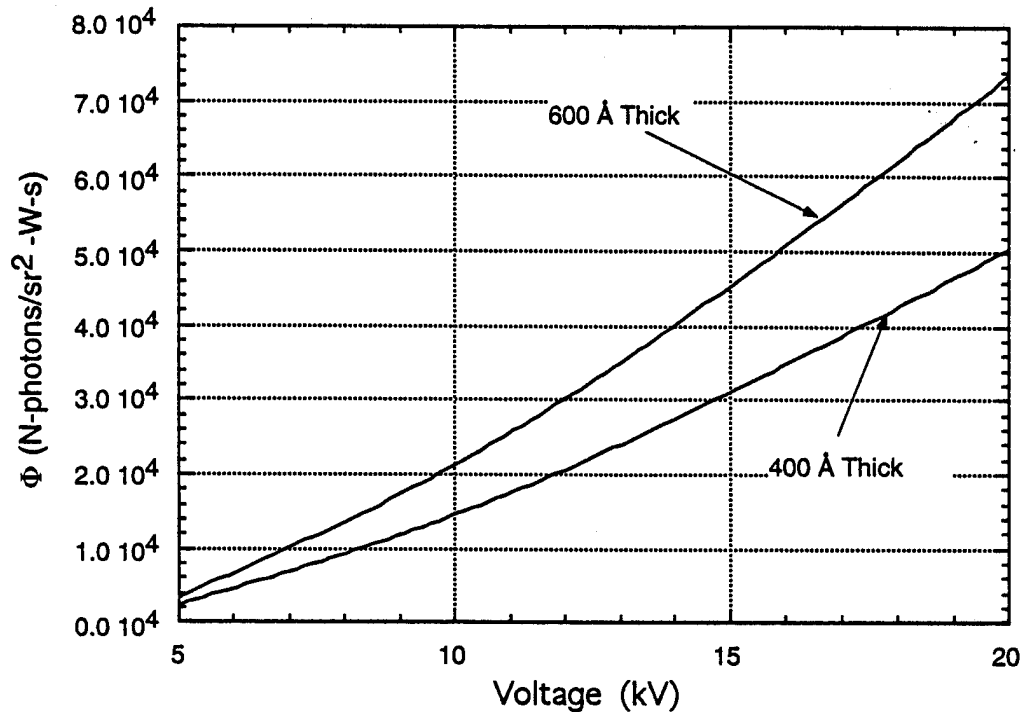


Figure 1.3.1. Calculated nitrogen fluorescence production efficiency.

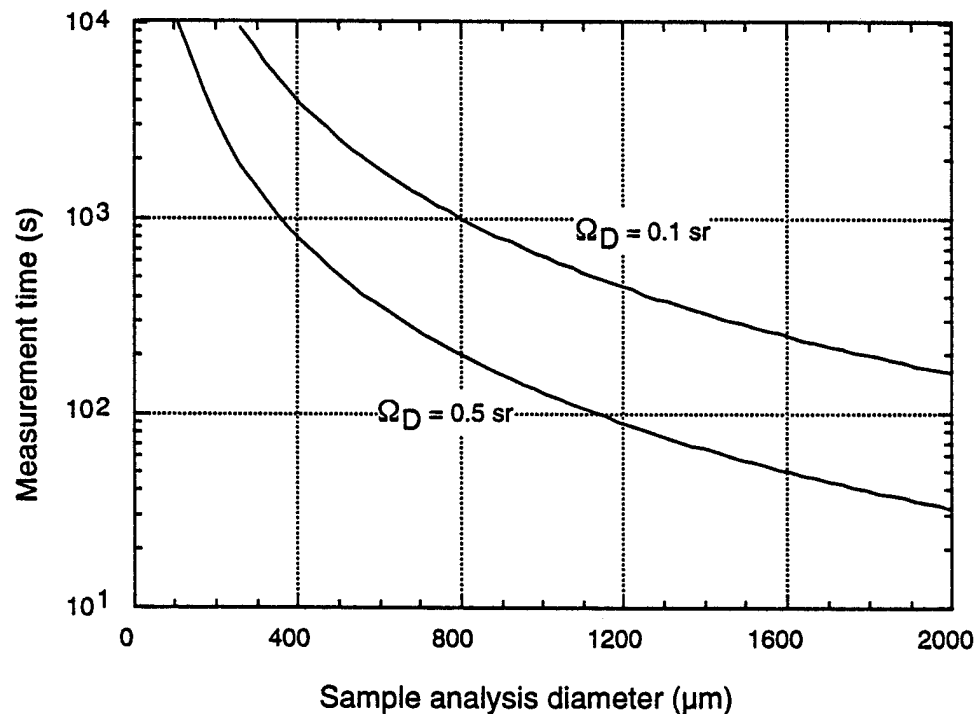


Figure 1.3.2. Dependence of the measurement time on the sample analysis size.

As Figure 1.3.2 shows, a sample analysis spot between 1 to 2 mm in diameter was predicted to achieve a measurement time between 100 and 200 seconds. Further, this measurement requires a large collection solid angle, greater than 0.1 sr. This project considered how to maximize the source count rate and solid angle, and also how to achieve the x-ray detection solid angle shown in Figure 1.3.2, using either an ED detector or WD collection optics.

Methodology

There are two basic approaches to determining the thickness of a thin film: (1) the emission method, based on the intensity of the fluorescence emission from the specimen, and (2) the absorption method based on the attenuation by the thin film of the fluorescent radiation from the substrate. We planned to primarily use method (1) to determine the film thickness and so we used this approach to determine the resulting precision of the measurement. If we assume that a monoenergetic radiation is producing the fluorescence, then the thickness of the thin film can be estimated with the following equations:

$$t = - \frac{2.3026}{\rho \mu^*} \log \left(1 - \frac{I_t}{I_\infty} \right) \quad (1.3.2)$$

where:

$$\mu^* = \frac{\mu_1}{\sin \Psi_1} + \frac{\mu_2}{\sin \Psi_2} \quad (1.3.3)$$

where: μ_1, μ_2 are the mass absorption coefficients of the thin film for the incoming radiation (at a wavelength λ_1) and the fluorescence radiation (at a wavelength λ_2).
 Ψ_1, Ψ_2 are the incident and take-off angles (degrees)
 ρ is the density of the thin film (g/cm^3)
 I_t is the fluorescence intensity from the thin film (c/s)
 I_∞ is the fluorescence intensity from a bulk sample (c/s)

Equation 1.3.2 can accommodate the presence of overlayers by correcting I_t for the reduction in the incoming and the fluorescent radiation by absorption in the overlayers.

The precision associated with the determination of the thickness of each layer was estimated by applying the method of propagation of errors to Equation 1.3.2, corrected for the presence of overlayers. The precision was estimated as a function of I_t, I_∞ , and the thickness of each of the overlayers. For the simple case of no overlayers, the precision reduces to Equation 1.3.4:

$$\sigma_t = \frac{2.3026}{\rho \mu^*} \left(\frac{1}{1 - \frac{I_t}{I_\infty}} \right) \frac{1}{I_t} \left(\frac{I_t}{I_\infty} \right) \sqrt{ \frac{I_t}{T} \left(1 + \frac{I_t}{I_\infty} + \frac{I_B}{I_t} \right) } \quad (1.3.4)$$

where: T is the counting time associated with the measurement (s)
 I_B is the background count rate under the peak (c/s).

1.3.2 Previous Work

This is a very brief review of some recent and relevant work in XRF analysis, with a particular emphasis on light-element and semiconductor thin-film analysis. A comprehensive literature review is beyond the scope of this report.

XRF has been applied to many different semiconductor, and related, thin-film materials. Recent instrumentation [e.g., Cross, 1988, and Zaitz, 1994] has shown that both near-line and on-line *ex-situ* [Kevex, 1994] measurements of film thickness and composition are possible in or near a semiconductor "fab." To date, very little work has been done on applying XRF for on-line *in-situ* process control of semiconductor fabrication. ARACOR evaluated the concept of using XRF (and XRD), for on-line analysis in the semiconductor fab environment, under an (D)ARPA SBIR Phase I contract [Franco, 1992].

Most of this recent work has been associated with the measurement of opaque metallic films, but other transparent films, such as BPSG, have been analyzed for both the thickness and composition [Madden, 1989].

Analytical methods and algorithms have been established for extracting reliable film thickness and composition from the x-ray intensities for each element, without the need for multiple standards and more-traditional multiple least-squares calculations [e.g., de Boer, 1990, Huang, 1991, and Feng, 1992]. Film thickness precisions (1σ) are typically in the range of 0.1 to 1% relative [Cross, 1988, and Kevex, 1994], with accuracies of about $\pm 3\%$ or better [Huang, 1991]. Compositional accuracies can be $\pm 1\%$ by weight or better [Huang, 1991].

In order to measure uniformity of films, or perform selected-area analysis, the analysis beam should be small. However, "focusing" x rays have always proved to be extremely difficult, because of the short wavelengths involved. So far, attempts using optics such as multilayers [e.g., Marshall, 1986, and Schuster, 1995] or capillary optics [e.g., Carpenter, 1991, and Hoffman, 1994] have only been useful as a research tool, and not found application within a commercial instrument.

Commercial microbeam XRF instrumentation, introduced in the last decade, has been based on a simpler approach of aperturing the x-ray beam. Although this approach is very inefficient, the technology has been used successfully for process development and control in semiconductor and related industries [e.g., Cross, 1988, and Zaitz, 1994]. Small-area XRF analysis has become a valuable tool for understanding and controlling the deposition process over the entire area of a 200-

mm wafer. For process control, current instrumentation is limited to a spot size of about 2 mm, in order to have sufficient signal to meet the industry requirements for precision. For light-element (low-energy) analysis, the spot size has to be even larger (at least 1 cm diameter), making uniformity or localized measurements almost impossible [Kirby, 1993].

2.0 TECHNICAL APPROACH

The technical approach for this project, after re-aligning the objectives from the original proposal, was to design and build a new low-power x-ray tube which could be closely coupled to a semiconductor wafer, and still allow good access of x-ray spectrometers to provide efficient capture of fluorescent x rays from the sample. This approach, of close coupling the tube to the sample, was chosen as more likely to provide a versatile and higher flux source than a more powerful source, further from the sample, and focused by an active optic such as an LSM or capillary optic. Since no source was commercially available that met the design objectives, a new tube was designed and built in conjunction with a subcontractor.

In order to meet the needs of semiconductor thin-film analysis, it was necessary to design both an energy-dispersive and a wavelength-dispersive spectrometer (WDS). The energy-dispersive spectrometer (EDS) was specially designed to be mechanically compatible with the x-ray tube, to provide the optimum solid angle for x-ray capture. It was configured with a new window material to provide optimum analysis of light elements. The EDS was used to perform most of the data acquisition. In order to satisfy the need of analyzing TiN films, it is necessary to be able to distinguish Ti $\text{L}\alpha$ from $\text{N K}\alpha$ x rays, and so the WDS was designed to perform this specific analysis, using a custom-designed and fabricated multilayer optic.

The conceptual design of the system is shown in the cross-sectional view in Figure 2.1, and a plan view in Figure 2.2.

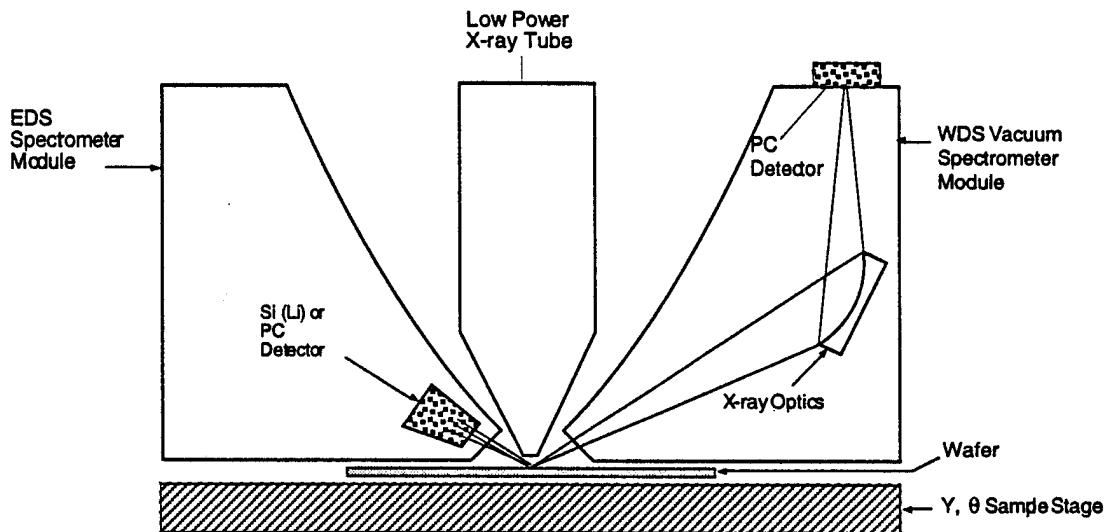


Figure 2.1. System cross-sectional view, with WD and ED spectrometers.

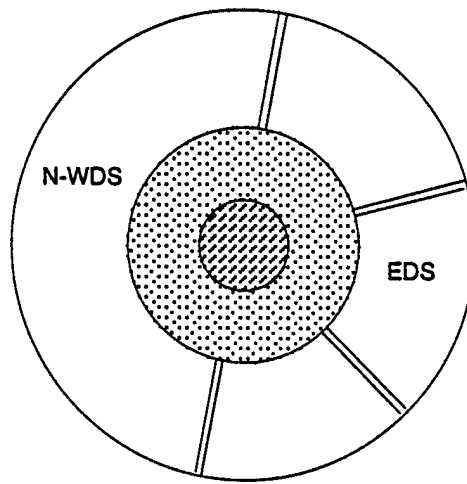


Figure 2.2. System plan view.

3.0 ALTERNATIVE APPROACHES

3.1 X-RAY SOURCE DESIGN

3.1.1 Requirements

The requirements for the x-ray tube, used on this project, included several conflicting needs. Since the funding was also limited, some approaches were taken which were simpler in order to fit the available budget.

The first requirement was that the tube had to be sealed for robustness in a semiconductor analytical environment (i.e., high vacuum is incompatible with high throughput analysis). However, a window on the tube reduces the transmission of low-energy characteristic and bremsstrahlung radiation which is critical for light-element fluorescence.

Secondly the x-ray source, at the anode, had to be as small as possible to produce a small spot on the sample (this is true even for a pinhole aperture, otherwise divergence causes the collimated beam at the sample to be much larger than the aperture). The conflict here was that the smaller the x-ray source, at the anode, the more stringent becomes the local cooling requirements. Also, the x-ray source had to be as close to the sample as possible, again for coupling efficiency. However this need conflicts with the need to get the spectrometers closely coupled, because of the limited solid angle available above the sample.

Also, one had to design a tube which had good efficiency for excitation of both light elements such as carbon and nitrogen, but could also be used to excite titanium, tungsten and copper x rays in the range 1 through 15 keV.

In the end, the decision was made to use a transmission-target tube, with a narrow cone geometry at the target end, which could be closely coupled to the sample. The collimation would be built into the tube assembly, although it could be interchanged for different analytical spot sizes. A thin layer of molybdenum was chosen as the target material, to be directly deposited on the beryllium window. A diamond window was rejected because of the relatively high absorption for low-energy x rays.

3.1.2 Summary of Previous Work

Because of the need to do small-area analysis, most of the commercial tubes, designed for x-ray spectroscopy, were not suitable for this project. They often have anode spot sizes greater than 10 mm. Alternatively, microfocus tubes are generally used for radiography where the requirement for a very stable source intensity is not so stringent. The other problem with most commercial tube

designs is that the ability to closely couple the sample to the x-ray source (i.e., at the anode) is difficult because of the large anode-to-window distances, and because most tubes are not designed for close packing with the sample and other equipment such as x-ray spectrometers.

For example, the Omicron spectrometer [Cross, 1988] uses a minifocus side-window tube and integrated power supply which is difficult to get close to the sample, while still leaving room for one, let alone multiple spectrometers. Consequently the anode-to-sample distance on that system is over 50 mm. Alternative end-window tubes are available which are more compatible with multiple spectrometer configurations [e.g., Toda, 1994, and Vrebos, 1993], but they are not usually designed with small-spot sizes at the anode. Using these types of tubes, with typical anode spot sizes of 10 mm or more, with a sub-millimeter collimator, would be very inefficient without some active focusing optic.

Because of the lack of a suitable commercial x-ray tube, it was decided that a specially-designed tube would have to be built. Since ARACOR did not have the necessary resources to complete this part of the project, a subcontractor was used to help complete the design and fabricate some x-ray tubes for testing. In arriving at the final configuration of the tube, several older tube designs were evaluated. We rejected all the designs where the tube is continuously pumped, because of the requirement for a sealed source, as noted previously. The two designs, closest to the final configuration selected, included one originally proposed and built by Herglotz [1973] and another built by Hershyn [1975], and also described by Zulliger[1975].

Both Herglotz and Hershyn were contacted in order to determine their progress since these papers were published, and to solicit ideas for future work, with a potential role for consulting. Herglotz had retired, and had also discussed this design with Hershyn many years earlier in an effort to commercialize the design. Herglotz had a patent granted [Herglotz 1971] which has subsequently expired. The essential element is the anode construction shown in Figure 3.1.1.

This tube is potentially very efficient because the electrons impacting the steep conical taper, and which are scattered, have multiple opportunities to cause the generation of x rays. Also, the x-ray anode area is “fore-shortened” by the view in front of the tube, allowing for potentially higher powers of excitation. The whole end-piece is covered by a thin Be window and a foil of the same material as the cone.

One of the disadvantages of this design was that the source was presented as a ring (in the form of a “donut”) rather than a point source. Also, the thin-foil (typically 5-micron-thick Cu) was separately mounted from the 125-micron thick Be window. The main issue with the design, according to Hershyn, was the difficulty in getting the electrons to travel down the narrow cone shown in Figure 3.1.1. Hershyn had independently developed his own transmission-target tubes, at several companies, with a far simpler concept of a Be window coated with anode material, with

the idea that the electron gun would be responsible for the focusing of the electrons, and not the anode itself. Also, he had developed direct brazing techniques which would allow efficient coupling of the anode/window into the tube body for efficient cooling. The main difference, from his previous designs, would be the need to bring other detectors and optics close to the analysis area, requiring a steeper take-off angle of the tube body, resulting in different cooling requirements as well as possible space-charge effects internally.

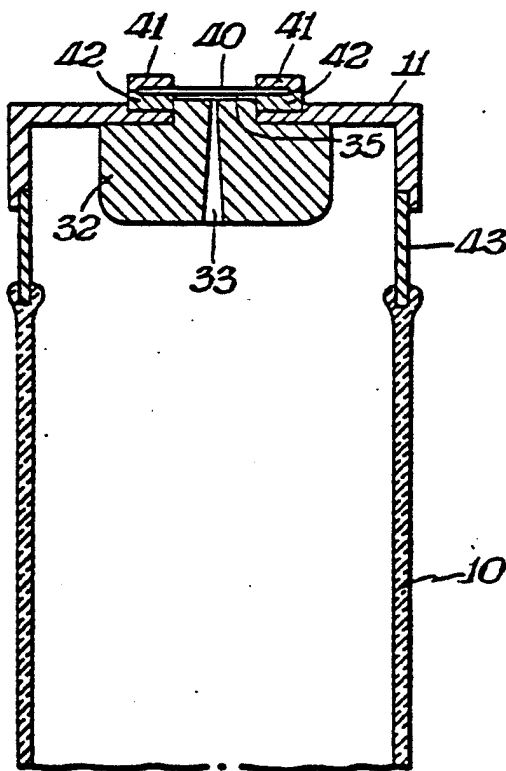


Figure 3.1.1. Anode assembly for Herglotz tube [Herglotz, 1971].

3.1.3 Make/Buy Decision

ARACOR has no experience in building commercial x-ray tubes, and a major issue was to produce a tube which could be manufactured reliably and inexpensively. Therefore, it was decided that we would use an outside supplier to fabricate the tube for this program. Several manufacturers were contacted (e.g., Kevex, TruFocus and X-Tech/Oxford) and asked to quote on the subcontract. Of these, the only company that put in a reasonable bid for the contract was TruFocus. However, at the time, they were in the process of relocating their factory, and were unsure about committing to a delivery schedule. When the opportunity to directly contract with Bill Hershyn (of ARPES) became available, this was an obvious choice because of his prior expertise in this area. Because of budget constraints, we decided to set up Hershyn's equipment at ARACOR to reduce the overall

cost to the program. This also gave us a better opportunity to monitor progress and provide early feedback on the tubes.

3.2 MULTILAYER OPTICS

3.2.1 Requirements

The requirements for the multilayer optics were driven by the requirements for the WD spectrometer. We used the application of measuring the composition and thickness of thin TiN films to set these requirements. These thin films are important materials used as anti-reflection coatings or as a passive diffusion barrier layer during the fabrication of integrated circuits. In these applications, the TiN film is typically 400- to 1000-Å thick.

Quantitative analysis of light elements is complicated by the inefficiency with which the characteristic x-ray fluorescent signals are produced and detected. This is a consequence of their low fluorescence yields and their relative inefficiency for absorption of higher-energy radiation. The detection of N-K and Ti-L radiation also requires very thin detector windows to minimize the absorption of radiation. Another factor, in the window fabrication, is that the carbon content should be low, as the C-K absorption edge is just below the x-ray energies of interest and, therefore, strongly absorbs this radiation. In this application, these factors are compounded by the thin film nature of the samples which further reduces the signal level. This places a premium on achieving large collection solid angles, and in using an efficient detector.

A second requirement results from the presence of peak overlaps between N and Ti that complicate the determination of the elemental composition of these films. The Ti L_1 and L_2 emissions at 395 and 401 eV interfere with the N $K_{\alpha 1}$ and $K_{\alpha 2}$ emissions at 392.3 eV. Simulations, using the computer code DTSA V2.0.1 [Fiori 1993], indicate that these two Ti-L emissions will be about 33% of the intensity of the N-K emissions from TiN samples.

Quantification of the amount of N present in the TiN sample, as well as measuring the film thickness, requires that we measure both the N and Ti signals. For single-layer TiN films, it is possible to use the Ti-K signal to determine the concentration of Ti present. However, many of the applications in semiconductor fabrication contain multiple layers of TiN or TiN with Ti layers. Consequently, to solve some of these complex problems, the signals from both Ti-K and Ti-L were required. The Ti-K signals could be obtained from the EDS channel, independently of the Ti-L measurements using WDS.

The Ti peaks, that overlap the N-peaks, are obtained by measuring the Ti L_{α} signal at 450 eV and using tabulated relative peak heights (correcting for matrix effects) to estimate the Ti L_1 and L_2 signals under the N peak [Armigliato, 1982]. Rybka and Wolf [1993] give another practical

example of the analysis of a titanium-containing nitride inclusion with an LSM-060 dispersion crystal (a W/Si multilayer with a 2d spacing of 60 Å offered commercially by Osmic). Thus, we needed to measure the x-ray emission over a small wavelength range, sufficient to measure all of the Ti-L and N-K signals. This meant that a scanning WDS system had to be designed, and the optic had to accommodate the varying wavelengths and geometries.

3.2.2 Summary of Previous Work

Key factors affecting the performance of a wavelength dispersive spectrometer (WDS) include the peak reflectivity and angular bandpass of the multilayer deposited on the optic substrate. These factors are, in turn, a function of materials selection and defect control during multilayer deposition. The optimal materials for a given x-ray energy will have the largest possible x-ray scattering contrast between adjacent layers, while minimizing x-ray absorption in the low scatter spacer layer [Spiller and Rosenbluth, 1985]. Practical considerations, such as interdiffusion of adjacent layers, chemical reactivity, and toxicity further limit the choice of materials. Development of multilayers over the past 15 years [Underwood and Barbee, 1981; Henke et al, 1990] have elucidated practical material combinations with the best characteristics for a particular energy range. Typical material combinations include W/C, W/Si, Mo/Si, and Ni/C, consisting of a high atomic number (Z) layer followed by a low Z spacer material.

ARACOR has developed planar DC magnetron-sputtered multilayers which show very low interfacial roughness between layers, a necessary requirement for producing high reflectivity multilayers for analysis of low Z elements. These include combinations such as W/B₄C [Christenson et al., 1991] and W/Mg₂Si [Boher et al., 1992], as well as a trilayer structure, W/C/Mg₂Si (unpublished), in which the additional carbon spacer boosts reflectivity, presumably by reducing interfacial roughness. For the present project, a different range of constituents had to be considered because the common spacer elements of C and B₄C would absorb the radiation of interest (480 - 680 eV) from TiN layers.

Another important parameter governing the efficiency of the multilayer is the smoothness of the substrate material. Relatively inexpensive but smooth substrates are available in the form of thin silicon wafers, used by the semiconductor industry for integrated circuit manufacture. The substrate roughness of ~0.3 nm "prints through" into the overlaying multilayer structure and degrades reflectivity in a well understood manner [Savage et al, 1991; Takacs and Church, 1990]. The drawback of silicon wafers is that they are flat, while an efficient WDS channel requires collection and focusing of x rays in order to gather the fluorescence emitted from the source over a large solid angle.

ARACOR has previously explored the use of bent silicon wafers, but the elastic limit of the silicon precludes their use for the tight radius of curvature required to gather a large solid angle. Electroformed nickel substrates, smoothed with lacquer coatings, have been used at ARACOR for several focusing optics, but the large surface roughness of this substrate (~2.5 nm) would reduce the reflectivity of a deposited multilayer to an insignificant value for the present application. Custom ground and polished aspheric optics have also been used at ARACOR as multilayer substrates for the purpose of collimating x rays, but these tend to be prohibitively expensive. The requirement for a smooth, low-cost, but curved substrate was therefore examined during this project.

ARACOR has developed an expertise in depositing multilayers with accurate d-spacings gradients over the surface of flat and curved substrate materials. The technique involves the iterative design of masks to control the sputter deposition, with measured d-spacing gradients which converge rapidly (usually within 3 iterations) to within 1% of the design specifications. The initial iterations are evaluated by measuring the optical density of deposited films on glass plates, which is much faster to implement than the point-by-point determination of d-spacing gradients with a diffractometer. This capability was instrumental in permitting the design and fabrication of a curved optic at reasonable cost.

3.2.3 Make/Buy Decision

Although there are two commercial suppliers of multilayer optics (Osmic and MOXTEK), we decided to build the optics at ARACOR because of the research nature of this project. Because ours is a research rather than a production facility, in the future it could be worthwhile to contract out this fabrication, if either of the two vendors can meet the required specifications. Also, ARACOR has probably the leading-edge skills in building tailored d-spacing multilayers, whereas the other facilities specialize in more uniform optics. We did, however, evaluate a new nitrogen LSM from MOXTEK, as part of this project, as it appeared to offer some potential benefits, and was made from a patented combination of layers.

3.3 ADVANCED DETECTORS

3.3.1 Requirements

The requirements for detectors for light-element (i.e., low-energy) XRF are primarily the same as those for higher-energy analysis. However, special consideration must be given to the efficiency of detecting low-energy x rays, which primarily means reducing the attenuation between the sample and the detecting element. Of the different factors of concern, the most important are (1) the ability to work in a vacuum environment, to reduce absorption between the sample and the detector, (2) the vacuum-compatible window which protects the detector, and (3) any coatings

which are required to filter out light, or make contact with the detector front surface. For some types of detectors (e.g., Si(Li)), there is sometimes an inactive "dead-layer" region on the surface of the detector which can act as a filter for low-energy x rays, so this is also important for light-element analysis.

At these low energies, there is little concern about x rays completely traveling through the detector, and so once in the detector itself there is little concern. Although count rate is always of concern, from a practical standpoint, the efficiency of generating low-energy x rays is usually so poor, that low count-rate detectors and electronics are sufficient. Of more importance is the signal-to-noise ratio. However, since these same detectors would also be used for higher-energy x-ray detection, it was necessary to consider the possible requirement for high-count-rate data acquisition.

3.3.2 Summary of Previous Work

Since a part of the proposal was to investigate the use of advanced detectors, we spent some time in evaluating a wide variety of different detectors which could be used either for the light-element semiconductor XRF application and/or the corrosion analyzer.

As part of this evaluation of different detectors, we contacted Mr. Pierre Buckens (939 Lee Drive, Menlo Park, CA 94025) to provide a state-of-the-art review of potential detectors. Some of the key points are summarized, and discussed further, in the following section. Another recent review of note, is that by Sareen who looked at energy-dispersive detectors for low-energy applications[Sareen, 1994].

Gas proportional counters have inherent noise-less gain, and the noise due to leakage current is minimal. However, the small number of initial charge carriers has the dominant effect on resolution. They are good for direct detection of low-energy x rays, and have a large effective area. They are also good for relatively high-count-rate non-dispersive applications, where another element (e.g., a crystal) provides the x-ray dispersion. Their efficiency limits their application to about 10 keV, and below.

Of all of the detectors considered for this project, the most mature and advanced are the Si(Li) detectors. Silicon crystal production, and drifting with Li, are routinely available from several commercial suppliers. The noise is typically on the order of 70 eV at LN (liquid nitrogen) temperatures. This noise is determined primarily by the first stage (e.g., JFET) of the amplification circuit. It is possible to operate Si(Li) detectors with good performance at -90°C, which is attainable with 5- or 6-stage Peltier cooling. High-purity Ge (HPGe) detectors are better for higher energy x rays (above 30 keV), but they must be cooled to at least LN temperatures. They also have a more absorbing dead layer, and a thermal shield (e.g., aluminum thin film), which reduces their efficiency for low-energy (less than 1 keV) detection. However, Sareen

believes that, in the future, Ge detectors may improve considerably as the manufacturing process is better controlled, and therefore may supplant Si(Li) detectors for the highest performance applications.

A more recent and promising detector is mercuric iodide. Because of its higher band gap, it has a low leakage current at room temperature. For good resolution it still requires a high-quality cooled FET. The biggest concern with mercuric iodide is in the stability of the material. It is difficult to make pure, although this is now attainable, and trapping sites can suddenly develop, disabling the charge-collection process. Similar detectors can be fabricated from cadmium (zinc) telluride. They have higher noise, due to higher leakage currents, and a more pronounced low-energy tail. They are easier to grow than mercuric iodide crystals, but may suffer from the same stability problems.

A newer detector, that was evaluated carefully, was the silicon avalanche photodiode (APD). These detectors, used primarily for visible light detection, are similar to photodiodes but with internal gain. The gain is very sensitive to temperature and bias variation, and the manufacturing process is not yet mature enough for high-quality x-ray detectors. They also have a thick dead layer which inhibits low-energy x-ray detection. They may be suitable for high bandwidth applications, where they offer the biggest advantage (faster pulse-processing times). Another new detector, only available on a research basis, is the silicon drift chamber. These have a concentric field gradient which channels charge carriers to a small central electrode. The latter is responsible for a lower leakage current and capacitance. The challenge will be to implement an FET suitable for matching the capacitance of this small electrode. In theory, these devices could produce the performance of a Si(Li) detector operating near room temperature, with good low-energy performance—perhaps better than a proportional counter. At this time, these devices are not commercially available.

A simpler detector, that has recently been made available for x-ray applications [Pantazis, 1994], is the silicon pin-diode detector. A good quality 7 mm^2 pin diode has been integrated with an FET and other discrete electronics, including a Peltier cooler, to produce an x-ray detector with a resolution (about 250 eV) which approaches that of Si(Li) detectors, but without the need for liquid nitrogen [Huber, 1994]. For the best performance, the detector assembly is cooled to about -30°C within the TO8 package.

3.3.3 Make/Buy Decisions

After evaluating several different detectors, it was decided that we would use relatively conventional detectors, but fit them with state-of-the-art components (i.e., windows, FETs, etc.). For the WD spectrometer, we had a suitable proportional counter available. In order to analyze nitrogen and other light elements we decided to purchase a boron hydride window, which has

recently been made available for these detectors, from MOXTEK (Salt Lake City, UT). The window was assembled on a silicon grid for support in a vacuum environment.

Again, for the ED spectrometer, we chose to use a conventional Si(Li) detector manufactured by GDE (Princeton, NJ). It is not practical or cost-effective to manufacture these detectors oneself, so it was decided that an outside vendor would be used. The choice of manufacturer was on the basis of price. This detector was also fitted with a state-of-the-art window (in this case a polymer mounted on a silicon grid, also from MOXTEK), which was assembled in the detector by the manufacturer. Electronics were purchased to interface with this detector, as described in Section 5.3.1. The choice of these components was made both on price and performance.

4.0 INSTRUMENTATION DESIGN

4.1 X-RAY SOURCE DESIGN

4.1.1 Thermal Calculations

An initial set of calculations was undertaken to determine an upper limit to the permissible power loading on the anode. This upper limit was conceived to arise from the maximum steady-state temperature of the anode which would allow the anode material to remain in place over the operating lifetime of the x-ray tube, which was assumed to be 2000 hours.

The simplest model assumes the uniform deposition of energy by the electron beam over a circular spot which is large compared to the anode thickness. In steady state, all the power deposited in a spot must be conducted through the spot perimeter (ignoring radiation). The rate of heat flow across the surface at radius, r , is proportional to the temperature gradient, as given by Fourier's Law [Condon, 1967]:

$$P/2\pi rh = -K dT/dr \quad (4.1.1)$$

where P is the deposited power within radius r , h is the anode thickness, T is the temperature at radius r , and K is the thermal conductivity, K , (watts/deg-cm). If we assume that the total power, P_0 , is distributed uniformly over the spot of radius r_0 , so that:

$$P = P_0 (r/r_0)^2 \quad (4.1.2)$$

then integration of Equation 4.1.1 yields a quadratic decrease in temperature out to the edge of the spot:

$$\Delta T_{(\text{in spot})} = -P_0/4\pi h K (r/r_0)^2 \quad (4.1.3)$$

Note that the temperature drop from center to edge of spot ($r = r_0$) is independent of spot radius for a constant power loading. Outside the spot ($r > r_0$) the deposited power is constant, so integration of Equation 4.1.1 yields a temperature which decreases logarithmically with distance from the edge of the spot according to:

$$\Delta T_{(\text{out of spot})} = -P_0/4\pi h K \ln(r/r_0) \quad (4.1.4)$$

From Equations 4.1.3 and 4.1.4, we find that the maximum temperature at the center of the spot will depend on the heat-sink temperature, which is the steady state temperature achieved at the edge of the window. For a very small spot (e.g., $r_0 = 10 \mu\text{m}$), it is important to minimize the effective radius of the surrounding heat sink in order to minimize the temperature drop, ΔT_{window} . To take a specific example, Figure 4.1.1 shows the temperature profile for a molybdenum-coated Be window at 1, 5, and 10 watt power loadings, assuming the steady-state temperature of the heat

sink, located at $r/r_0=200$, is 40° C (e.g., for a $20 \mu\text{m}$ diameter focal spot, the window diameter would be 4 mm).

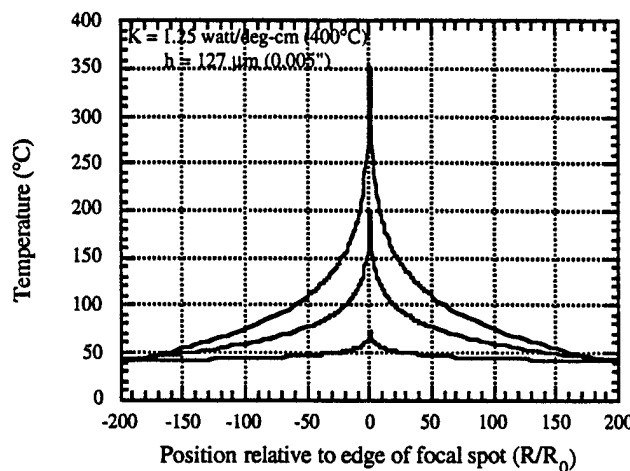


Figure 4.1.1. Temperature profile for Mo on Be at 1, 5, and 10 watts.

The simple model considered above breaks down for a spot which is not large compared to anode thickness. Since we are interested in achieving a $\sim 100 \mu\text{m}$ spot diameter on a 0.005-inch-thick window (127 μm), we must consider the more complicated case which includes a temperature gradient across the anode thickness, which will increase the focal spot temperature over that predicted by the simple model above.

The small spot case is modeled by drawing an analogy between electrostatics and heat flow problems [Condon, 1967], as shown in Table 4.1.1, where the following correspondence holds (L = Laplacian):

$$L(U) + Q/\alpha = 0 \quad (4.1.5)$$

Table 4.1.1. Analogy between electrostatics and heat flow as per Condon [1967].

Variable	Electrostatics	Heat Flow
U	potential, Φ (volts)	temperature, T ($^\circ\text{K}$)
Q	charge source, ρ (C/cm^3)	heat source, Q (watt/cm^3)
α	permittivity, ϵ_0 ($\text{C}/\text{volt}\cdot\text{cm}$)	conductivity, K ($\text{watt}/\text{deg}\cdot\text{cm}$)

The basic approach is to replace the heat source associated with electron deposition in the anode with an equivalent charge source (including any image charges which are required to satisfy the boundary condition of no heat flow across the faces of the anode), and then to numerically integrate the contribution from these fixed charge distributions to find the corresponding electrical

potential distribution at any point within the anode. The resulting potential distribution within the window can be replaced with the equivalent temperature distribution.

To simplify the problem, we assume that the conductivity, K , is a constant rather than varying with temperature. A second good assumption is that the electron beam is deposited in a depth which is small compared to the anode thickness. The boundary conditions for tangential heat flow at the top and bottom of the window are satisfied by the placement of image sources equally spaced above and below the true source, as shown in Figure 4.1.2.

The electrostatic potential due to disks having uniform charge density can then be calculated numerically for any point within the window (horizontal slab). Far from the source (i.e., at large radial distances), the result should match the previously derived Equation 4.1.4, which gives a logarithmic decrease in temperature with radius. This is plausible from the model shown above, since the vertical string of discrete charge sources looks like a continuous line of charge when viewed from afar. A line source of charge gives an electrostatic potential which decreases logarithmically with radial distance [Bull, 1971].

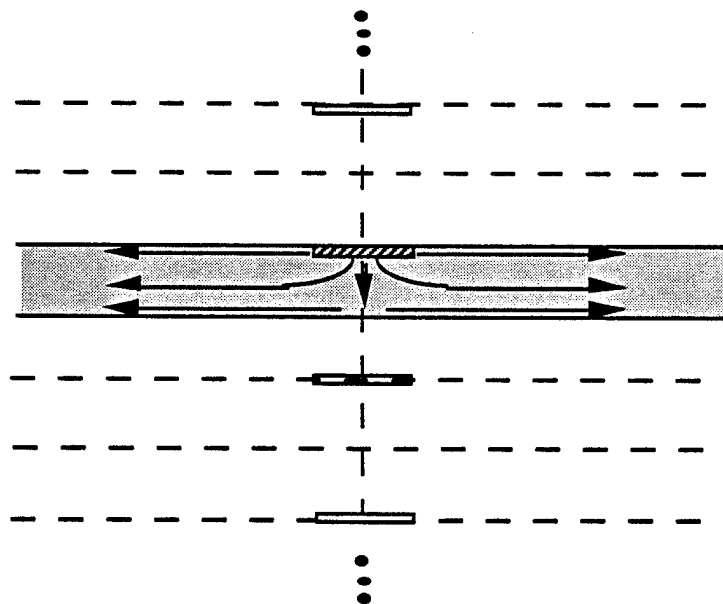


Figure 4.1.2. Model to calculate temperature distribution in anode/window.

To obtain accurate results, the required number of image sources depends on how large a radius is considered. For a 1-mm radius and 0.127-mm-thick anode, the sources are spaced apart by 0.254 mm, so that $1/0.254 = 4$ image sources are required both above and below the true source to give the required logarithmic behavior at the largest distance. Using a total of twelve sources, the calculation was performed with an Excel spreadsheet, and Figure 4.1.3 shows how the temperature varies, both as a function of radial distance and depth within the window. At large radial distances, the dependence coincides with the simpler model, as per Equation 4.1.4.

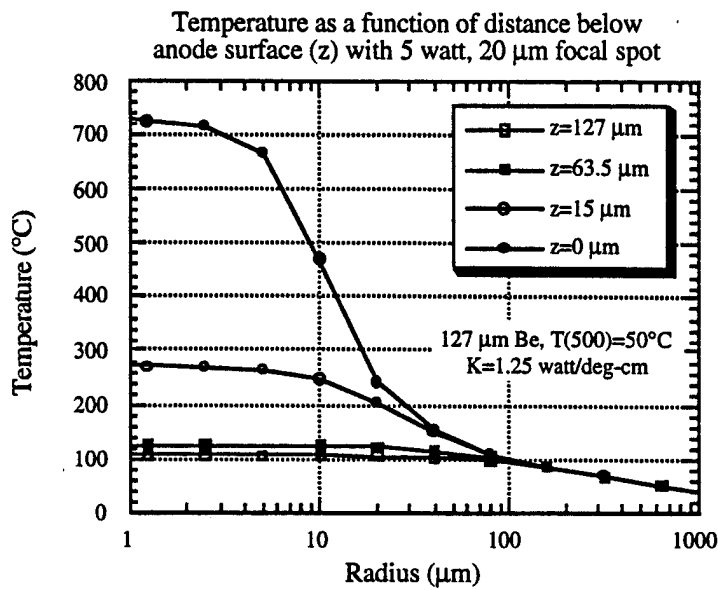


Figure 4.1.3. Temperature in anode as a function of radius and depth, z.

Note that the model predicts a steep temperature gradient across the anode thickness, since the spot size is small compared to the anode thickness.

We can calculate a maximum theoretical limit to anode temperature for our design by assuming that the x-ray tube lifetime is determined by the evaporation rate of the thin molybdenum (Mo) anode deposited on the beryllium window. Figure 4.1.4 shows data from several sources [Zemansky,

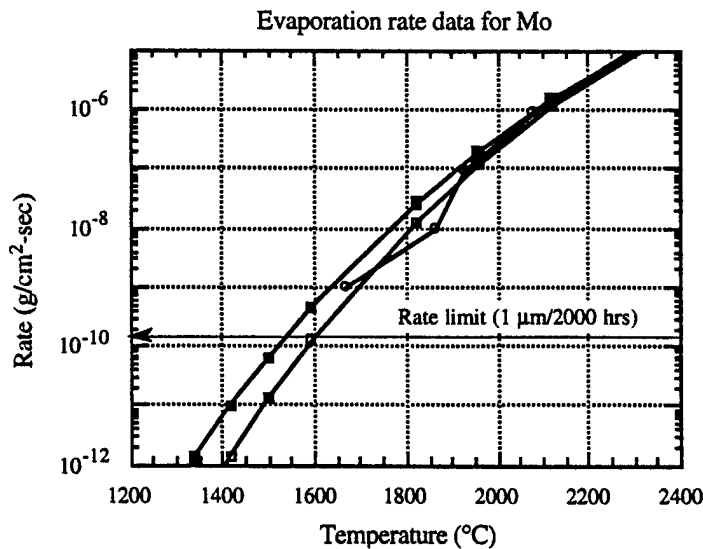


Figure 4.1.4. Evaporation rate of Mo as a function of temperature.

1972; Maissel and Glang, 1970] on the evaporation rate of Mo as a function of temperature. The desired thickness of Mo is determined by the competing requirements that it be thick enough to stop the highest energy incident electrons, yet thin enough to allow the greatest number of fluorescent x rays to emerge from the window, yielding an optimal thickness of 1.0 to 1.5 μm for the anticipated voltage range of 5-20 kV.

The upper temperature limit of about 1400°C is derived by assuming an evaporation rate of 1 $\mu\text{m}/2000$ hours for the tube lifetime requirement. A plot of peak temperature as a function of spot size and power loading is shown in Figure 4.1.5. Assuming a fixed heat-sink temperature of 50°C at a distance of 500 μm from the spot, the allowable power loading is proportional to focal spot size, at about 0.5 watt/ μm , which is half of the usual 1 watt/ μm rule-of-thumb for reflection-geometry solid x-ray tube anodes.

Substituting $P_0=10$ watts, $K=1.25$ watt/deg-cm for beryllium [Powell and Childs, 1972], $h=127 \mu\text{m}$, $r_0=63 \mu\text{m}$, and $r=2.25 \text{ mm}$ into Equations 4.1.3 and 4.1.4 yields a temperature drop of $\Delta T_{(\text{in spot})}=50^\circ\text{C}$ and $\Delta T_{(\text{out of spot})}=179^\circ\text{C}$ for a total drop of 229°C. The more accurate model which accounts for the temperature gradient across the anode thickness yields a maximum temperature drop of $\sim 320^\circ\text{C}$. This is quite low compared with the calculation for a 20- μm spot on a 1-mm diameter window, which gave a temperature drop of $\sim 1450^\circ\text{C}$. The larger spot size reduces the maximum temperature to well below the critical evaporation temperature of Mo ($\sim 1500^\circ\text{C}$).

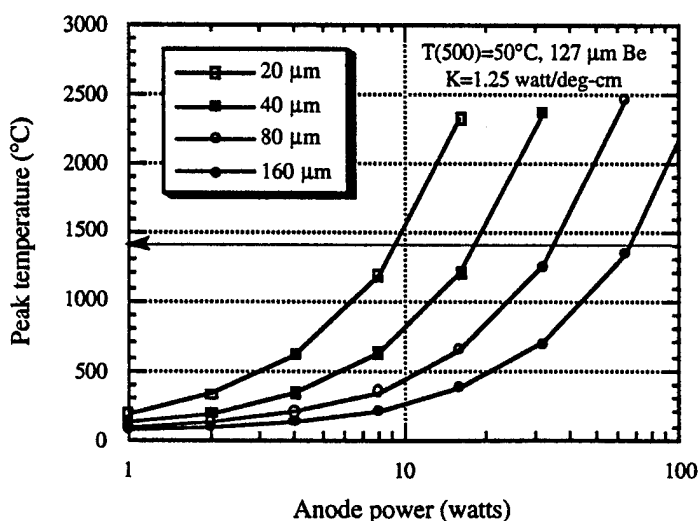


Figure 4.1.5. Peak temperature on anode as a function of power loading and spot diameter.

The primary conclusion from this modeling effort was that a power loading of 10 watts was below the theoretical limit for a desired focal spot diameter of 125 μm , given the practical constraints on

cooling and tube geometry. The modeling was also used to show that a 0.005-inch beryllium window would yield a greater flux of Mo-L radiation than a 0.010-inch-thick window, even when the power loading was decreased to give the same maximum focal spot temperature. The peak anode temperature scales with the inverse thickness (less sensitively for a small spot), so operating the tube at half the power still yields a net gain over the thicker anode, which reduces x-ray transmittance by a factor of three.

Another set of calculations was performed to estimate conduction of heat away from the tube, which would provide a realistic heat-sink temperature. Assuming that conduction alone carries heat to the x-ray tube mounting flange, the temperature drops along the conical nose-piece and straight sections were estimated to be 20°C and 1.5°C, respectively, using Fourier's Law and the appropriate conical or cylindrical geometry. The total drop from anode window to chamber would therefore be 21.5°C.

If the 10 watts are finally dissipated by convection from the top plate of the vacuum chamber, then the steady-state rate of heat transfer:

$$h = P_0 / (L^2 \Delta T_{air}) \quad (4.1.6)$$

can be set equal to estimates of the heat transfer coefficient for a plate in air, given by [Holman, 1976]:

$$h_{plate} = 1.32(\Delta T_{air}/L)^{0.25} \text{ watts/deg-m}^2 \text{ (laminar)} \quad (4.1.7)$$

$$= 1.43(\Delta T_{air})^{0.333} \text{ watts/deg-m}^2 \text{ (turbulent)} \quad (4.1.8)$$

where L is a characteristic length of the radiating surface (0.9 d, for a disk of diameter, d) and ΔT_{air} is the temperature difference between the chamber and air. A chamber diameter of $d \sim 0.34$ m and $P_0 = 10$ watt power loading would yield the curves shown in Figure 4.1.6 which intersect at a value of $\Delta T = 6^\circ\text{C}$.

For air at 21°C, the chamber top would be 27°C, and adding in the temperature drop from x-ray tube window to chamber top would bring the heat-sink temperature to approximately 48.5°C in the steady state. These results imply that water cooling of the tube or immediate surroundings would not be required, and that simple heat conduction and convective air cooling should be sufficient to maintain the tube temperature below 50°C.

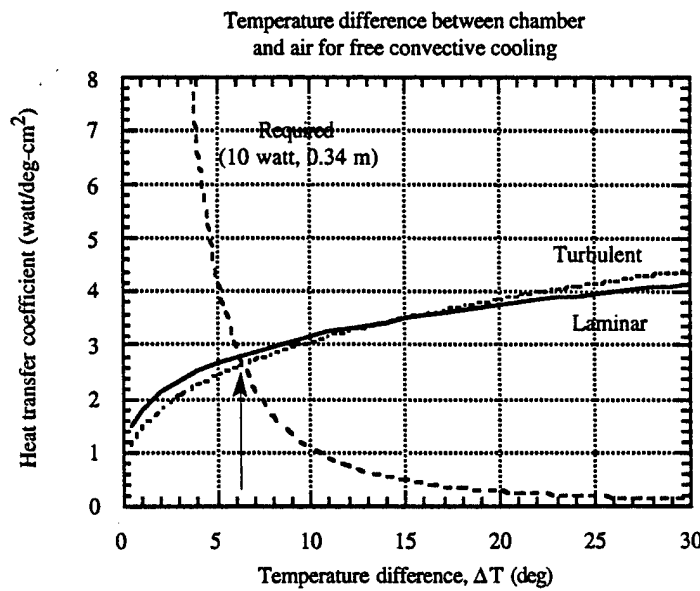


Figure 4.1.6. Heat transfer from chamber lid as a function of temperature difference.

4.1.2 Materials Issues

One of the original concepts for the x-ray tube, shown in Figure 4.1.7, was designed to achieve a small sample spot diameter while maintaining a large flux of x rays onto the sample spot.

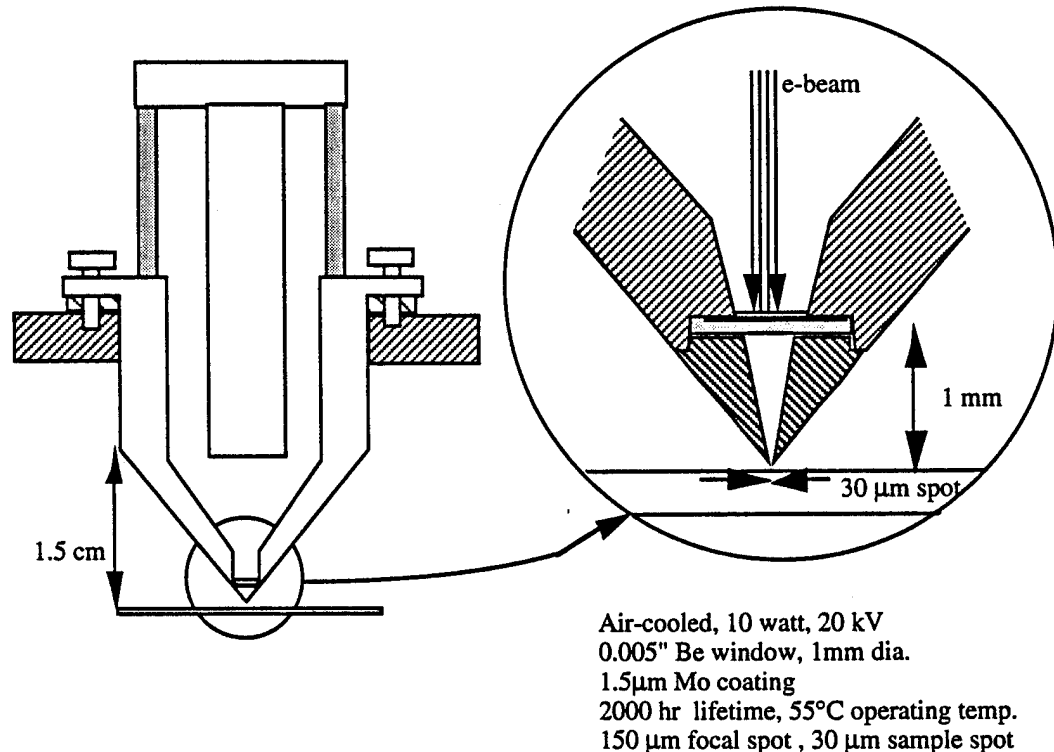


Figure 4.1.7. Concept for transmission target x-ray tube close coupled to sample.

The spot diameter, on the sample, can be calculated as a function of four parameters, which include the x-ray focal spot diameter, d_0 , the collimator diameter, d_1 , the focal spot-to-collimator distance, L_{01} , and the focal spot-to-sample distance, L_{0s} (see Figure 4.1.8). The spot diameter, d_s , can be expressed as the sum of two terms:

$$d_s = d_0 [L_{0s} - L_{01}] / L_{01} + d_1 L_{0s} / L_{01} \quad (4.1.9)$$

representing, respectively, the projection of the focal spot diameter onto the sample by a point collimator, and the projection of the collimator diameter onto the sample by a point focal spot.

The net flux onto the sample is a function of three parameters, including the focal spot-to-collimator distance, L_{01} , the collimator diameter, d_1 , and the power loading on the x-ray tube, P , assuming a fixed operating voltage. For a given spot size on the sample, we can define a figure of merit, F , proportional to the flux onto the sample:

$$F = P [d_1 / 4L_{01}]^2 \quad (4.1.10)$$

which is given by the product of the power loading and the fractional solid angle subtended by the collimator, assuming the collimator diameter is small compared to the source collimator distance. Eliminating the collimator diameter from Equation 4.1.10 with Equation 4.1.9 yields the result:

$$F = [P d_s^2 / 4L_{0s}^2] [1 - (d_0 / d_s) (L_{1s} / L_{01})]^2 \quad (4.1.11)$$

where the collimator to sample distance, L_{1s} , has been substituted for $L_{0s} - L_{01}$. This result shows that decreasing the source-sample distance, L_{0s} , to a minimum value provides potentially large gains in flux onto the sample for a given spot size, d_s . Furthermore, a flux gain can be achieved even with low-power x-ray tubes, since the dependence on power is only linear while the distance dependence follows an inverse square law.

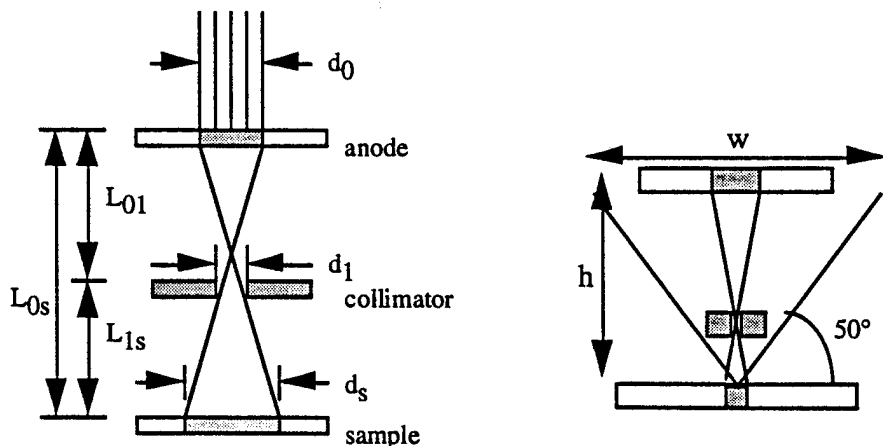


Figure 4.1.8. Geometry governing spot size and flux onto sample.

The design proposed by ARPES compromised some of the desired features of the initial concept, due to practical considerations of tube construction and available materials. The tube consisted of a glass envelope with attached electron gun assembly and electrical feedthroughs, sealed to a Kovar metal ring. A small beryllium window was brazed onto a shelf countersunk into the tip of the OFHC copper body, which serves as heat sink and mounting flange for the x-ray tube. After sputtering molybdenum onto the inner face of the beryllium window, the copper body was centered and welded to the electron gun assembly, and the tube was then evacuated, baked out, and sealed.

Based on data obtained from Dyson [1973], Figure 4.1.9 shows that at 20 kV, the electrons become fully diffused in the molybdenum anode by a depth of 0.3 μm , and that the integrated path length of 1.6 μm results in an effective range of only about 0.8 μm . Since this range scales with the square of electron energy, the expected range at 5 kV would be less than 0.1 μm . On the other hand, the attenuation length of Mo-L radiation in molybdenum is 1.5 μm , so that an anode thickness in the range of 1.0 to 1.5 μm would produce little self-absorption of x rays, while stopping the great majority of incident electrons. The targeted anode thickness was therefore 1.5 μm of molybdenum. Models comparing Mo, Al and other anode materials, indicated that Mo would be the overall best choice of material, for both general excitation of TiN and other thin films, and also from a materials aspect.

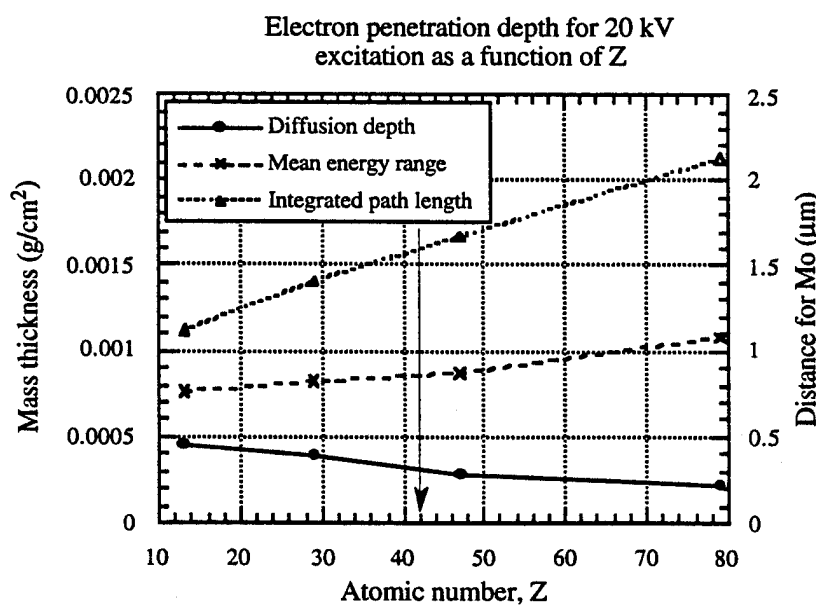


Figure 4.1.9. Penetration of electrons into an anode at 20 kV.

4.1.3 Specifications

The initial performance specifications of the x-ray tube and high-voltage power supply, developed with ARPES, are summarized in Table 4.1.2. The tube was designed with a grounded anode (target) for simplicity of design, and close coupling.

Table 4.1.2. Summary of tube and power supply specifications.

kV	Variable from -2 to -20
mA	Variable from 0.01 to 0.5 mA
Anode spot size (μm)	150 or less
Sample spot size (μm)	Adjustable from 1000 to 50
Power (W)	10 or more (constant W desired)
Length (inches)	3.5
Body diameter (inches)	1.0
Stability (4-hour period)	Spot movement $\leq 75 \mu\text{m}$
	Flux RSD $\leq 0.25\%$

4.2 WAVELENGTH-DISPERSIVE SPECTROMETER

4.2.1 Optic Design

A figured optic was designed to collect a significant fraction of the radiation emitted and transport it to the detector. Our approach was to approximate the point-to-point focusing conditions of an ellipse with a spherical optic. The radius of curvature, 23.5 cm, was selected to re-focus the radiation within the active volume of the detector. The width of the optic, 25 mm, was selected based on the width of the proportional counter window.

4.2.2 Multilayer Design

We considered several candidate multilayer designs for the wavelength region covering Ti-L and N-K x rays. The materials included Cr/Sc, Monel/Ti, Monel/Mg₂Si, W/Mg₂Si, W/Si and U/Sc. The Cr/Sc multilayer is commercially available (from Osmic) and, along with W/Si, is the standard multilayer used for the analysis of nitrogen. U/Sc is a new multilayer combination, provided to this project by MOXTEK, that has a theoretical increase in the nitrogen reflectivity over Cr/Sc. The principal drawback associated with scandium-containing multilayer coatings is their poor reflectivity for Ti L_α radiation due to the presence of the scandium L_{III} absorption edge at 402 eV. Of the remaining multilayer combinations, we found the Monel/Ti multilayer combination to be the most promising for N and Ti x-ray analysis.

Characterization methods

Candidate Monel/Ti multilayers were fabricated at ARACOR and then evaluated using our Siemens D5000 x-ray diffractometer, at the wavelength of copper $K\alpha$, to determine the multilayer structural parameters, and with N and Ti radiation, using our low-energy Henke tube, to determine the reflectivity.

The d-spacing, d , fractional thickness of the high atomic number (Z) layer, Γ , and interface roughness, σ , were determined for each multilayer with the x-ray diffractometer using the following methods.

The Bragg relationship,

$$m\lambda' = 2d \sin\theta'_m \quad (4.2.1)$$

which holds within the multilayer structure, relates the grazing angle of reflection, θ' , to the diffraction order, m , of a multilayer with d-spacing, d , at wavelength, λ' . The primed values are related to the externally measured, unprimed, values by Snell's Law,

$$\lambda/\lambda' = (1-\delta) = \cos\theta/\cos\theta' \quad (4.2.2)$$

where, $\delta = 1 - n$, is the index of refraction decrement, and n is the real part of the average index of refraction for the multilayer [Henke et al, 1990]. Combining these two relationships yields the dependence of diffraction angle on order number,

$$\sin\theta_m = \sqrt{(m\lambda/2d)^2 + (2\delta - \delta^2)}. \quad (4.2.3)$$

Since $\delta \ll 1$, this reduces to the following equation with little error.

$$\sin\theta_m = (m\lambda/2d) + \delta (2d/m\lambda) \quad (4.2.4)$$

For values of $(m\lambda/2d) \gg \sqrt{\delta}$, $\sin\theta_m$ increases linearly with m , while for smaller values there is an important refraction correction. Least squares estimates of d and δ are obtained by fitting Equation 4.2.4 to the measured values of θ_m for multiple diffraction orders. A value of Γ can then be estimated from,

$$\Gamma = (\delta - \delta_L)/(\delta_H - \delta_L) \quad (4.2.5)$$

where δ_L , δ_H are values for the pure low and high Z materials, respectively. These are derived from tabulated values of the optical constants for the 92 elements [Henke et al, 1993].

The integrated reflectivity for a kinematical model (with absorption) of a perfect multilayer film is given by [Henke et al, 1990],

$$R = r_0^2 \lambda^3 / [2\mu d^2] \{ (MF1)^2 + (MF2)^2 \} (1+\cos^2(2\theta))/2 \sin 2\theta \quad (4.2.6)$$

where r_0 is the classical electron radius, μ is the linear absorption coefficient of the multilayer at wavelength, λ , and the structure factor dependence, $MF = MF1 + i MF2$ is given by,

$$(MF1)^2 + (MF2)^2 = |A|^2 |B|^2 |C|^2 \quad (4.2.7)$$

where: $|A|^2 = (d/2\pi m)^2 [(n_x f_{1x} - n_y f_{1y})^2 + (n_x f_{2x} - n_y f_{2y})^2]$ (4.2.8)

$$|B|^2 = 2[1 - \cos(2\pi m(Y+T)/d)] \quad (4.2.9)$$

$$|C|^2 = 2(d/2\pi m T)^2 [1 - \cos(2\pi m T/d)]. \quad (4.2.10)$$

The $|A|^2$ term expresses the contribution to reflectivity from contrast between layers, with atomic densities of $n_x f_{1x}$, n_y and complex atomic scattering factors $f_{1x} - i f_{1y}$, $f_{2x} - i f_{2y}$. The $|B|^2$ term accounts for the ratio of high and low Z materials, where Y is the high Z thickness and T is the thickness of an assumed linear transition layer between high and low Z materials. Finally, the third term, $|C|^2$, introduces a reduction in intensity due to the thickness of the transition layer.

To simplify this result for the purpose of data fitting, the linear transition region is replaced by an interface with Gaussian roughness which produces a decrease in intensity given by the static Debye-Waller factor [Spiller and Rosenbluth, 1985],

$$|C|^2 = \exp\{-(2\pi m \sigma/d)^2\} \quad (4.2.11)$$

where σ is the rms roughness. Furthermore, without the transition layer, the $|B|^2$ term reduces to,

$$|B|^2 = 2[1 - \cos(2\pi m \Gamma)] \quad (4.2.12)$$

where Y/d is defined to be the fractional thickness of the high Z layer, Γ . If we neglect constant terms in order to find the dependence of reflectivity on order number, m , we obtain,

$$R_m = (1/m^2) [1 - \cos(2\pi m \Gamma)] \exp\{-(2\pi m \sigma/d)^2\} (1+\cos^2(2\theta))/2 \sin 2\theta \quad (4.2.13)$$

Using the Bragg relation, Equation 4.2.1, we can replace the θ dependent term with,

$$(1+\cos^2(2\theta))/2 \sin 2\theta = [1 - 2(m\lambda/2d)^2 (1 - (m\lambda/2d)^2)] / [(m\lambda/2d) \sqrt{1 - (m\lambda/2d)^2}] \quad (4.2.14)$$

resulting in an analytical expression for the relative integrated reflectivity as a function of order number, m , and the parameters d , Γ and σ .

Our Siemens D5000 x-ray diffractometer is used to obtain the integrated peak reflectivities of several orders, and, since these vary over many orders of magnitude, the least squares estimates of σ and Γ are obtained by fitting the values of $\ln(R_m)$ to the equation,

$$\begin{aligned}
 \ln[R_m] = & \ln[c] - 2\ln[m] + \ln[1-\cos(2\pi m\Gamma)] - (2\pi m\sigma/d)^2 \\
 & + \ln[1-2(m\lambda/2d)^2 (1-(m\lambda/2d)^2)] - \ln[(m\lambda/2d) - 1/2 \ln[1-(m\lambda/2d)^2]] \quad (4.2.15)
 \end{aligned}$$

where c is a constant which relates the relative reflectivities to the absolute reflectivities. For the least squares fit, the initial value chosen for Γ must be near the actual value, since the function defined by Equation 4.2.15 produces a least squares fit with many local minima. An initial estimate of Γ is provided by Equation 4.2.5 which is obtained from the d-spacing determination.

Monel/Ti

Figure 4.2.1 shows a reflectivity curve collected with the Siemens diffractometer using the Cu-K α energy (8041 eV).

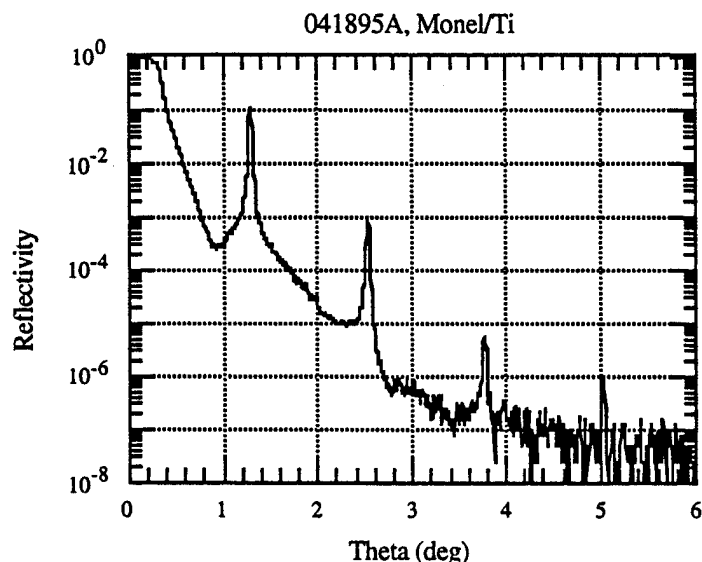


Figure 4.2.1. Reflectivity of Monel/Ti multilayer measured at Cu-K.

Using the methods described, the d , Γ and σ values were estimated from the fits shown in Figure 4.2.2 (a and b), yielding values of $d = 35.3$ Å, $\Gamma = 0.37$, and $\sigma = 4.0$ Å.

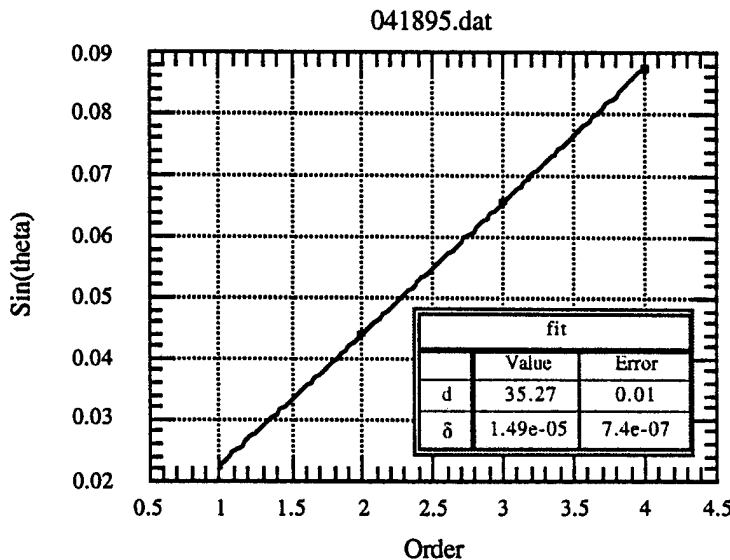


Figure 4.2.2 (a). Parameter fits (1) to four diffraction orders from Monel/Ti multilayer.

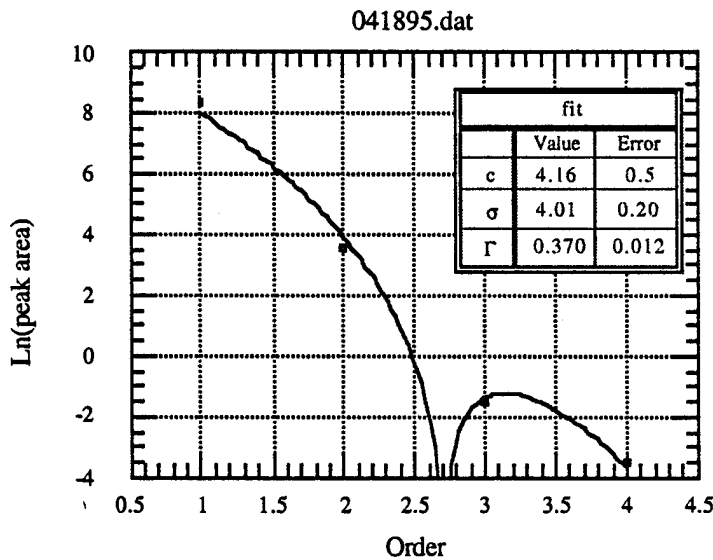


Figure 4.2.2 (b). Parameter fits (2) to four diffraction orders from Monel/Ti multilayer.

The roughness parameter, σ , was also estimated by trying to fit the measured Cu-K data with a program which simulates the multilayer reflectivity, as shown in Figure 4.2.3. The first order peak seems to be fit by a larger roughness parameter value of $\sim 10\text{\AA}$ (the lowest curve in Figure 4.2.3), but this value produces much lower intensities for the high order peaks than were actually observed. In order to see the fourth order peak, the estimated roughness should only be about 5\AA . A tentative conclusion is that the multilayer is rougher near the surface, so that the first order intensity, which depends predominantly on the top few layers, would be relatively weak.

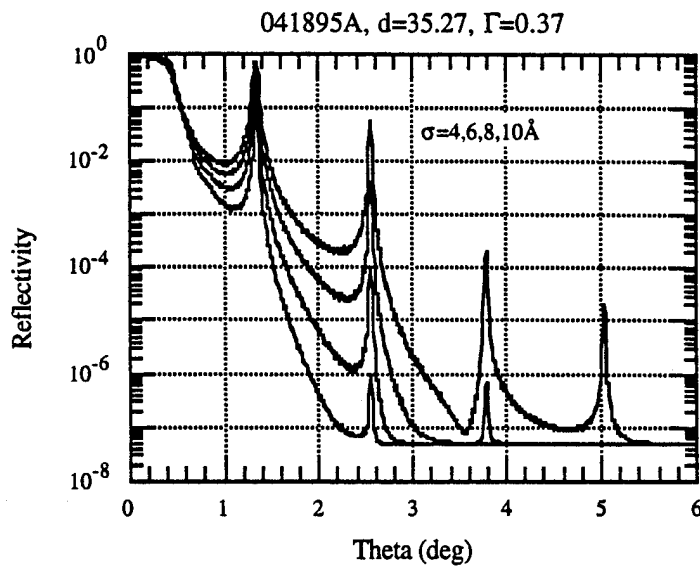


Figure 4.2.3. Simulated reflectivity for multilayer of Figure 4.2.1.

A third estimate of roughness was obtained by plotting the integrated counts under the first order peak for a number of different d-spacings, as shown in Figure 4.2.4. Fitting the d dependence with the previously developed formalism, Equation 4.2.13, yields an estimated roughness of 9.4 Å for the first order peak, which agrees with the conclusion of increased roughness near the surface of the multilayer.

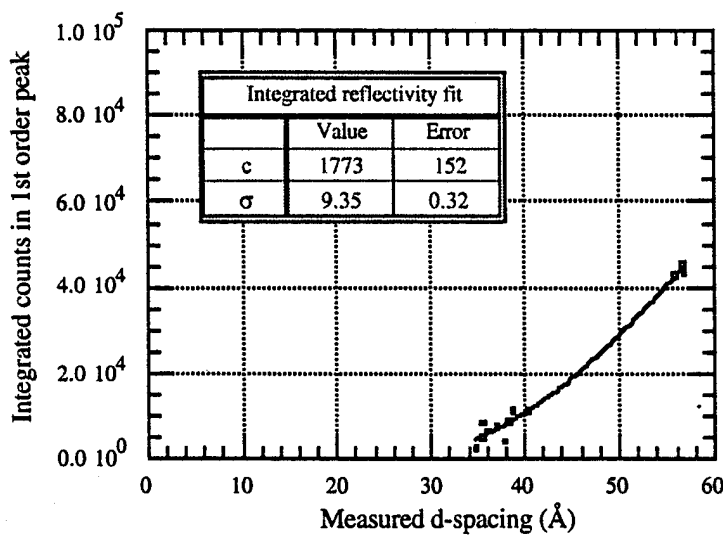


Figure 4.2.4. Measured 1st order integrated reflectivity as a function of d-spacing.

Analysis at N-K

The reflectivity was also measured at the wavelengths of interest for the WDS application by using the Henke x-ray tube source with a TiN anode. A Ti filter on the source was used to isolate the Ti and N characteristic lines, while a N₂ gas filter was used to provide variable attenuation of the Ti-L α,β characteristic lines. The resulting reflectivity plot, Figure 4.2.5, shows a relative enhancement of the N-K line and suppression of the Ti-L α line when the N₂ pressure is increased.

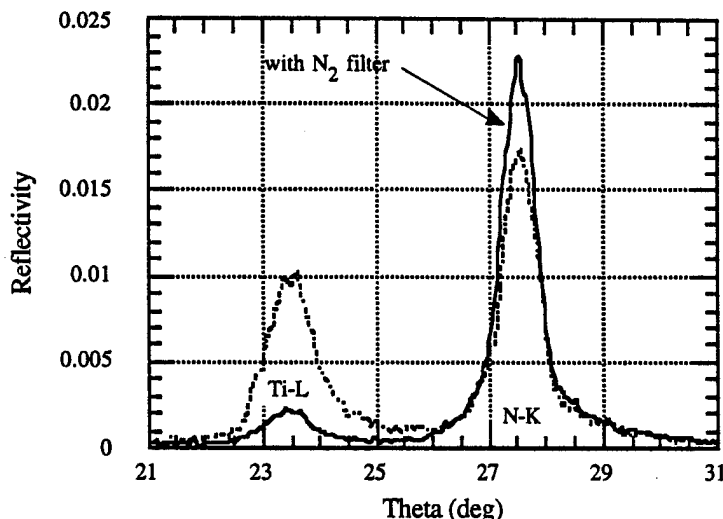


Figure 4.2.5. Reflectivity of Monel/Ti multilayer at N-K and Ti-L.

The peak and integrated intensities for pure N-K and Ti-L radiation were estimated by plotting the relative values of the N-K and Ti-L peaks and extrapolating to the y-intercept value to deduce the N-K reflectivity, as shown in Figure 4.2.6. The result is a predicted integrated reflectivity of 0.424 mrad for the 041895A multilayer at N-K, and a peak reflectivity of 2.3%. Multilayer 041595A showed an improved peak reflectivity of almost 4%.

The integrated reflectivities were modeled using the multilayer program for a range of roughness parameter values, yielding a curve which is well fit by a Debye-Waller type term, Figure 4.2.7. The measured reflectivity indicates a roughness of about 10Å for the first order peak at N-K, which is consistent with the roughness determined for the first order reflectivity at Cu-K.

Ux/Sc

Another multilayer combination consisting of uranium and scandium was provided by MOXTEK for evaluation. The samples had a fixed d-spacing of ~34Å with a variable number of layer pairs. Figure 4.2.8 illustrates the reflectivity measured at Cu-K for one of these samples.

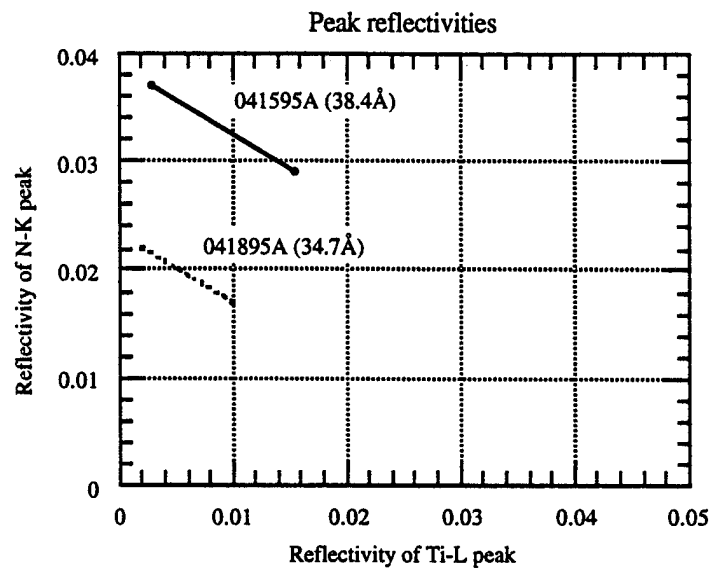


Figure 4.2.6. Plot used to infer reflectivity for a single wavelength of x rays.

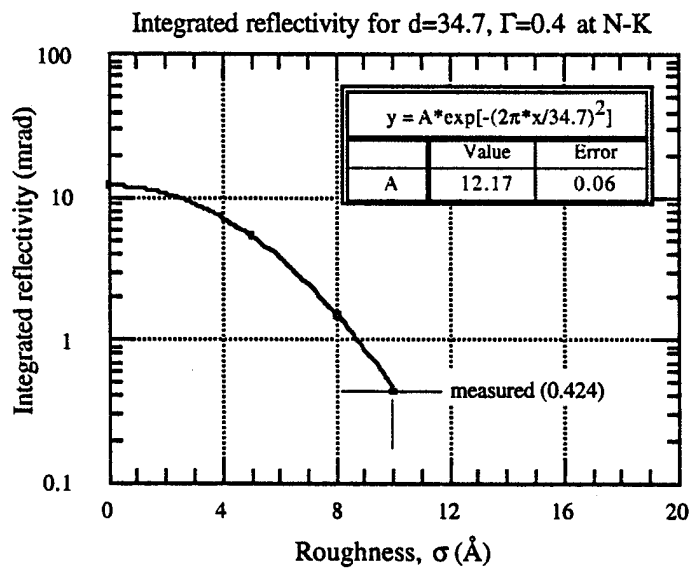


Figure 4.2.7. Roughness of multilayer deduced from reflectivity at N-K.

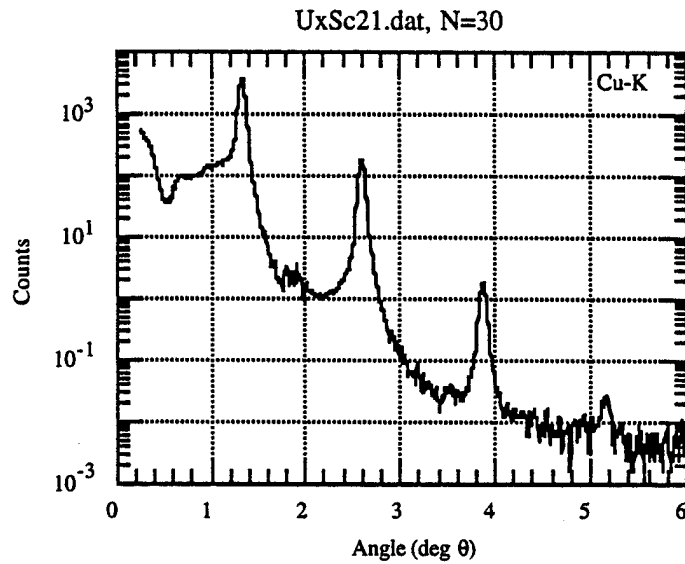


Figure 4.2.8. Reflectivity of Ux/Sc multilayer measured at Cu-K.

The Cu-K data showed a consistent d-spacing, gamma, and roughness between samples, as shown in Table 4.2.1.

Table 4.2.1. Cu-K diffractometer data for Ux/Sc multilayers.

Sample	N	D-spacing	δ	σ (Å)	Γ
UxSc21	30	34.33(.03)	1.72e-5(.12)	3.50(.10)	0.282(.003)
UxSc22	50	34.07(.03)	1.99e-5(.17)	3.00(.13)	0.295(.005)
UxSc23	70	34.15(.02)	2.00e-5(.19)	3.00(.13)	0.295(.005)
UxSc24	85	34.56(.05)	1.99e-5(.40)	2.96(.10)	0.319(.003)
UxSc25	100	34.15(.02)	2.00e-5(.21)	2.92(.09)	0.291(.006)

Only one of the multilayers (UxSc24) showed a distinct suppression of one of the diffraction orders (3rd), which is consistent with a gamma value which is closer to 0.33 than for the other multilayers.

Using tabulated [Henke et al., 1993] delta values (U:4.48e-5/Sc:9.10e-6) and densities (U:19.10/Sc:2.99), the average δ value of 1.94e-5, derived from the measured refraction correction, implies a value of $\Gamma = 0.289$ from Equation 4.2.5, which is in good agreement with the average gamma of 0.296 derived from fitting the relative areas of the Cu-K diffraction peaks. Since the model used to deduce roughness, σ , from does not take into account the finite number of layer pairs, the observed decrease in roughness may be due to the improving reflectivity with

increasing number of layer pairs. The multilayer appeared to be smoother than the Monel/Ti multilayer, judging from the tabulated values and good fit to the simulated reflectivity of the first order peak, as shown in Figure 4.2.9.

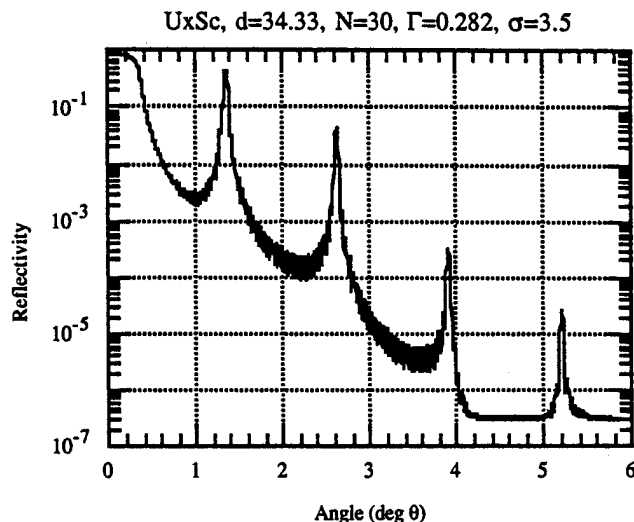


Figure 4.2.9. Simulated reflectivity for multilayer of Figure 4.2.8.

N-K analysis

Four of the five multilayers were examined at the energy of N-K, using a TiN anode on the Henke tube. Table 4.2.2 summarizes the results of the reflectivity scans. Figure 4.2.10 illustrates a sample reflectivity curve for UxSc25.

Table 4.2.2. Reflectivity data for Ux/Sc multilayers using N-K radiation.

Sample No.	No. Layers	Bragg Angle	Peak ($\pm 20\%$)	Peak Width	Refl. ($\pm 20\%$) (mrad)	Theory (mrad)
UxSc21	30	27.25°	0.038	1.11°	0.95 mrad	2.59 mrad
UxSc23	70	27.60°	0.046	0.79°	0.97	3.32
UxSc24	85	27.25°	0.059	0.77°	1.07	3.35
UxSc25	100	27.40°	0.043	0.73°	0.69	3.36

Integrated reflectivities are roughly 30% of the predicted values, using the multilayer parameters deduced from the Cu-K data. Since the model used to deduce the roughness parameter is rather crude, a different (larger) apparent roughness may hold at the N-K energy. Calculations indicated that an apparent roughness of 6.5 Å at each interface in the multilayer would explain the decreased reflectivity at N-K.

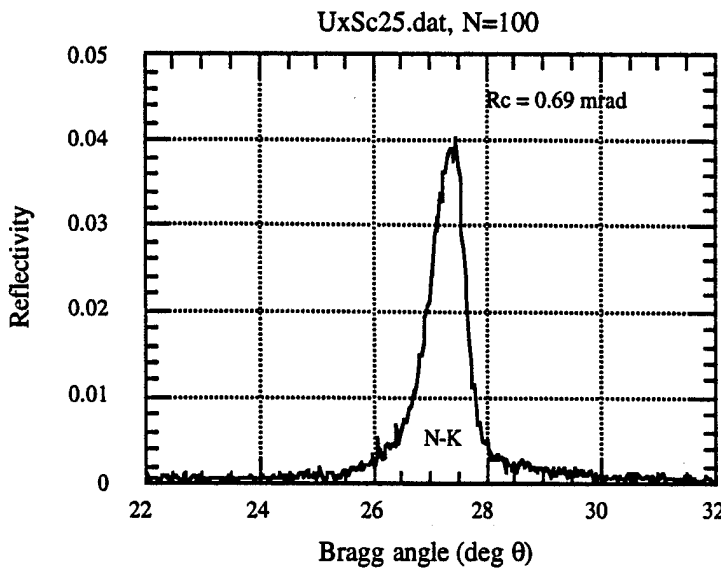


Figure 4.2.10. Reflectivity of Ux/Sc multilayer at N-K and Ti-L.

The measured line widths were well fit by theoretical values added in quadrature to a constant value of 0.60° . This width corresponds to an energy range of 7.7 eV which is not associated with the multilayer that probably arises from inherent band widths of ~ 3 eV for the individual N-K and Ti-L_{α,β} characteristic lines [Holliday, 1968], as well as the 8.5 eV energy spread between the N and Ti lines, which have different relative intensities. The net effect of the additional energy width is to reduce the peak intensity to 60% of its unbroadened value.

In comparison with the Monel/Ti multilayer with an equivalent d-spacing, the Ux/Sc combination had a reflectivity which was roughly 2.5 times greater, but it displayed very little reflectivity for Ti-L_{α,β} lines. This made it unsuitable for a scanning WDS system where it is desirable to evaluate both the N-K and Ti-L contributions from the TiN samples.

4.2.3 Detector Design

The detector for the WDS spectrometer consisted of a dual-anode Siemens gas-flow proportional counter, shown in Figure 4.2.11. The counter was backfilled with propane gas to a pressure of 96 Torr, which is sufficient to absorb all of the incident N-K and Ti-L x rays over the absorption path of 25 mm. The counter was run at a bias of 1270 Volts, which resulted in pulse heights of about 1 volt for N-K x rays.

Most counter windows for soft x-ray detection employ carbon-based polymer films, such as Formvar, polypropylene, or VYNS. However, these materials are not suitable for N-K detection

because the x-ray energy of 392.4 eV is just above the absorption edge for carbon, at 284 eV, which results in very low transmittance.

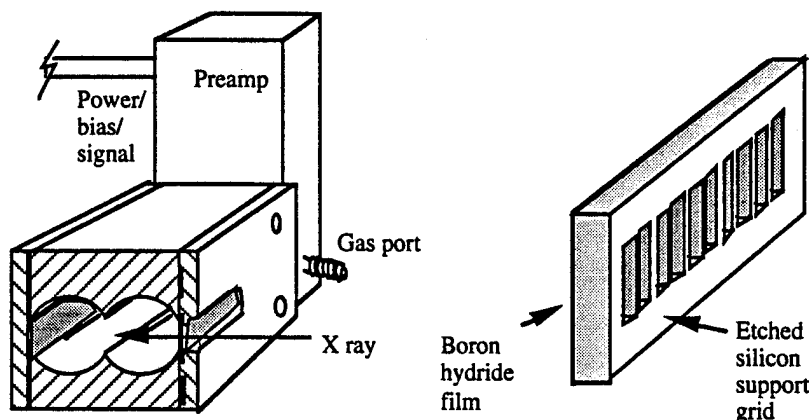


Figure 4.2.11. Detector and window used for detection of N-K, Ti-L.

For this reason, a recently developed boron-hydride window from MOXTEK was employed, consisting of a thin film of boron hydride, coated with 200 \AA of aluminum and supported on an etched silicon support grid, Figure 4.2.11. ARACOR designed a brass plate for mounting the window onto the proportional counter, and MOXTEK epoxied the window into the plate and used silver paint to provide electrical continuity between window and plate.

The exact composition of the window was not disclosed by MOXTEK, but a plot of melting point vs. B atom fraction for known hydrides from the CRC Handbook of Chemistry and Physics (reproduced in Figure 4.2.12) shows that, for a window which can be safely baked at 200°, the

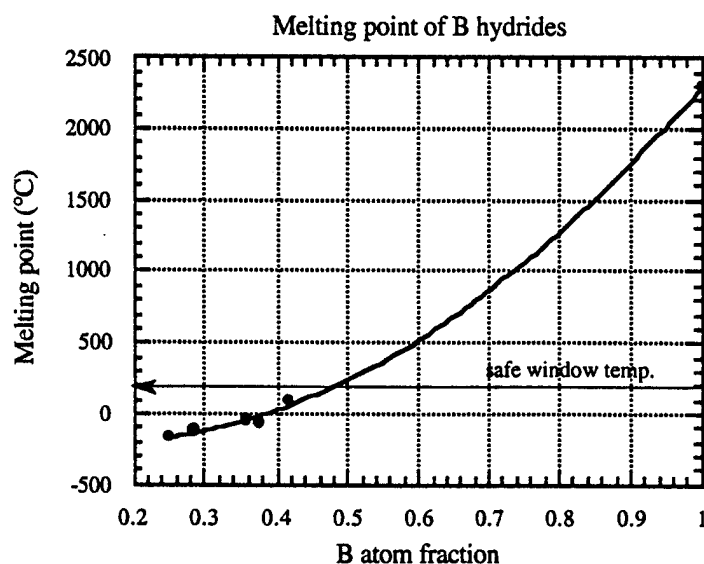


Figure 4.2.12. Melting point of boron hydrides as a function of boron content.

boron atomic fraction is probably at least 0.66. A plot of density vs. B atom fraction, Figure 4.2.13, yields an estimated density of 1.5 to 2 g/cm³, so the expected transmittance for a number of film thicknesses can be calculated, Figure 4.2.14. MOXTEK quoted a transmittance at N-K of ~50% without the aluminum coating, which would be consistent with a thickness near 0.27μm. Including the aluminum, the estimated transmittance is 46%.

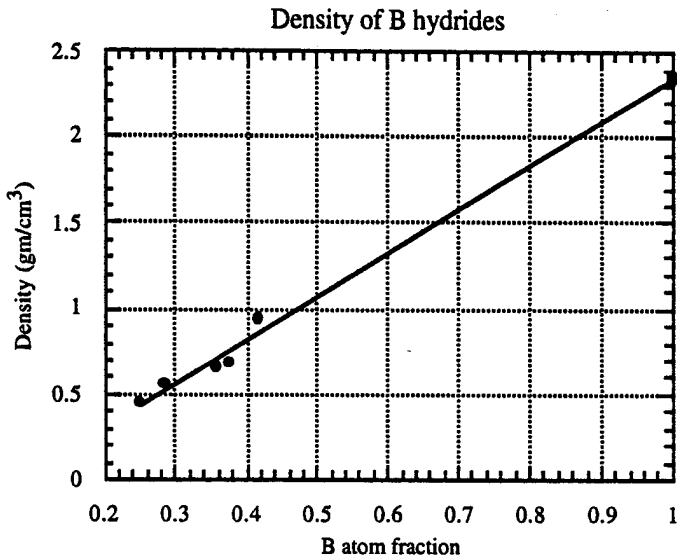


Figure 4.2.13. Density of boron hydrides as a function of boron content.

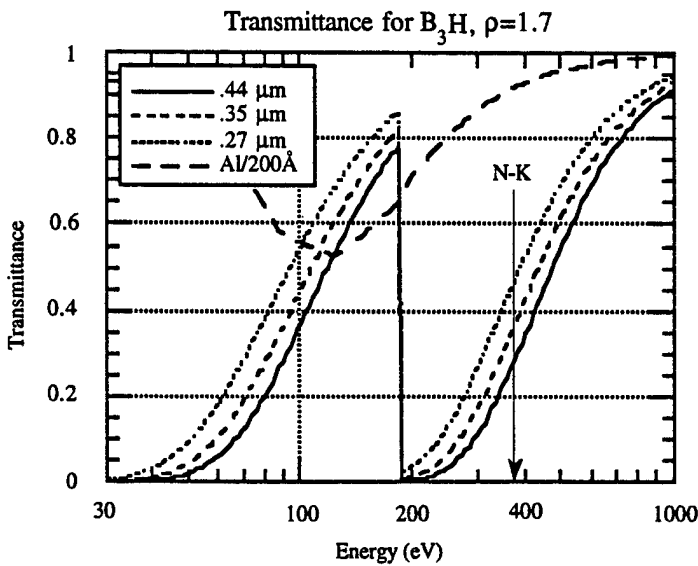


Figure 4.2.14. Predicted thickness dependence of boron hydride transmittance.

The window support grid consists of thin silicon plates etched from a solid wafer with an aspect ratio of about 3:1, where each rib is 50-μm wide, with a 250-μm gap. This restricted the radiation

coming out of the plane of dispersion to 15 degrees. It was necessary to determine the effect on transmittance for rays which are not incident perpendicular to the window. Figure 4.2.15 shows the overall geometry as well as the grid dimensions.

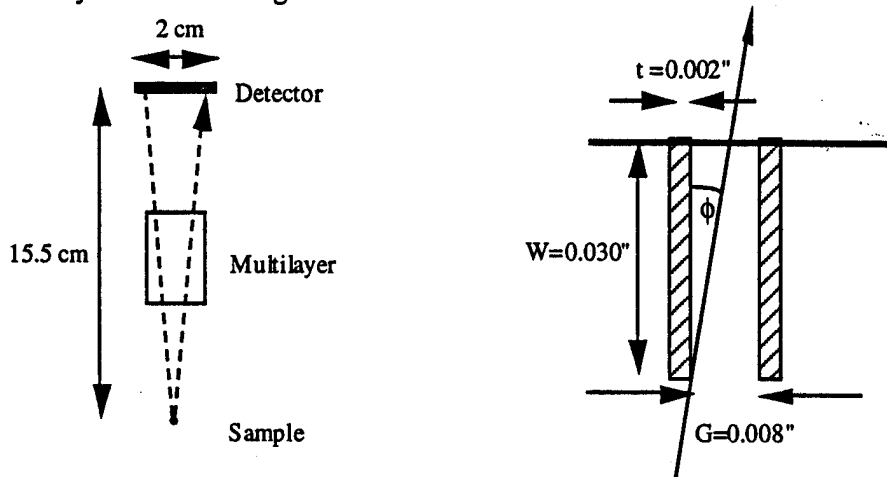


Figure 4.2.15. Geometry describing transmittance of window support grid.

For an angle of incidence, ϕ , the transmission by the grid is given by:

$$T(\phi) = [G - W \tan\phi] / [G + t] \quad (4.2.16)$$

The average transmission over the total range of angles is then given by:

$$\begin{aligned} \langle T \rangle &= \int_{(0,\Phi)} T(\phi) / \Phi \, d\phi \\ &= G/(G+t) \{ 1 - W/(2G\Phi) \log[1 + \tan^2\Phi] \} \end{aligned} \quad (4.2.17)$$

where Φ is the maximum angle at which x rays enter the detector. For small angles, Φ , the result simplifies to:

$$\langle T \rangle = G/(G+t) [1 - W\Phi/2G] \quad (4.2.18)$$

Based on the dimensions shown in Figure 4.2.15, the maximum angle of incidence is $\Phi = 3.7^\circ$. Substituting into Equation 4.2.18, the grid structure passes 76% of the incident radiation. Since 46% of this is transmitted through the boron-hydride film, the net transmittance for grid structure and window is ~35%.

4.2.4 Motion Control and Design Layout

Two WDS geometries were originally considered for incorporation into the chamber. The first consisted of several flat multilayers tilted at slightly different angles of incidence to direct radiation into a large area proportional counter located inside the vacuum chamber. This option was not pursued because of the difficulty in obtaining large-area windows transmissive to N-K (392 eV)

radiation. The second design consisted of a curved optic which could focus and redirect the sample fluorescence towards the top of the chamber where a small area detector could be mounted. This design, illustrated in Figure 4.2.16, uses an externally mounted linear motion to translate the

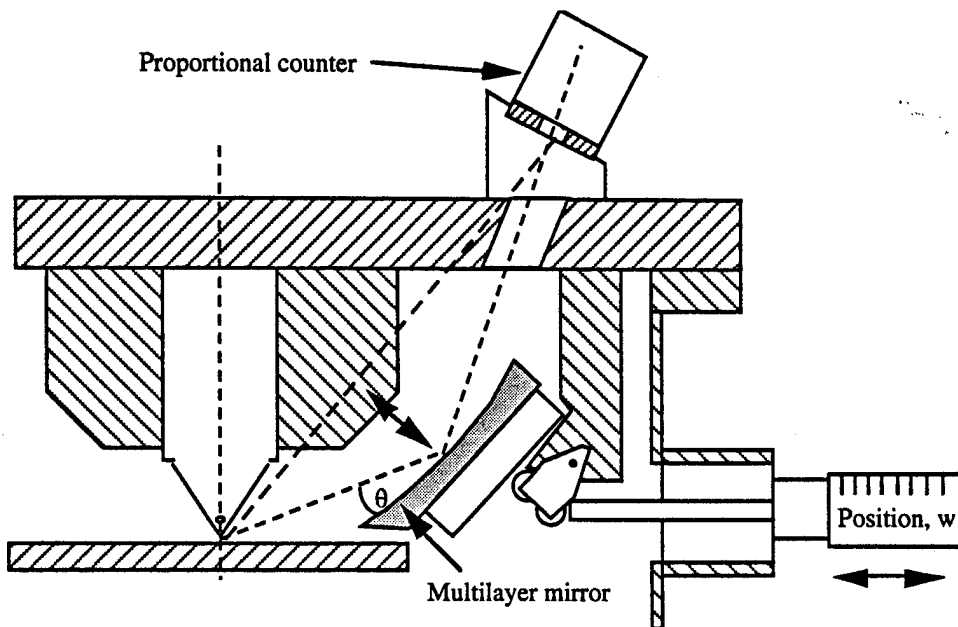


Figure 4.2.16. Layout for wavelength dispersive spectrometer.

multilayer in a direction which tunes the angle of incidence, θ , hence, the x-ray energy reflected from the mirror. A disadvantage of this geometry was the large distance between sample and detector. The mirror focused the radiation from a point source to a line focus at the detector, where a window length of 2 cm limited the amount of radiation that could be collected. The proportional-counter detector, as described in Section 4.2.3, was located on the chamber lid and tilted to increase its acceptance angle.

The final design drawing of the wavelength dispersive spectrometer is shown in Figure 4.2.17. This was developed in conjunction with the subcontractor, McKinney Engineering.

The angles of incidence of the radiation onto the optic were adjusted by the translation of the optic along a 45 degree line. This motion was introduced to the optic by a linear motion feedthrough (Model BLM-275-1-03 from MDC Vacuum Products Corporation of Hayward, CA) that pushes on the rollers. This motion could be controlled both by an end-mounted Superior Electric Slo-Syn stepper motor, or by hand with a vernier-scale adjustment. A cable was built to interface the stepper motor to an in-house Velmex Model 86MM-2 motor controller and driver. The motion could be programmed from the front panel of the controller, or remotely controlled by an external computer, using an RS-232 serial interface. The operation is discussed further in Section 5.2.4.

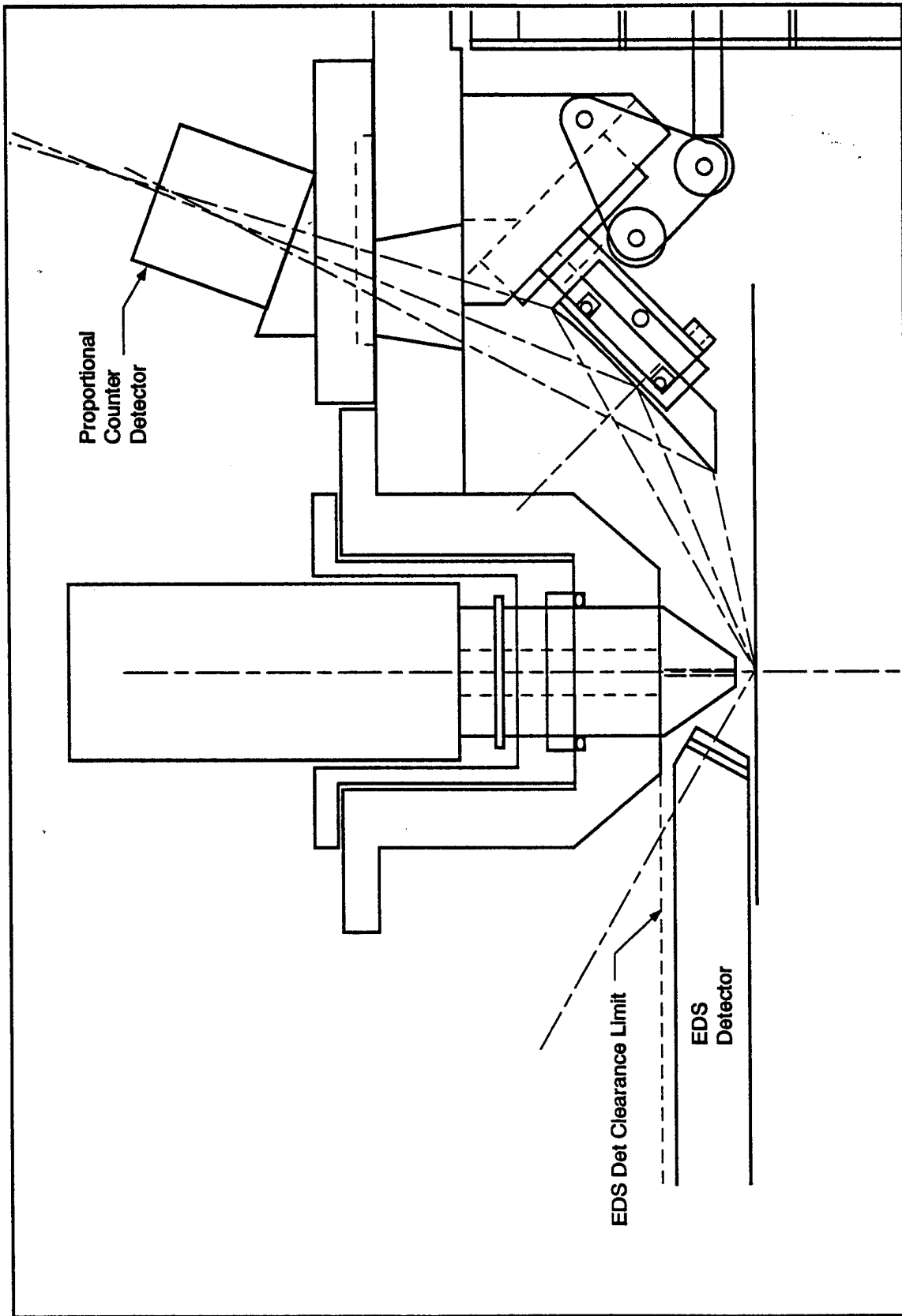


Figure 4.2.17 Design layout drawing for wavelength-dispersive spectrometer.

4.2.5 Specifications

The initial specifications developed for the wavelength-dispersive spectrometer are summarized in Table 4.2.3.

Table 4.2.3. Specifications of the wavelength-dispersive spectrometer.

Parameter	Value
Wavelength range	26.9 to 33.6 Å
Solid angle	0.01 steradians
Detector efficiency	34%

4.3 ENERGY-DISPERSIVE SPECTROMETER

4.3.1 Detector Design and Fabrication

The requirements for the LN-cooled Si(Li) detector were as follows: (1) analysis of elements down to at least carbon; (2) resolution at about 150 eV FWHM (Full Width at Half Maximum), or better, at 5.9 keV; (3) as large a solid angle as possible, given a maximum angle of 50° from the horizontal (sample) surface within which to place the detector; (4) manual slide to be able to adjust the position of the detector in the horizontal axis.

For the optimum crystal size, 30 mm² was suggested as the balance between good resolution and solid angle. This value was used in the design. Our initial drawing of the requirements for the detector are shown in Figure 4.3.1, and the final drawing by the vendor (GDE), of the end-cap section, is shown in Figure 4.3.2.

The "chisel-nose" end-cap and collimator design maximizes the take-off and total solid angles. The detector tube was fabricated from stainless steel which provides an effective shield up to at least 30 keV. The collimator was fabricated from aluminum, coated in a carbon "dag" to further reduce the fluorescence yield and thereby reduce spectral contamination.

The detector window was a MOXTEK AP1.3 grade polymer window, with a 75-80% open area, with the remainder consisting of parallel silicon grids which were 360 micron thick, 20 microns wide, and spaced 80 microns apart (100-micron pitch). The grids are arranged to be in a vertical plane when the window is mounted, to minimize the absorption path for x rays from the sample. The window was 300 nm thick, and coated with 40 nm of aluminum to reduce the light transmission (which would render the detector unusable) and help seal the window. With this thickness of aluminum, it is still necessary to keep the detector assembly in a light-tight chamber, as some visible light can still penetrate the window.

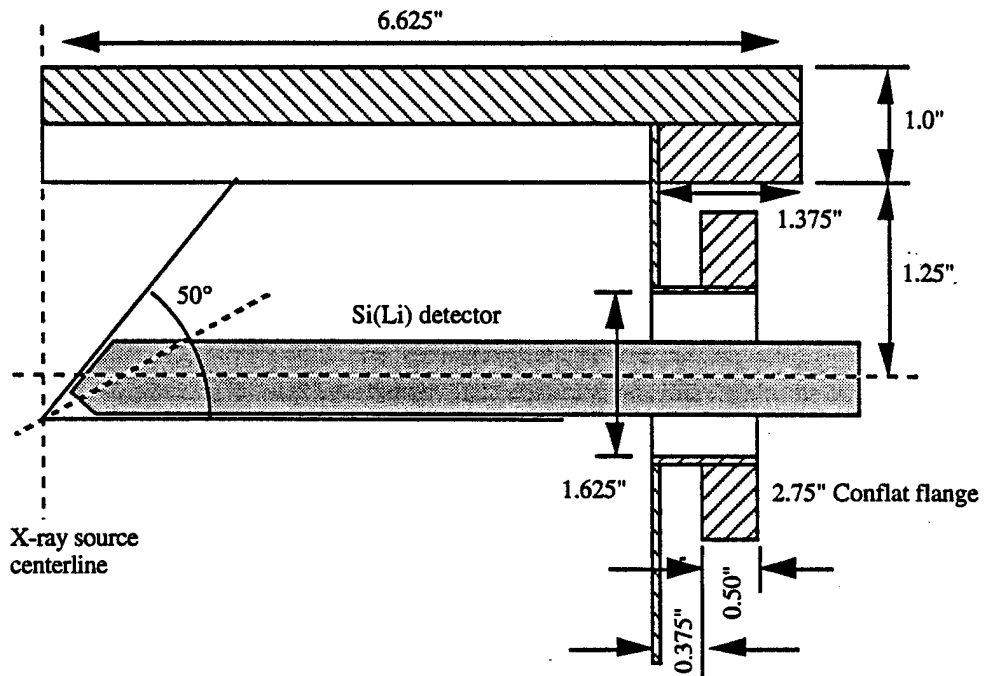


Figure 4.3.1. Required Si(Li) detector geometry.

Originally the detector was to be built from refurbished parts to save money, but because of delays in shipping and the availability of parts, the vendor agreed to supply new parts, including a "mini-Dewar" cryostat which was half the usual volume, but with the same 4-day holding time for liquid nitrogen.

We also had the opportunity to evaluate one of the new Amptek XR-100T silicon pin-diode detectors, and compare its performance with the more conventional Si(Li) detector. This was one of the early models and had a beryllium window which was 3 mils (75 micron) thick. More recent models have windows with a thickness down to 0.5 mils, which would be more suitable for low-energy XRF.

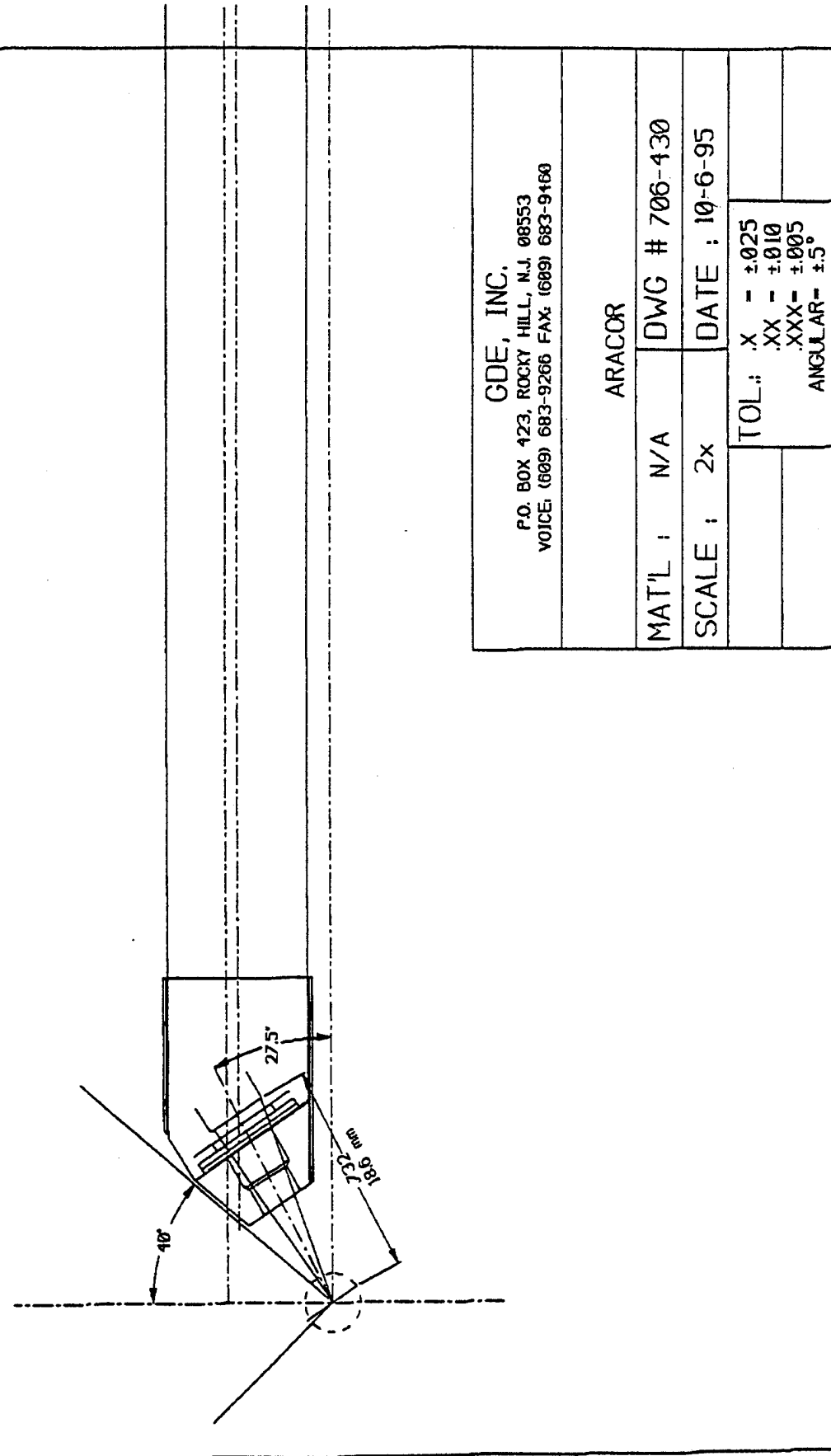


Figure 4.3.2. Actual geometry of Si(Li) detector.

4.3.2 Specifications

The initial specifications for the Si(Li) detector are summarized in Table 4.3.1.

Table 4.3.1. Specifications of Si(Li) detector.

PARAMETER	VALUE
Lowest element detected	Carbon
FWHM Resolution @ Mn K α (5.9 keV)	150 eV at 30 microsecond shaping time
Active area	30 mm ²
Ultra Thin Window (MOXTEK AP1.3)	300 nm Polymer + 40 nm Al coating
Silicon crystal thickness	3 mm
Dead layer thickness	200 nm
Gold contact layer	20 nm
Retractable Slide	At least 70 mm
Solid Angle	0.10 steradians

Because of difficulties in achieving the geometry of the end cap and collimator, the final solid angle was less than that specified. We also had concerns about the availability of the 50° angle, and so we took a more conservative approach and designed to an angle of 47° which noticeably reduces the solid angle. It was also reduced by 25% because the effect of the grids in the MOXTEK window had been neglected, so the total available solid angle in the final configuration was reduced by 50% to 0.05 steradians.

A calculated transmission curve showing the efficiency of x-ray detection over the range 0.1 through 20 keV, including the effects of the window, grid, silicon dead layer, gold contact layer and silicon crystal thickness, is shown in Figure 4.3.3. Note that the maximum efficiency never exceeds 0.75, because the MOXTEK AP1.3 grids are infinitely thick for all x rays up to 20 keV, and they occupy 25% of the total area of the detector. The efficiency starts to fall off above 15 keV, because the detector crystal is no longer infinitely thick to x rays.

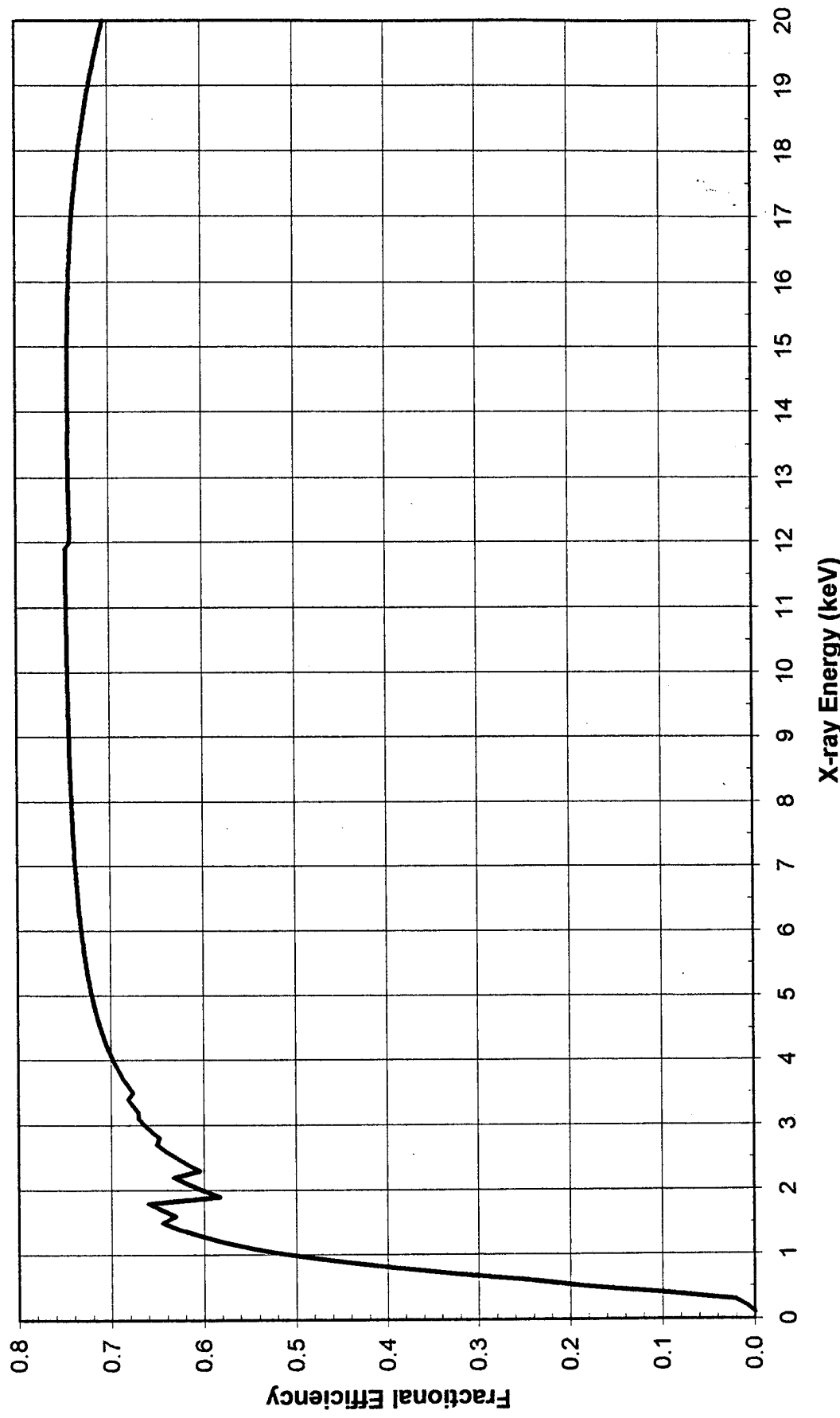
Efficiency of Si(Li) Detector with Moxtek AP1.3 Window

Figure 4.3.3. Detection efficiency of Si(Li) detector for low-energy x rays.

4.4 INTEGRATION ISSUES

4.4.1 Source-Sample-Spectrometer Geometries

The x-ray tube, sample stage, and detectors were designed to fit within a modified cylindrical vacuum chamber, which was available at ARACOR from a previous project. The chamber had a horizontal stage designed to support a 15 cm wafer which could be loaded through an o-ring sealed side door on the chamber. The stage position was manually adjustable from outside the chamber using a sliding rod with bellows feedthrough located 180° from the loading door. The stage position could be manually adjusted with an accuracy of about 1 mm, although there was no attached scale to measure position. Five additional ports were also available around the circumference of the chamber, with one port on the chamber bottom. Given the basic chamber geometry, functions for the available ports were assigned as shown in Figure 4.4.1.

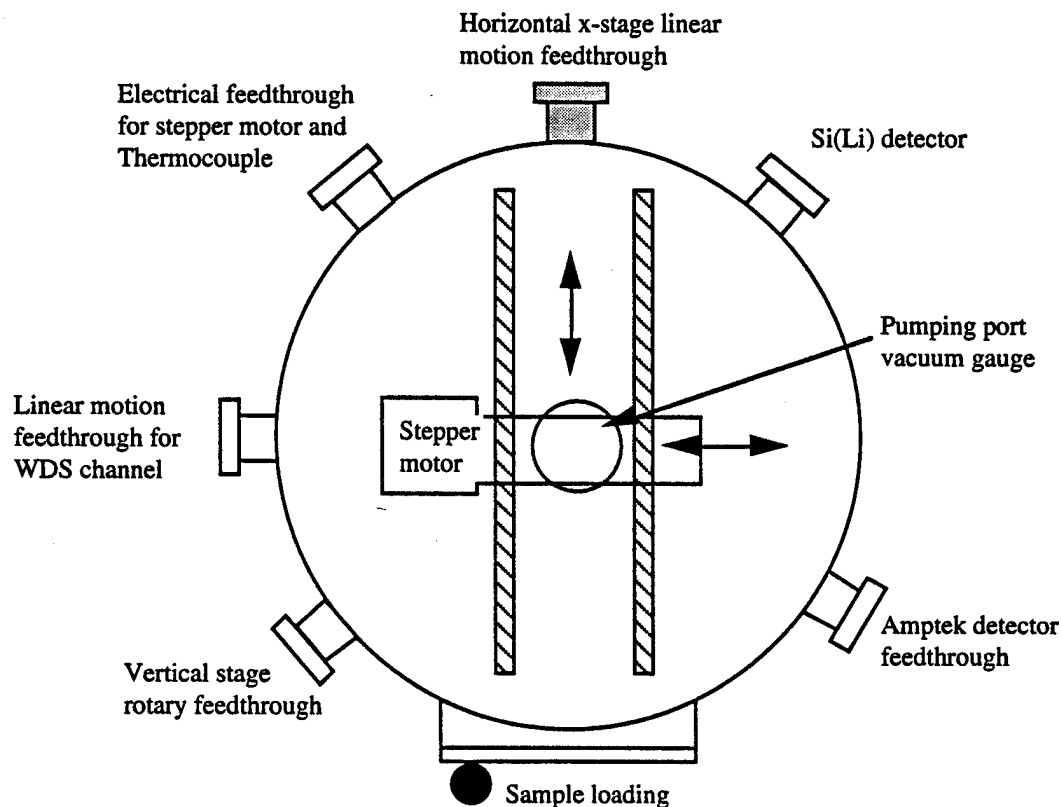


Figure 4.4.1. Top down view of available ports on vacuum chamber.

Two additional motions were added to the sample stage, permitting horizontal scanning of the stage by means of a stepper motor located in the vacuum chamber, and a miniature vertical stage which allowed the sample to be brought into close proximity with the end of the x-ray tube which was mounted vertically in the chamber lid.

One port was reserved for the Si(Li) detector, which was mounted on a linear feedthrough to allow positioning along a radius of the chamber, and a second port was dedicated to an electrical feedthrough for controlling the stepper motor and introducing thermocouple wires to monitor x-ray tube temperature. Adjustment of the WDS channel to allow scanning of energies was assigned to a third port. Although an observation port with microscope would have been useful for sample alignment under the source, the last available port was used instead to accommodate an Amptek PIN diode detector, which provided initial characterization of the x-ray tube prior to delivery of the Si(Li) detector.

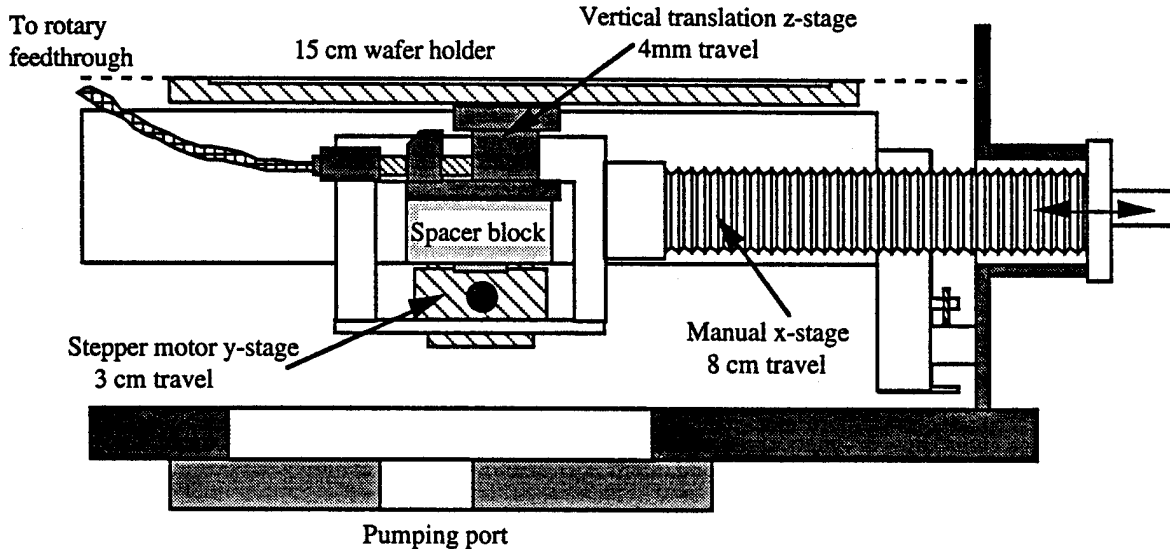


Figure 4.4.2. Detail of sample stage translation.

Figure 4.4.2 illustrates the method used to add the two additional degrees of sample motion. The wafer holder was originally mounted on a cradle supported by roller bearings which was connected directly to the manually driven linear feedthrough. The arrangement was redesigned so that the cradle now supported a stepper motor and stage which provided 3 cm of travel perpendicular (in and out of the page) to the manual motion (left and right). The Vexta stepper motor was driven by the in-house Velmex Model 86MM-2 controller, which provided a minimum scanning speed of $50\mu\text{m/s}$ with the translation stage being used. A spacer block on top of the stepper motor stage was designed to hold a small vertical stage which in turn carried the wafer holder. The vertical motion range of 4 mm was controlled by a flexible cable running to a rotary feedthrough.

The relative alignments of the sample stage, x-ray source, and Si(Li) detector were determined as follows. The Si(Li) detector was mounted on one of the chamber ports using a conflat flange, as shown previously in Figure 4.3.1. Given a 0.5-inch diameter for the end of the detector snout, which was assumed to be concentric with the chamber port, the height of the sample could be designed to be adjustable to within ~ 1 mm below the detector. The x-ray tube and mounting

hardware, which were attached to the chamber lid, could also be adjusted to place the end of the x-ray tube collimator at the maximum sample height position.

The known distance from chamber floor to conflat flange could be used to design the sample stage spacer block, Figure 4.4.2, to set the range of motion for the sample height position. A (nominal—see Section 4.3.2) 50° angle measured from the intersection of the centerline and maximum sample stage height was used to design the Si(Li) detector end piece and x-ray tube to achieve the closest possible coupling between x-ray tube anode, sample, and detector. The anticipated solid angle of radiation captured by the detector was ~0.1 sr (as noted in Section 4.3.2), based on a detector area of 30 mm² and a sample to detector distance of 19.2 mm, with the detector center at an elevation of 30°. The x-ray tube and collimator were designed to achieve a minimum anode-to-sample distance of 6 mm, with an anode to aperture distance of 4.5 mm.

A single WDS channel was incorporated into the prototype instrument to demonstrate functionality. The long range plan was to incorporate several identical channels around the sample which would be used to either increase the available count rate required to measure film thickness and composition, or to provide other elemental analysis (e.g., C, O, F).

The alignment issues associated with the WDS design were resolved by mounting the mirror assembly to the chamber lid, and adding some flexibility to the mirror mount design which permitted mirror angle and vertical position to be adjusted during optical alignment procedures.

4.4.2 Materials Issues

The main vacuum chamber, originally fabricated by MDC, consisted of 304 stainless steel. A new lid, sample holder and stage translation components were fabricated from aluminum. Standard vacuum design procedures were followed, including the use of venting for blind bolt holes to eliminate virtual leaks during pumpdown. The stepper motor for stage translation was disassembled and degreased in order to improve its vacuum compatibility.

The vacuum requirements were set by the need to minimize absorption of the lowest energy x rays which needed to be examined, in this case N-K and Ti-L. Preliminary pumping with a roughing pump indicated that 100 mTorr could be achieved within two minutes, and 10 mTorr after 30 minutes. The residual air consists predominantly of N₂, so the Ti-L line at 450 eV, which would be absorbed most by the nitrogen, was used to calculate the maximum allowable pressure. The transmittance, T, can be expressed as a function of pressure, P, by:

$$T = \exp\{-[2 A_N \mu_N x] / 22,400 (P / P_0)\} \quad (4.4.1)$$

where P₀ is atmospheric pressure, A_N is the atomic weight of nitrogen, μ_N is the mass absorption coefficient of nitrogen at Ti-L, and x is the path length in the chamber. Substituting in the

maximum path length from sample to WDS detector, $x = 16$ cm, and assuming values of $P_0 = 760$ Torr, $A_N = 14$ gm, $\mu_N = 24,800$ cm²/gm, $P = 100$ mTorr yields a transmittance of 94%. At 10 mTorr the transmittance increases to 99.6%, so the roughing pump was deemed satisfactory.

The low-grade vacuum requirement permitted the use of Viton o-ring seals, instead of copper gaskets, for the flanges on the top and sides of the chamber. A copper mesh filter was installed between the roughing pump and the chamber to reduce backstreaming of oil from the pump.

The gas flow and vacuum system for filling the proportional counter detector was transferred from the ARACOR x-ray calibration chamber, to insure low risk operation. Figure 4.4.3 is a diagram showing how the system is connected to the main vacuum chamber.

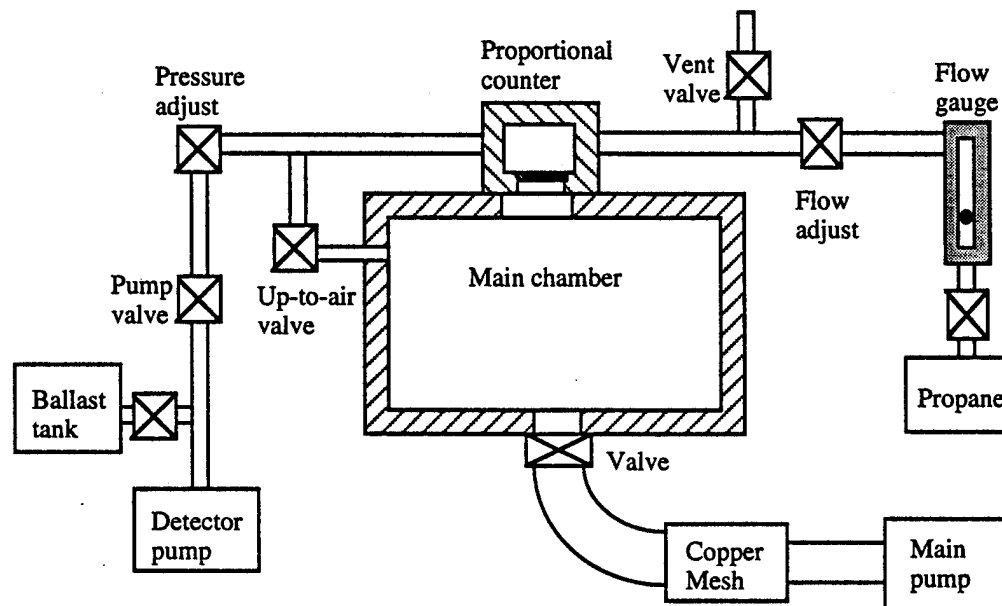


Figure 4.4.3. Vacuum system for main chamber and proportional counter detector.

During pumpdown of the main chamber, all valves were closed except for the up-to-air valve. In this way, both the detector and main chamber were evacuated, while maintaining a positive pressure differential from back to front of the fragile proportional counter window. After pumpdown, the up-to-air valve was closed, and propane gas was slowly admitted to the detector. After achieving the desired working pressure of ~100 Torr, a valve was opened to the detector vacuum pump which continuously pulled gas through the detector, maintaining the desired pressure.

For shutdown, the gas flow was shut off, allowing the detector to be evacuated. The vacuum pump was then valved off and the detector reconnected to the main chamber through the up-to-air valve. The main chamber could then be brought up to atmospheric pressure by admitting air through the vent valve, which again maintained a positive differential across the detector window.

The purpose of the ballast tank was to help reduce rapid pressure fluctuations arising from variations in pumping speed of the detector pump.

The x-ray tube collimator was fabricated from molybdenum so that no extra unwanted fluorescence lines would be created, other than the Mo-L (2.9 keV) characteristic lines emitted from the anode. As previously noted, the Si(Li) detector was fitted with an aluminum collimator to restrict the line of sight to the immediate vicinity of the sample.

4.4.3 System Integration and Design

The system was integrated in stages, beginning with the assembly and testing of the vacuum pumping system and stage motion assembly. The stage vertical height range was provided with a final manual adjustment of ± 1 cm in order to accommodate uncertainties in final positioning of the Si(Li) detector and x-ray tube. The centering of the Si(Li) detector in the mounting flange and the precise angle of entry could not be well characterized before arrival of the detector. In addition, the cone angle of the front end of the x-ray tube was not well defined in the early stages of planning, because of the uncertain effect it would have on focusing of the electron beam onto the anode. This angle uncertainty was translated into a height uncertainty for the x-ray tube collimator, since the chamber lid and x-ray tube mounting assembly had to be fabricated before the x-ray tube could be delivered.

Radiation safety was provided by designing a small enclosure which was mounted in the center of the chamber lid around the tube. The anticipated x-ray levels were expected to be low, because of the low excitation voltage of 20 kV and the fact that the anode region of the tube was located 8 cm below the top of the chamber lid with the rear end of the x-ray tube providing shielding. Concern about heat dissipation from the x-ray tube was accommodated by introducing thermocouple wires for monitoring temperature during operation, and allowing for the use of a fan to cool the x-ray tube enclosure.

There was some concern about heating and background radiation flooding the Si(Li) detector, because of its close proximity to the x-ray tube. The close coupling of tube to sample implied that there was no way to shield the detector from a direct view of the x-ray tube collimator, which might produce unwanted fluorescence and thermal radiation. However, this did not prove to be a problem.

4.4.4 System Specifications

The system performance goals may be summarized as follows. In terms of the expected efficiency of geometrical coupling between source, sample, and detector, the system input was specified by an x-ray tube power loading of 10 watts, over a range from 5 to 20 kV, with a 150- μ m focal spot

on the x-ray tube anode. The specifications are summarized in Table 4.1.2. The 6-mm distance between anode and sample, with 4.5-mm spacing between anode and collimator aperture, was designed to achieve efficient flux delivery onto the sample, with an achievable spot size of 100 μm when a 35- μm aperture was mounted in the collimator.

The close coupling between sample and the 30-mm² Si(Li) detector, at a distance of 19.2 mm and with a 30° takeoff angle, was designed to achieve efficient collection of the sample fluorescence. The remaining specifications (see Table 4.3.1) were designed to provide sufficient energy resolution and a low enough noise floor (with suitable electronics) to detect the N-K and Ti-L emissions between 390 and 450 eV.

Vacuum requirements were set at 50 mTorr to avoid attenuation of Ti-L radiation, and thermal conduction of heat away from the anode was expected to achieve a less than 50°C operating temperature at the end of the x-ray tube.

The sample X, Y and Z stage motion was sufficient to scan various samples, and optimize the geometry of the prototype.

5.0 INSTRUMENTATION ASSEMBLY AND EVALUATION

5.1 X-RAY SOURCE

5.1.1 Subcontract Work

The x-ray tubes were manufactured by Bill Hershy (ARPES), in part at ARACOR, with many specialized operations being performed at local shops in the near vicinity.

Three work areas were set aside for the subcontractor at ARACOR. The first consisted of a small office area suitable for design work and storage of parts. A second area was set up with a laminar bench for parts assembly and filament winding, a spot welder for assembling the electron gun, and a brazing area with two stations for performing either hydrogen or vacuum brazing. The brazing stations were used for attaching the anode/window to the x-ray tube and for brazing together other components. The subcontractor supplied the RF power supply, vacuum pumping station, and chambers for brazing, while ARACOR supplied the hydrogen gas flow control system and appropriate electrical and water utilities.

Figure 5.1.1 shows the system implemented by ARACOR for controlling the hydrogen delivery for brazing. When the solenoid is not energized, N₂ normally flows into the brazing chamber. However, it will energize and switch to H₂ gas when the thermocouple reads a high temperature from H₂ burn-off. With this control, the H₂ will automatically switch off if the flame should be extinguished or the power fails.

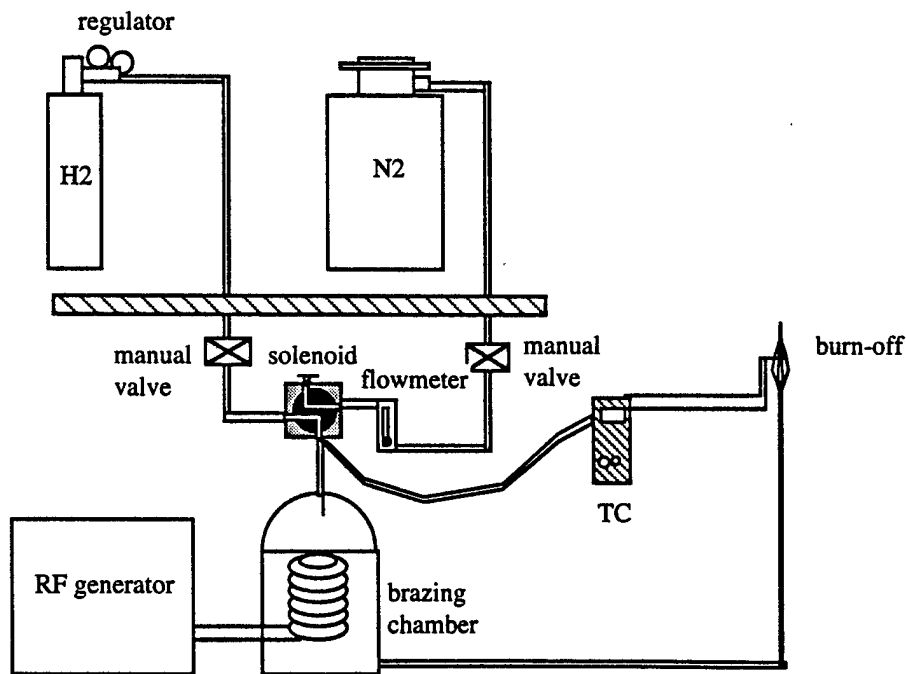


Figure 5.1.1. System used to regulate hydrogen flow through the brazing chamber.

A third room was equipped with a vacuum oven for baking out the x-ray tube, a high voltage power supply and oil bath for processing the tube at high voltage, and a torch for sealing the tube. A separate table was used for potting the finished x-ray tube in insulating rubber. Operations performed outside of ARACOR under supervision of the subcontractor included the machining of metal parts for the tube and for fixtures, production of the metal-to-glass seal, and forming of the glass/electrode assembly. Procurement of the high voltage supply, as well as special cabling and connectors required to power the x-ray tubes, was carried out by ARACOR under supervision of the subcontractor. The subcontractor also had access at ARACOR to a chemical area with fume hood, cleaning solvents, and an ultrasonic cleaner.

Several iterations were required to produce acceptable components for the final x-ray tube. For example, the correct brazing temperature and part fixturing had to be developed to produce sealed beryllium windows which were vacuum tight. An independent filament supplier had difficulty meeting the necessary deadlines for delivery, so the subcontractor decided to wind the filaments himself. Selection of the correct filament diameter and number of turns to match the filament power supply specifications on voltage and current required a few iterations to produce filaments which would not easily burn out.

The first tube was ready for trial by the 1st of August, 1995. The filament burned out on this tube after two weeks of operation. The tube was then supplied with a new filament and two additional tubes were made available by mid-September.

5.1.2 Component Evaluation

The first x-ray tube (#1) was available for testing before the Si(Li) detector could be incorporated into the measurement chamber, so the initial evaluation was performed with an Amptek XR-100T detector. This is a Peltier-cooled PIN-diode detector with an energy resolution of 250 eV at Mn-K. The detector has a 3-mil beryllium window, which made it useful only for elements as light as aluminum.

A vacuum feedthrough was constructed so that the detector could be used in vacuum, with the geometry for the initial measurements as shown in Figure 5.1.2. A 100- μ m pinhole was used in the collimator, and the stage was brought into a position which provided nearly a 1:1 imaging of the x-ray focal spot onto the sample.

The temperature of the x-ray tube adjacent to the anode was measured with a thermocouple wire attached to a vacuum feedthrough. The temperature reached a relatively stable value of 32° C (room temperature 20° C) in about two hours with a power loading of 10 watts, and the maximum temperature did not vary significantly when operated in air or vacuum. The temperature dropped

fairly rapidly when the power was removed, suggesting a path with high thermal conductivity away from the anode.

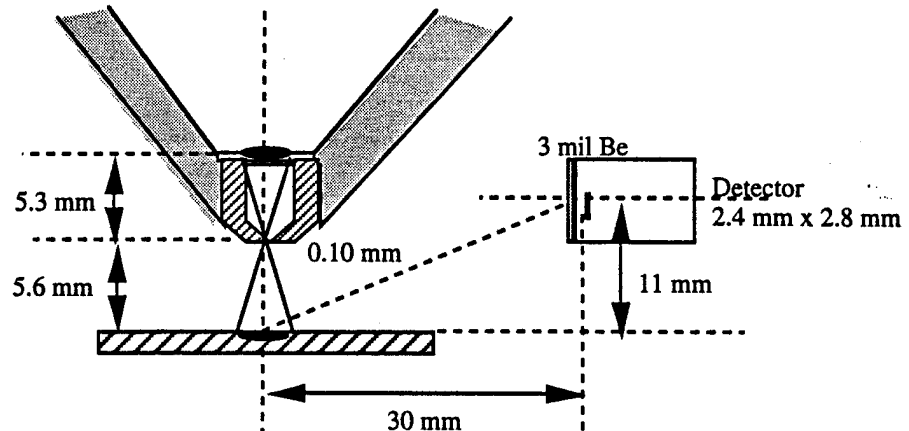


Figure 5.1.2. Geometry used for initial evaluation of focal spot size and count rate.

The focal spot size was estimated by scanning the edge of a silicon wafer through the projected x-ray focal spot with the motorized stage. Since the aluminum stage has an alodine finish, which is produced from nickel phosphate, the count rate under the Ni-K peak was monitored as a function of stage position, and the derivative of count rate with respect to position was used to derive the spot profile, as shown in Figure 5.1.3. Figure 5.1.4 illustrates the result for two measurements which differ with respect to the polarity of the x-ray tube filament hook-up. Note that the total spot diameter is approximately 1.2-mm wide, and the different polarities produce slightly different shapes and intensities for the same anode current. The implied focal spot on the anode appears to be much larger than the specified diameter of 0.15 mm.

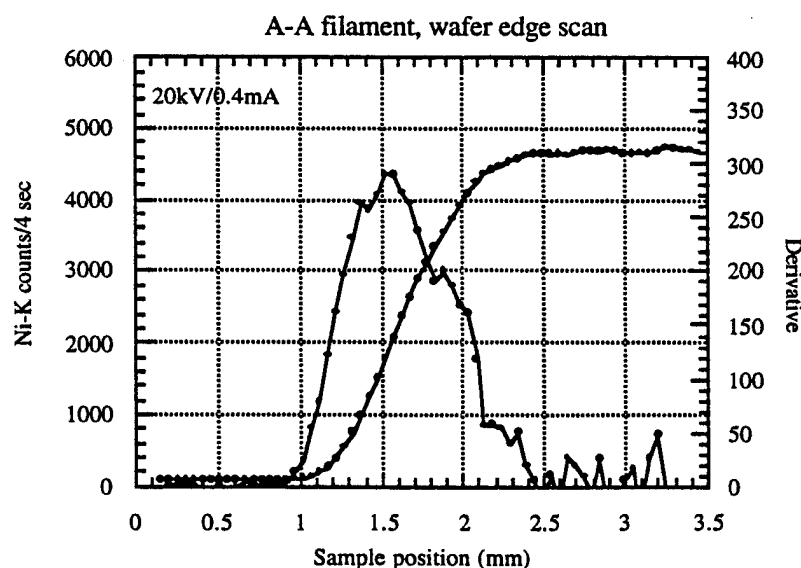


Figure 5.1.3. Focal spot size derived from edge scan of silicon wafer.

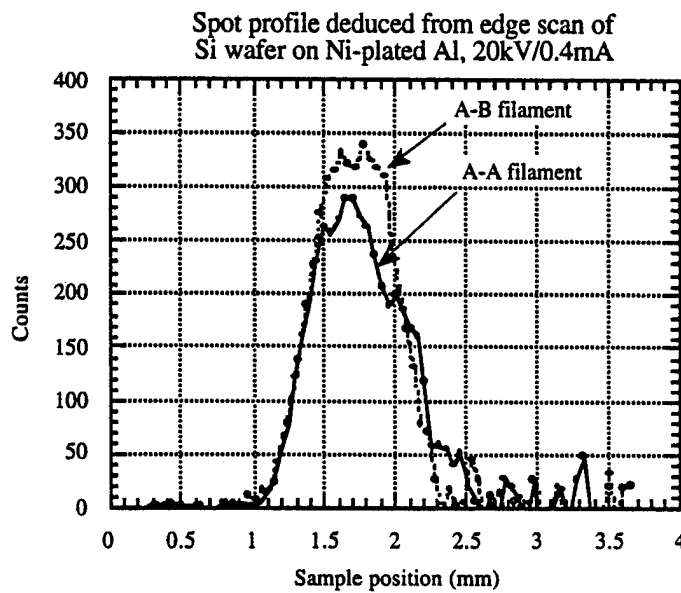


Figure 5.1.4. Change in focal spot with polarity change on filament.

Next, spectra were collected from aluminum and silicon samples in order to evaluate the x-ray tube output for comparison with theory. The spectrum of an aluminum plate, shown in Figure 5.1.5, gives evidence for alloying with iron, manganese, and chromium, along with some postulated potassium and calcium content.

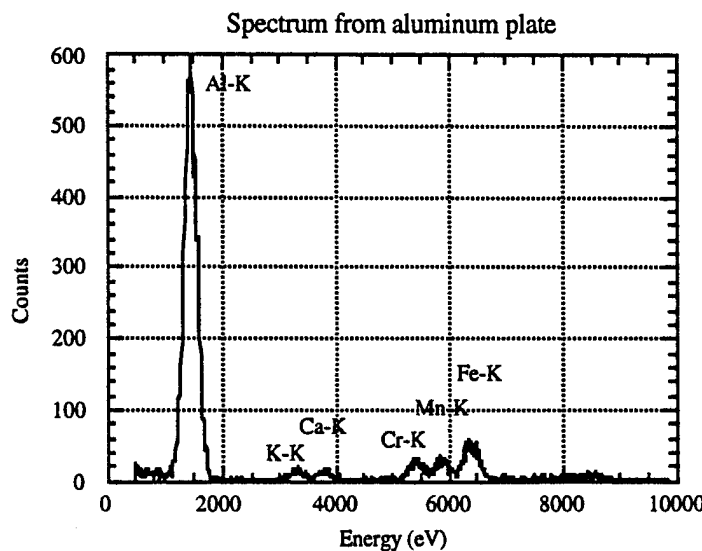


Figure 5.1.5. Spectrum of aluminum plate taken with PIN-diode detector.

The silicon spectrum, Figure 5.1.6, shows the characteristic silicon peak and a small nickel fluorescence peak.

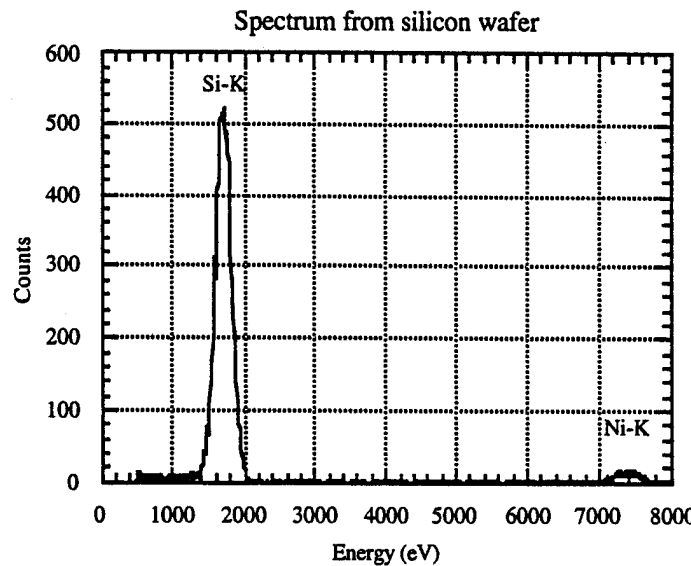


Figure 5.1.6. Spectrum of silicon wafer taken with PIN-diode detector.

The dependence of count rate on excitation voltage and current was then measured for the aluminum and silicon samples. For these measurements, a single channel analyzer (SCA) was set up to measure only the counts under the peak of interest. Figure 5.1.7 illustrates typical data for the silicon sample.

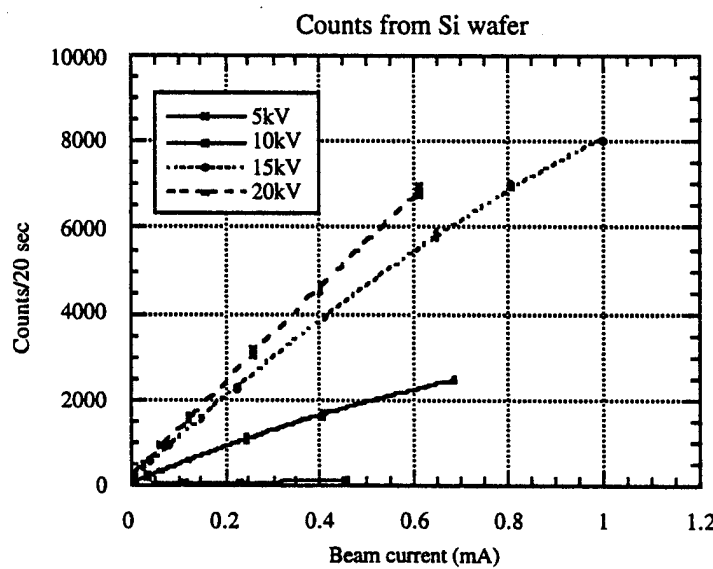


Figure 5.1.7. Count rate dependence on voltage and anode current.

Normalizing the count rates to the power loading on the anode yields the voltage dependence shown in Figure 5.1.8. The initial drop in count rate per watt is explained by a small offset of +12 μ A in the measured beam current, while the decrease at higher beam currents is not easily understood (change in slope of count rate shown in Figure 5.1.7). Note that the count rate per watt at 20 kV is less than at 15 kV. It is suspected that this effect may be due to non-linear count-rate effects in the PIN-diode detector and SCA electronics. The opposite effect (but much smaller as shown in Figure 5.1.18) was observed when another tube (#3) was later tested with the Si(Li) detector, after the dead-time handshaking in the electronics had been carefully setup and evaluated.

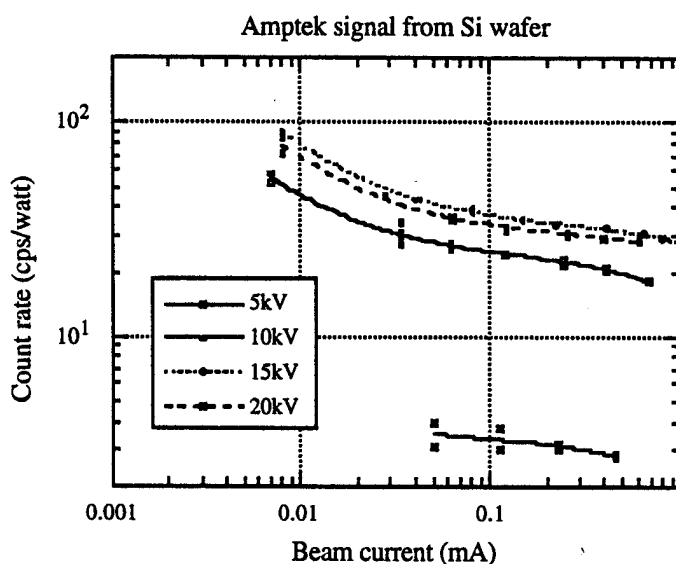


Figure 5.1.8. Count rate for silicon normalized to power loading on anode.

Using the geometry shown in Figure 5.1.2 and Excel spreadsheets to predict the x-ray tube output spectrum and fluorescent signals, the expected count rates from the aluminum and silicon samples were predicted as a function of excitation voltage. Figure 5.1.9 compares the measured count rates with those predicted from the spreadsheets. Most count rates were within a factor of two of the predicted values. The measured ratios for both samples decreased at 20 kV whereas the predicted count rate was expected to increase. This could be explained by an anode thickness which is thinner than the modeled value of 1.25 μ m. In that case, more electrons would penetrate the anode at the higher voltage, resulting in a decreased excitation of the anode material. The systematic deviation of the curves from the predicted shape may also indicate deviations from the predicted spectrum, perhaps due to tungsten deposition, from the filament, on the anode or emission from copper surrounding the anode (see below).

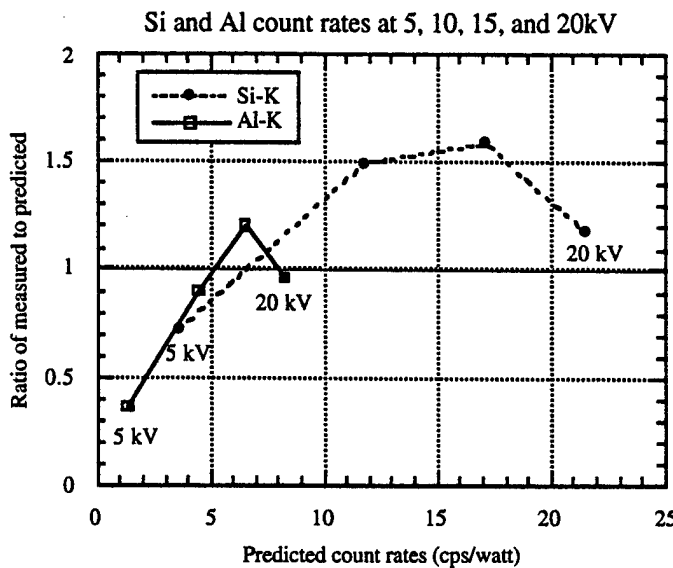


Figure 5.1.9. Comparison of measured and predicted count rates from samples.

The same phenomenon was later observed while analyzing a nickel sample, except that the maximum count rate peaked at 20 kV. The tube was run up to 25 and 30 kV, where the absolute (i.e., not ratioed to predicted) nickel count rate was observed to drop. This is interpreted to be due to the electrons exciting the molybdenum film prior to depositing all their energy, as a result of the molybdenum film being thinner than anticipated. A Monte-Carlo program, originally developed by David Joy (available commercially from Small World, San Mateo, CA), was used to visualize the processes involved as the electrons impact the molybdenum film. A variety of Monte-Carlo simulations were run with different film thicknesses and different values of excitation kV. Two of the simulations are shown in Figures 5.1.10 and 5.1.11.

Judging from these and other simulations, the actual thickness of the molybdenum film is about 0.8 micron, rather than the specified value of 1.5 microns. One can see that at 25 kV many of the electrons penetrate through the thin-film target into the beryllium-window substrate. This value also corresponds to the estimate of the mean electron range of 0.8 microns, as shown in Figure 4.1.9. As it turns out this value may have been the optimal one for operating this tube at 20 kV and below. If the target were any thicker, there would be increased absorption of the bremsstrahlung and characteristic x rays generated within the target.

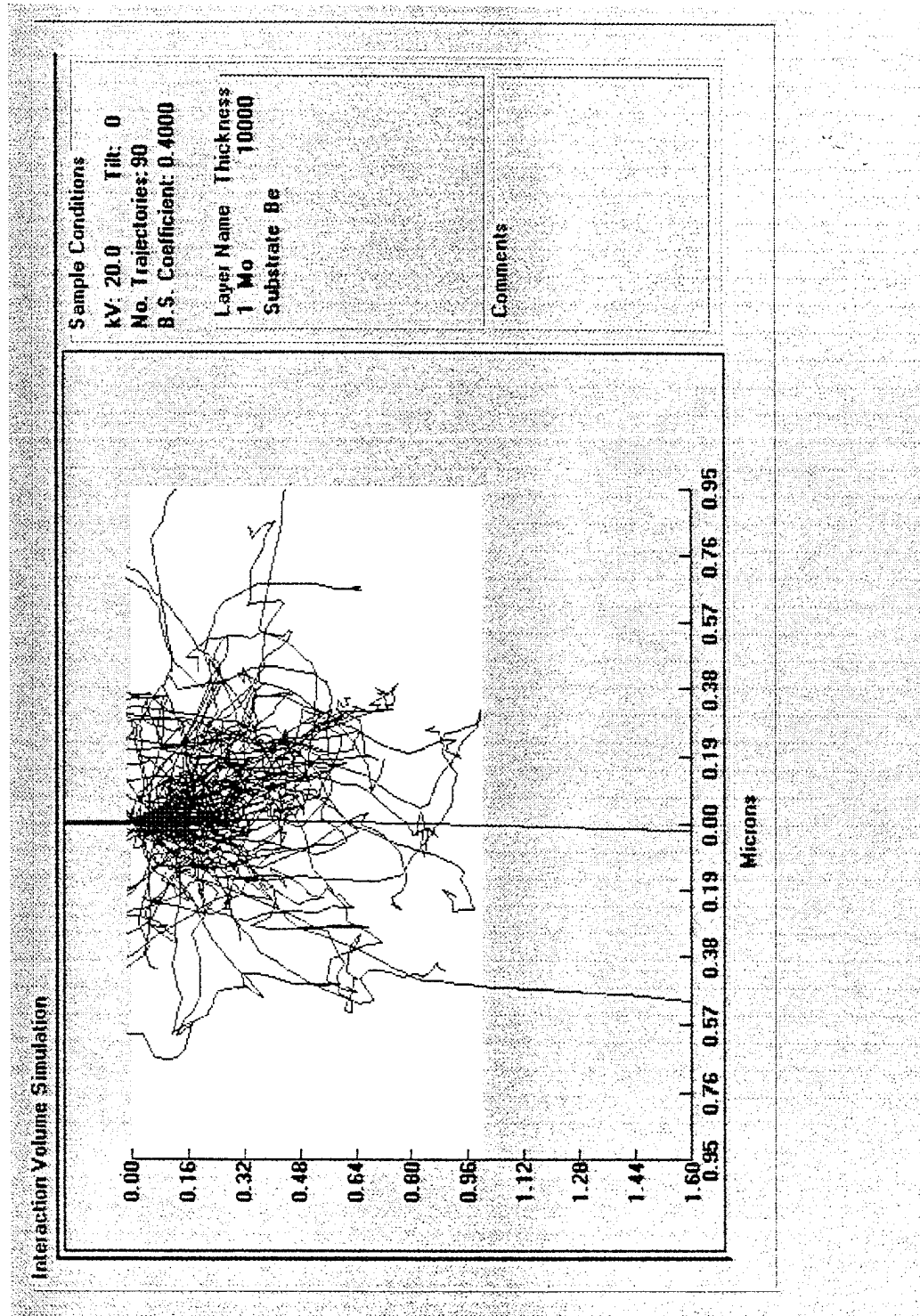


Figure 5.1.10. Monte-Carlo simulation of 20 kV electrons in a 1-micron molybdenum film.

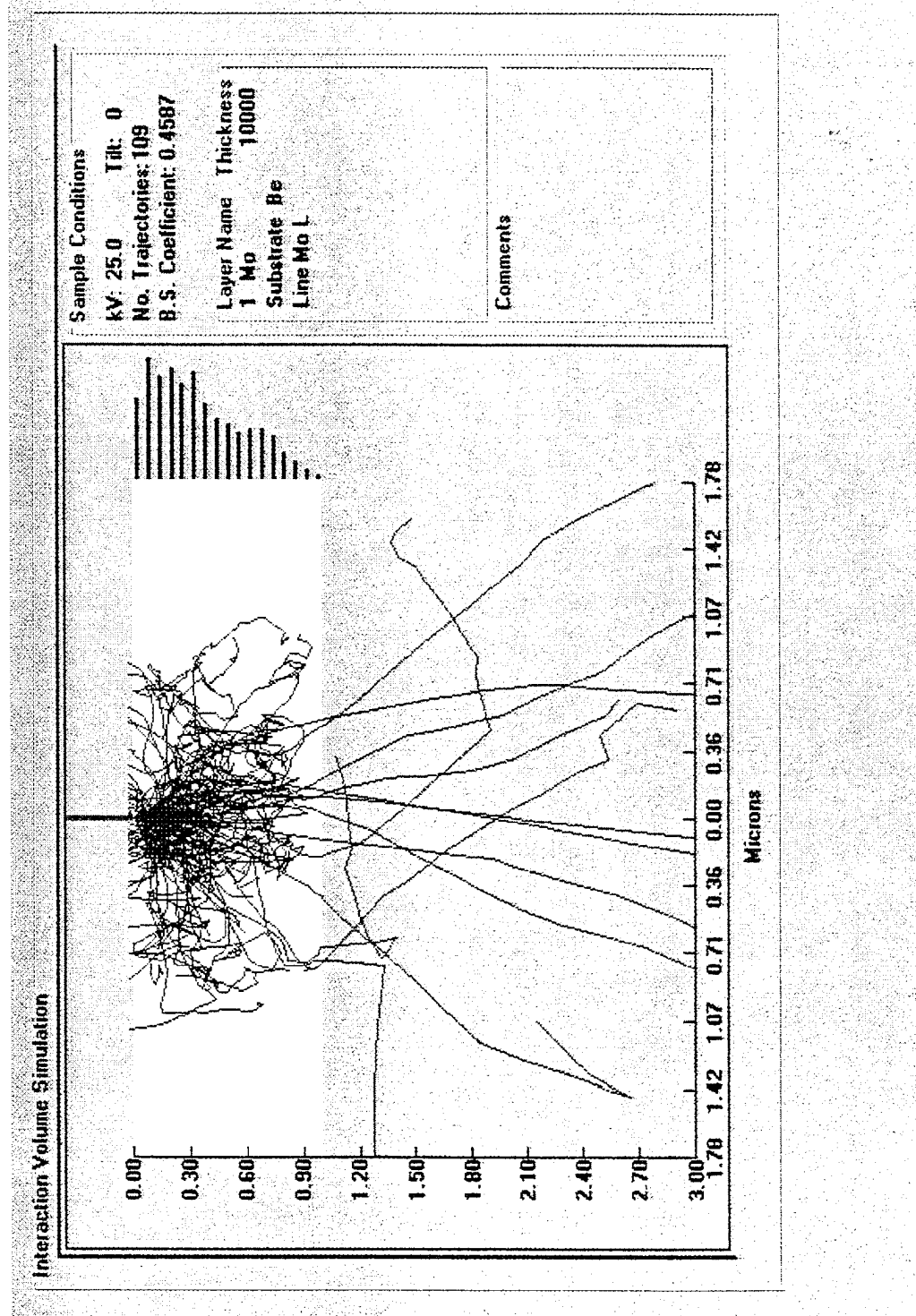


Figure 5.1.11. Monte-Carlo simulation of 25 kV electrons in a 1-micron molybdenum film.

Tube #1 was run overnight to measure the count rate stability, but the filament burned out after ~18 hours of continuous running, as shown in Figure 5.1.12. The steady decrease in count rate is presumed to result from evaporation of tungsten from the filament onto the anode, with subsequent burnout. The estimated total lifetime of the tube was 60 hours. Discussions with the subcontractor indicated that the tube had been designed to run at a maximum current of 0.5 mA, rather than an assumed fixed power loading of 10 watts over the voltage range of 5 to 20 kV.

Also, we had operated this tube at 25 and 30 kV, for a few hours, in order to do some experiments and to deliberately stress the tube beyond its operating range to determine any short-term catastrophic failure mode. The subcontractor also said that, since the tube had not been baked out and outgassed at 30 kV, operating at 30 kV would tend to degrade the vacuum environment. After this failure, and repair, we maintained the tubes within the designed operating range.

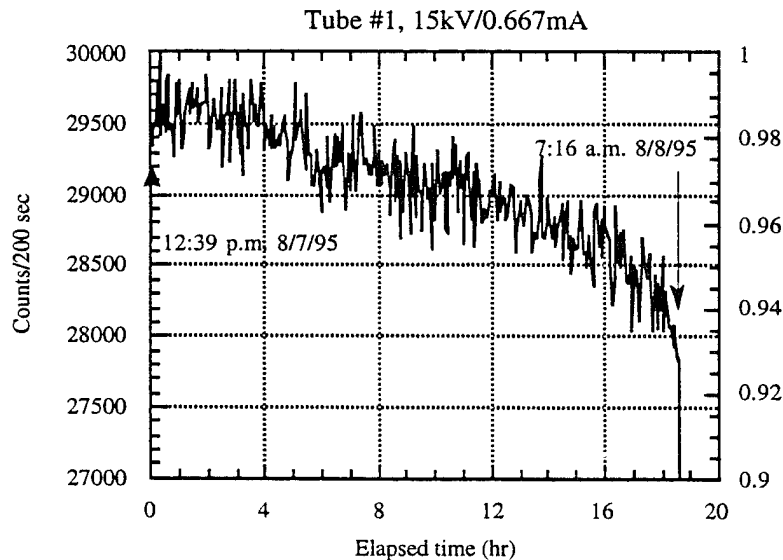


Figure 5.1.12. Count rate variation from tube #1 run overnight.

Tube #1 was rebuilt with a new filament and two additional tubes numbered #2 and #3 were produced. Figure 5.1.13 shows two of the x-ray tubes, with a collimator screwed into tube #1. To evaluate the focal-spot sizes, pinhole photographs (Figure 5.1.14) were taken of all three tubes at operating voltages of 10 and 20 kV, and with the filament hooked up with two different polarities.

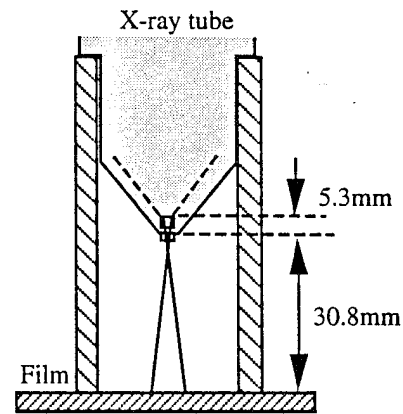
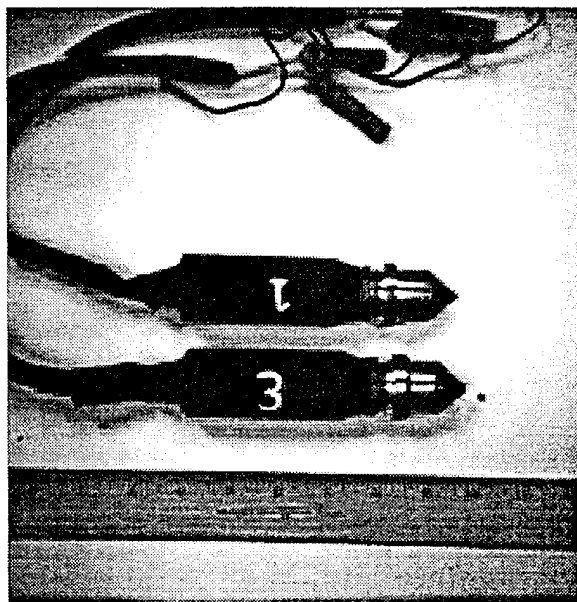


Figure 5.1.13. Photograph of x-ray tubes and pinhole photo geometry.

The geometry used to take the pinhole photos indicates a magnification factor of about 5.8x. Therefore, the 15-mm diameter of the images in the photographs, represents a true dimension of 2.6 mm, which closely matches the "inner" diameter of the window from the engineering drawings.

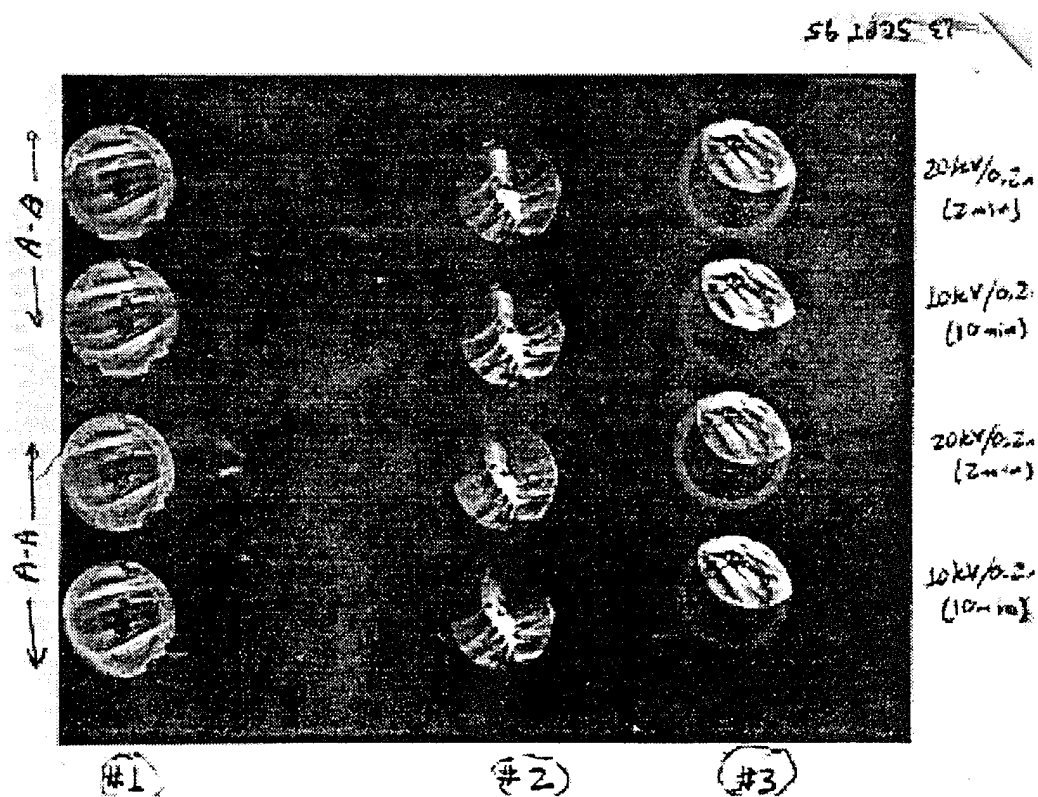


Figure 5.1.14. Pinhole photographs of focal spot for the three x-ray tubes.

X-ray tube #1 shows a pattern consistent with a defocused x-ray beam. The small dark vertical patch in the center of the image corresponds to a visually detectable deposit on the outer side of the beryllium window. This is thought to consist of decomposed oil which was deposited by the high temperatures developed during the high voltage processing in an oil bath. Tube #2 shows better focusing of the electron beam into a spot with a central core measuring roughly $3 \times 5 \text{ mm}^2$ on the photograph, or $0.5 \times 0.9 \text{ mm}^2$ after correcting for the magnification. Streaks emanating from the spot appear to be correlated with the focusing from individual coils in the tungsten filament. Tube #3 shows a misalignment of the electron gun as well as defocusing. The subcontractor acknowledged that a misalignment had occurred when the gun assembly was welded to the anode assembly, due to overheating and sagging of the glass envelope.

Only subtle changes are visible in the focal spot pattern for the different filament polarities and voltages examined. For example, for tube #2, the A-B (see Figure 5.1.17) filament connection (upper two photos) puts a greater fraction of the electron beam into the upper section of the focal spot than the A-A connection (lower two photos).

Tubes #1 and #3 display a bright outer ring which was postulated to arise from electrons drawn to the copper shoulder internal to, and supporting, the beryllium window. This was supported by comparing the spectra from tubes #2 and #3 taken with the Amptek detector and a silicon-wafer sample, Figure 5.1.15. Tube #3 displays a backscattered Cu-K peak which is not apparent in the tube #2 spectrum. Since the spectra were taken with the chamber at atmospheric pressure, they show an Ar-K peak in addition to the expected Si-K peak and backscattered Mo-L radiation from the anode. The broad peak at 8500 eV in both spectra represents bremsstrahlung from the anode which happens to be diffracted from the silicon crystal into the detector.

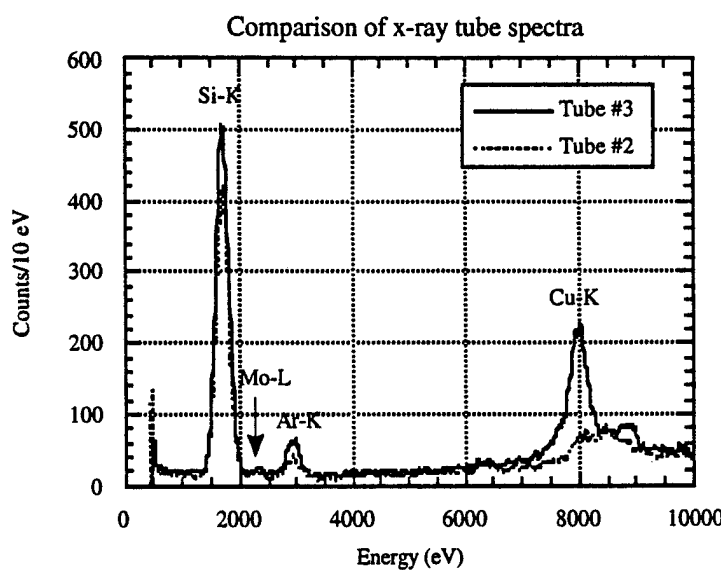


Figure 5.1.15. Appearance of a copper peak in the silicon spectrum from x-ray tube #3.

An indirect comparison of flux from the x-ray tubes was made by looking at the count rate from a nickel sample at a fixed voltage. Figure 5.1.16 shows that all the x-ray tubes generate comparable count rates, except for the first tube which was initially brighter by a factor of 3.6x before the filament burned out.

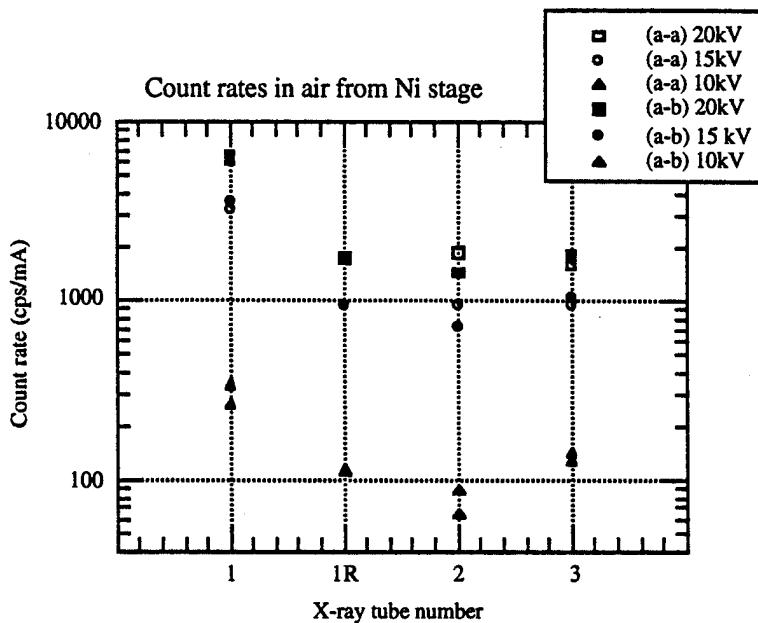


Figure 5.1.16. Comparison of x-ray tube efficiencies for exciting Ni-K x rays.

It may be that this tube had a higher proportion of Cu-K radiation, which would have been very efficient at exciting the measured Ni-K count rate. The expected Mo-L radiation from the anode at 2.3 keV does not contribute to the excitation of Ni-K, whose absorption edge is at 8.3 keV, whereas the Cu-K β line at 8.9 keV does. Note the variable effect of switching the filament polarity. It was postulated that since one end of the filament is connected to the conical focusing electrode, the filament polarity might affect the degree of focusing by either attracting or repelling the emitted electrons, as shown in Figure 5.1.17.

However, the pinhole photos suggest that this picture is oversimplified. Note that the filament leads were arbitrarily labeled A and B during construction, so the actual potential on the conical electrode with respect to the filament is unknown.

After the Si(Li) and associated electronics were installed, another test of the linearity of the tube (and power supply) current control was performed by measuring the generated fluorescent and scatter count rate from a nickel sample in the vacuum chamber. The plot of total spectrum count rate against tube current (mA) is shown in Figure 5.1.18.

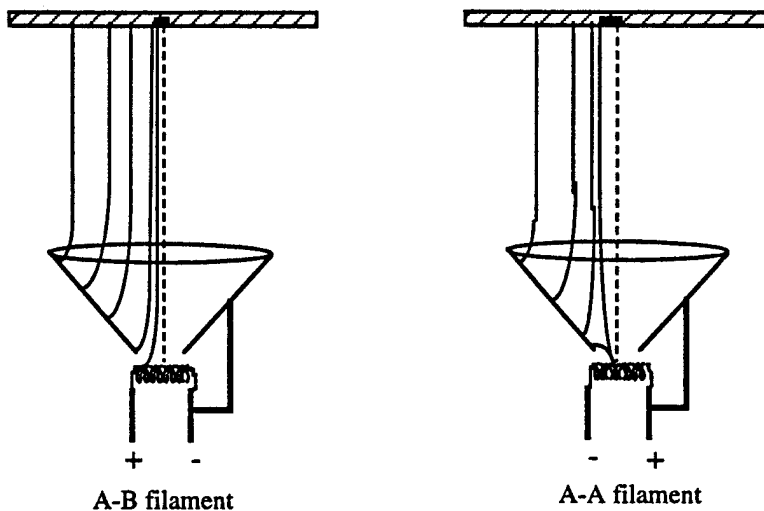


Figure 5.1.17. Possible mechanism for effect of filament polarity on observed count rates.

The tube (serial number 3) was operated at 5 kV for this test. Since this test covered the count-rate range from 2,600 up to 26,000 c/s, this was also a combined test with the linearity of the EDS detector electronics. The curve shows a slight upward trend in count rate, with increasing current. It is not clear whether this slight non-linearity arises from the tube and high-voltage power supply, or from the detector electronics. At this high a count rate, with a time-constant setting of 8 microseconds, the dead time was at about 80%, which is well beyond the recommended operating range. However, since the measured deviations were quite small, this does indicate a degree of confidence in operating over a wide dynamic range. The extrapolated offset was below 0.01 mA (which is below the setting accuracy of the power supply). Tests of another tube (serial number 1) showed a possible offset of 0.01 mA. This is normal and quite acceptable behavior. It is very difficult to operate and control any x-ray tube and power supply at low beam currents.

In order to test the stability of the tube, as far as output flux is concerned, it was necessary to test the tube as part of the overall system. Figure 5.1.19 shows a typical stability run, for total spectral counts from the fluorescence of a nickel sample, over a period of about 16 hours. Each data point was 400 livetime seconds. The Amptek pin-diode detector (see Sections 4.3.1 and 5.3.1) was used for this particular test, as the Si(Li) detector was not ready at the time. The measured 1σ relative standard deviation (RSD) matches the theoretical (from Poisson counting statistics) value of 0.13%. Of course this test actually convolutes any instability of the detector and electronics within the measured flux variation. However, as expected, the variations are entirely due to counting statistics, and so for these counting times the tube (and detector) flux variations are not an issue. Typical specifications for x-ray spectroscopy tubes (and systems) are for a 1σ variation of 0.25 to 0.5% RSD over any 4-hour period. The measurements obtained in Figure 5.1.19 (and other measurements) exceed these specifications.

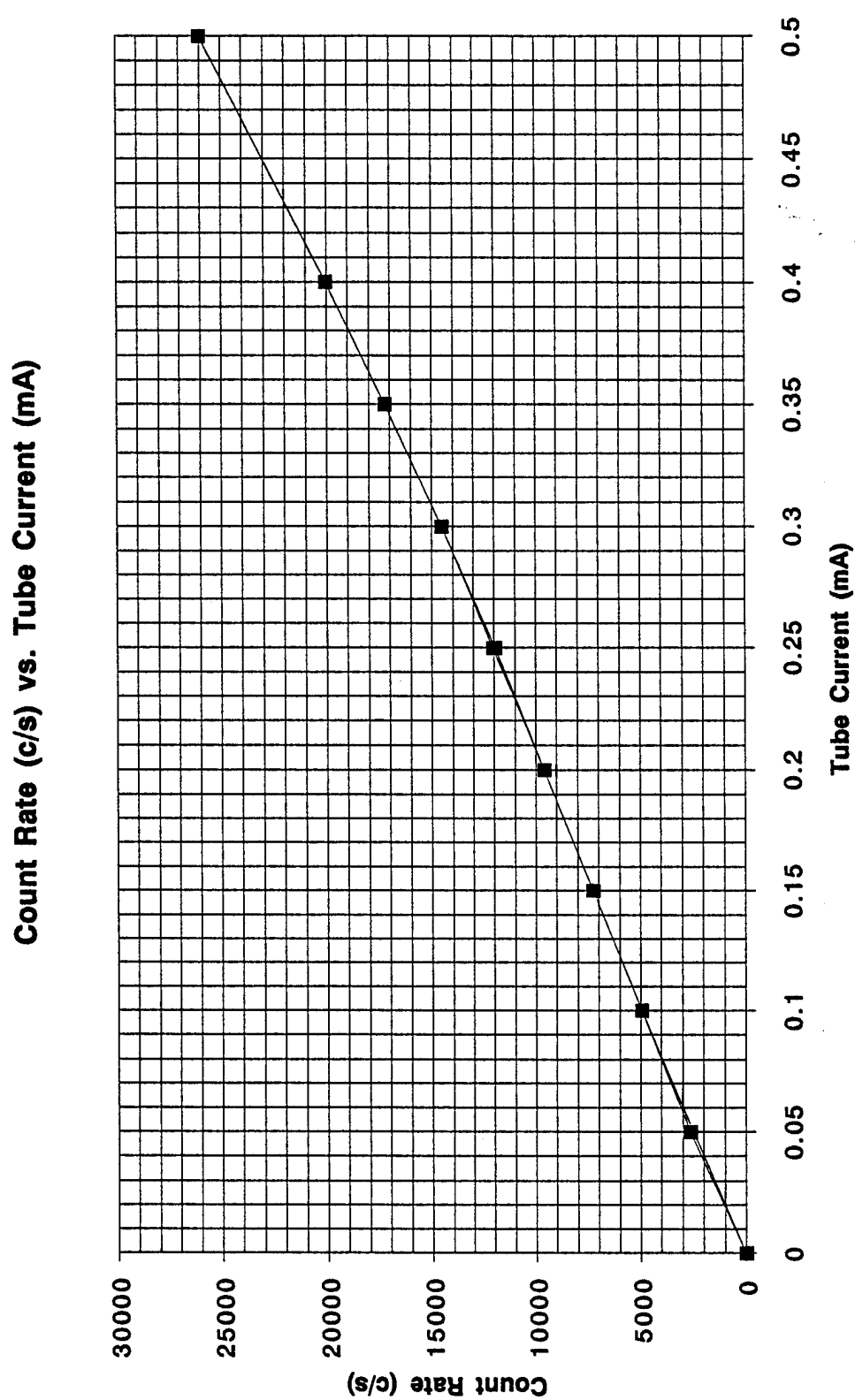


Figure 5.1.18. Count rate vs. tube current at 5 kV for tube #3.

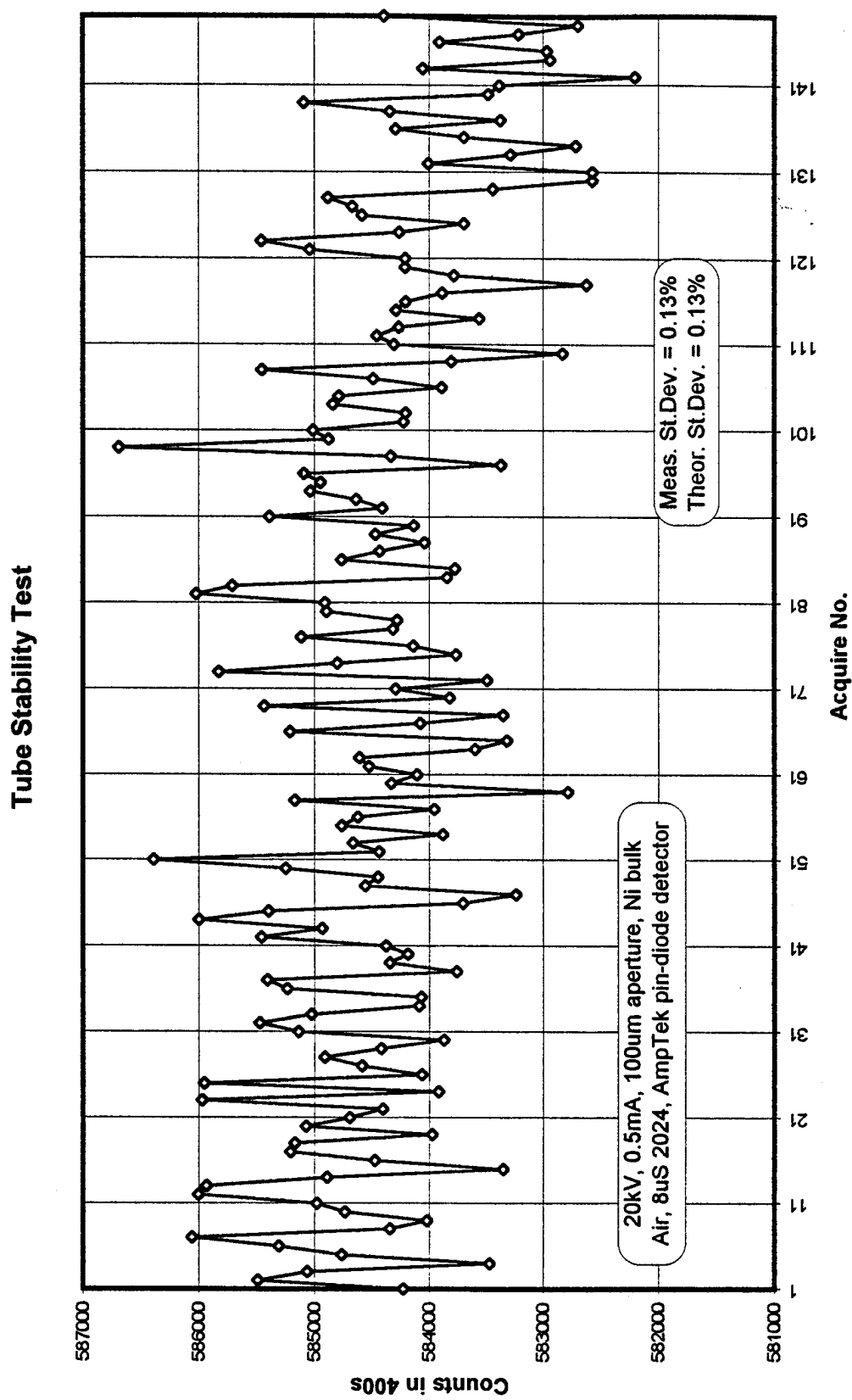


Figure 5.1.19. Tube stability test.

5.1.3 System Integration

In summary, the integration of the tube into the sample chamber proceeded smoothly. The heat loading was as predicted, and no external cooling was required. X-ray leakage tests showed no discernible radiation up to 30 kV operation, with or without a sample in place (high and low atomic number). The tube also operated in vacuum without any apparent degradation in the cooling of the anode. This indicates that the conductive paths are sufficient, and that any convective cooling of the anode, internally in the chamber, has a small effect.

5.2 WAVELENGTH-DISPERSIVE SPECTROMETER

5.2.1 Subcontract Work

The WDS mechanical assembly and the spherical substrate were produced through subcontractual arrangements with McKinney Engineering (of Sunnyvale, CA) and General Optics (of Azusa, CA). The mechanical assembly, consisting of the optic holder and the linear motion system, were fabricated by McKinney Engineering. The angular motion produced by these components was verified by measuring the dispersion of a reflected laser beam as a function of position of the linear feedthrough. Five precision spherical substrates, with the overall dimensions described in Section 4.2.1, were produced by General Optics. These optics were fabricated from silica with the following specifications: 1 Å RMS surface roughness, and a 60-40 scratch-dig (the typical standard for scientific research applications). The latter specification implies that no scratches above 6- μ m width were visible with optical inspection. Similarly, there were no visible digs, or craters, with a diameter greater than 0.4 mm. The vendor's metrology indicated that these specifications were met, and so the optic was accepted by ARACOR.

5.2.2 Detector Evaluation

A leak-tight seal between the MOXTEK boron-hydride window assembly and the proportional counter was achieved using Parafilm "M" laboratory film, sold by Ernest F. Fullam, Inc. A vacuum roughing pump with a copper mesh backstreaming filter achieved a vacuum of 40 mTorr in the chamber after a five-minute pumpdown, and no noticeable increase in pressure was found with an operating gas pressure of 150 Torr propane in the proportional counter. Continued cycling of gas pressure in the detector over a two-month period resulted in no noticeable degradation in window integrity.

The detector was operated at a nominal pressure of 100 Torr propane at a flow rate of 0.1 standard cubic feet per hour. The signal from the detector preamplifier was fed into a Canberra Model 10 Multichannel Analyzer, using slow pulse shaping and an amplifier gain of 5.0 x. Figure 5.2.1

shows the relationship between bias and gas pressure required to achieve 5 volt pulses for the indicated photon energy.

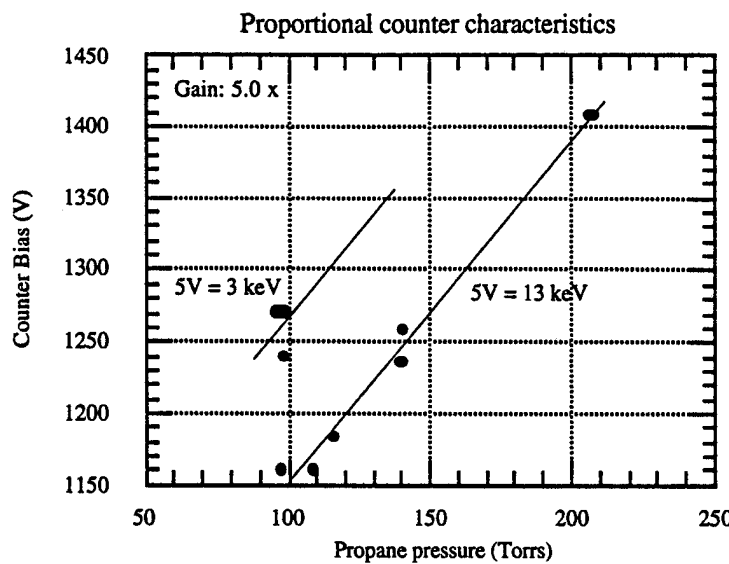


Figure 5.2.1. Detector bias as a function of operating gas pressure.

The predicted efficiency of the detector, including the effects of gas absorption and grid/window transmittance is shown in Figure 5.2.2. The transmittance drops sharply at the absorption edges of aluminum (73 eV) and boron (188 eV) which are present in the window, and rises sharply at the

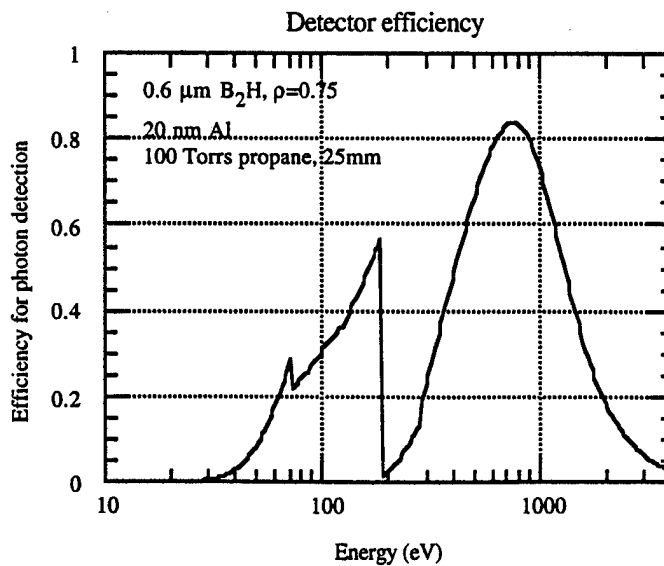


Figure 5.2.2. Predicted efficiency of detector for soft x rays.

absorption edge of carbon (283 eV) which is in the propane. The drop off in efficiency above 800 eV is due to decreasing absorption by the counter gas. It would have been possible to drop the detector efficiency further for the higher energy x rays by decreasing gas pressure to 50 Torr, but the rotary vane pump used to achieve the steady state gas pressure had insufficient pumping speed.

Initial spectra collected with the detector were difficult to interpret, because there was no simple way to perform an energy calibration. The detector had to be operated in a vacuum, and it was therefore deemed inadvisable to introduce a sealed isotopic source into the vacuum chamber for fear of destroying the source. There was also no line of sight between detector and x-ray source or sample, which would have provided a known energy of x rays.

Initial spectra were therefore collected in the full WDS configuration, with a glass substrate substituted for the multilayer mirror, and using a range of x-ray source voltages and samples to evaluate the effect on the spectrum. Figure 5.2.3 displays two spectra collected with 20 and 10 kV excitation on the source with a TiN sample.

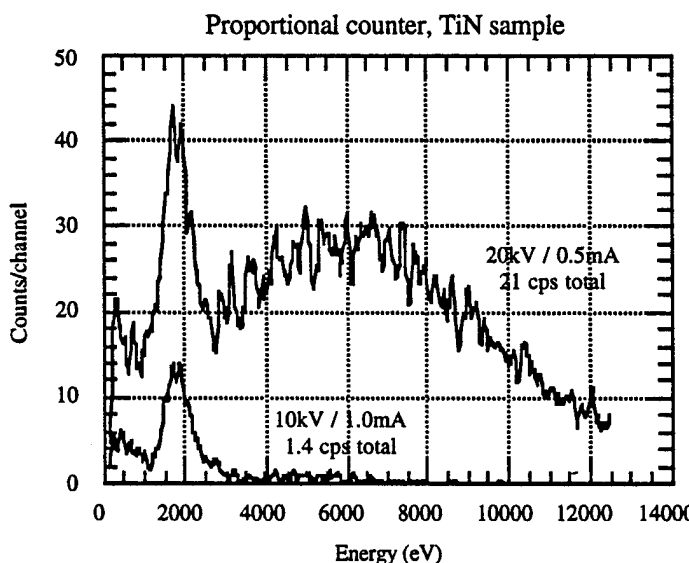


Figure 5.2.3. Initial spectrum collected with detector using TiN sample.

The large change in the broad, background peak with voltage suggested that the high-energy limits for each spectrum were associated with high-energy x rays entering the detector. Therefore, the highest energy pulses associated with the 10kV excitation were assigned an energy of ~10 keV, as shown. This suggested that the peak below 2000 eV might be Si-K, which could arise from fluorescence of the glass mirror (SiO_2) by the Ti-K x rays from the sample. This possibility was reinforced by covering the mirror with a piece of copper foil and reacquiring the spectrum, as shown in Figure 5.2.4.

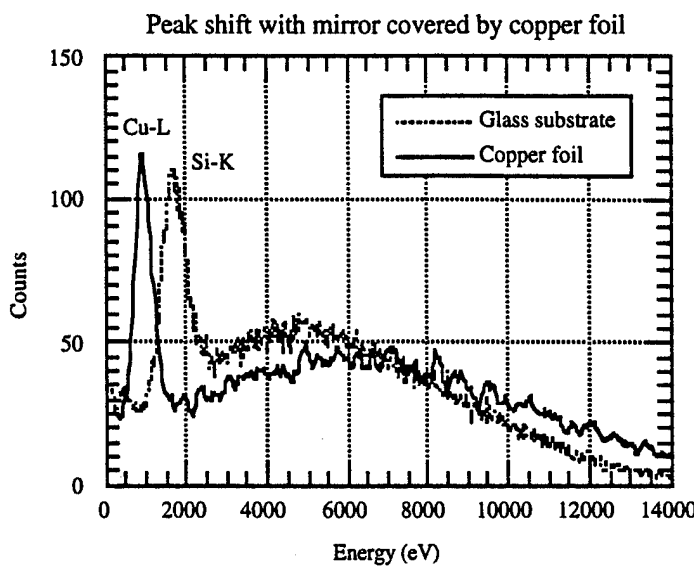


Figure 5.2.4. Change in peak position with mirror substrate covered with copper foil.

There is a shift in the low energy peak, consistent with a change from Si-K (1740 eV) to Cu-L (931 eV). In addition, the fluorescence intensity was found to be correlated with the sample placed under the x-ray source. For example, the Si-K peak intensity changed with sample according to the order Ti (4510) > Ni (7480) > Si (1740), which was expected since the closer the energy is to the absorption edge energy of silicon, 1839 eV, the more efficient it should be at exciting Si-K, as long as it is greater than the absorption edge energy. Similarly, the Cu-L peak intensity changed with sample according to the order Si (1740) > Ti (4510) > Ni (7480), which is consistent with an absorption edge energy of 1097 eV for copper.

A remaining question was how to interpret the source of high energy background. This was especially puzzling since the detector efficiency, Figure 5.2.2, was very low above 3000 eV where most of the background is seen to occur. A possible source for the background were high-energy x rays from the x-ray tube which would have to be scattered twice, once from the sample and a second time from the glass substrate, in order to reach the detector. An Excel spreadsheet was developed to estimate the spectrum and intensity of those scattered x rays which would enter the detector with the x-ray tube operating at a voltage of 20 kV, as shown in Figure 5.2.5. Values for the scatter cross sections were taken from McMaster et al [1969].

The integrated predicted flux of 10 photons/s was of the correct order of magnitude compared to the observed count rate of ~20 counts/s (see Figure 5.2.3), especially since other parts of the chamber surrounding the mirror could also contribute to scatter. However, the energy of scattered x rays falls outside the direct range of detection by the proportional counter, Figure 5.2.2, so it

was presumed that the detection must occur indirectly, for example by striking the back wall of the detector and causing secondary fluorescence of brass in the counter wall. The rear brass wall of the detector was replaced with a thin aluminum window, but this had no observable effect on the collected spectrum.

The conclusion developed from these studies was that the background peak is due to the emission of Auger electrons following the absorption of high energy, scattered x rays in the counter walls. These give rise to pulses with a broad energy spread below the incident x ray energies. Since electron emission is a surface effect ($<1\mu\text{m}$), it would not be expected to depend strongly on the actual composition or thickness of the rear wall of the detector. Methods for alleviating this source of background would include better shielding to limit the field of view of the detector for scattering surfaces and/or an extension of the detector with a grid and bias voltage to keep the Auger electrons out of the detection volume.

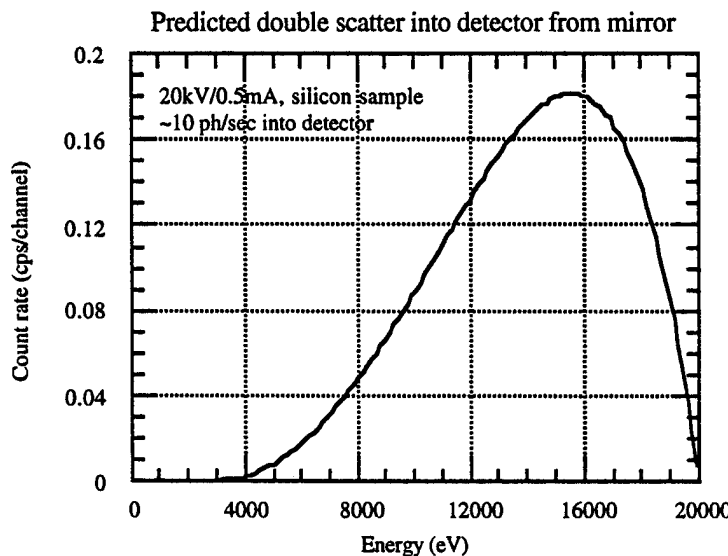


Figure 5.2.5. Predicted scatter of bremsstrahlung from x-ray tube to detector.

5.2.3 Multilayer Evaluation

The d-spacing gradient developed for the multilayer in the WDS channel was based on modeling the relative position of the sample and mirror, as shown in Figure 5.2.6.

The frame of reference used to specify sample spot and mirror position was tied to the x-ray tube centerline (shown dashed) and the bottom surface of the vacuum chamber lid, since both the x-ray tube and WDS mirror were attached to this lid. The sample-spot-to-lid, y_0 , could be adjusted by raising the vertical stage to bring the wafer into close proximity with the x-ray tube collimator, whose position was accurately measured. The mirror position was defined by the location of the

point, A, closest to the sample spot, and by a tilt angle for the glass substrate, ϕ_s . The mirror holder was nominally set at a 45° angle to the chamber lid, and the linear feedthrough position, w, was calibrated to determine the resulting coordinates (x_A, y_A) . Knowledge of the mirror radius of curvature, r, then provided sufficient information to derive the angle of incidence, θ , for each point, Z, along the surface of the optic for a given stage position, w.

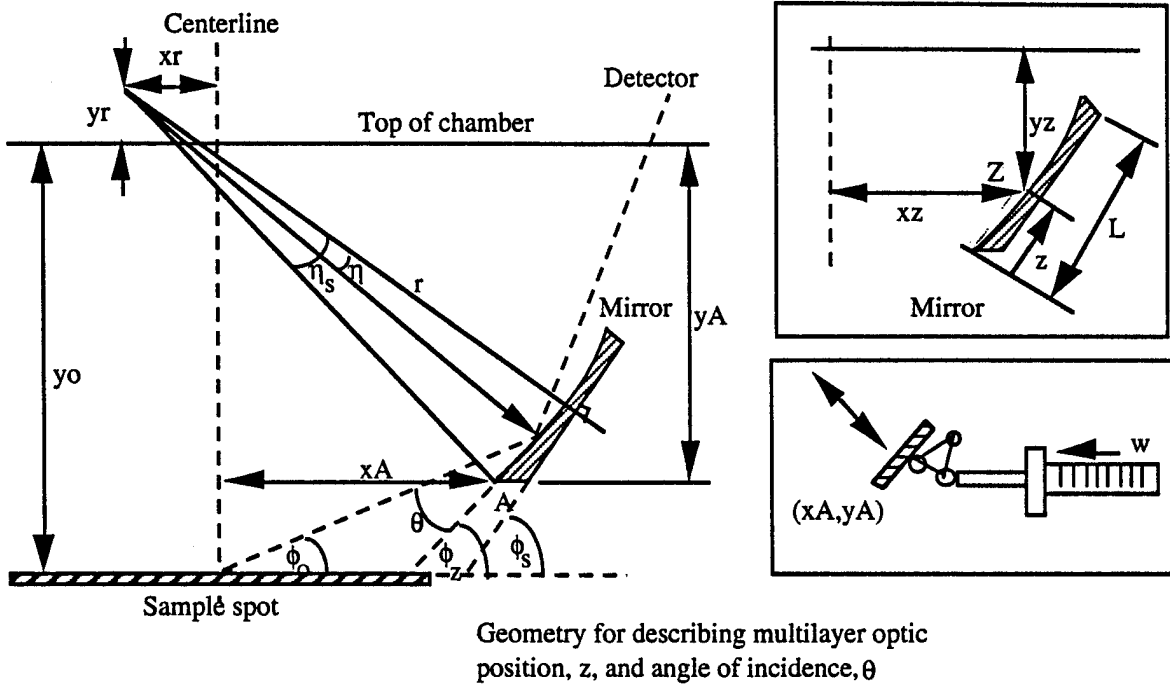


Figure 5.2.6. Parameters used to model angle of incidence along surface of multilayer.

A range of motion of ~ 1 cm for the mirror was sufficient to allow tuning over a range of energies sufficient to include the Ti-L and N-K lines. For a position, w_N , designated for reflection of N-K radiation, the angle of incidence as a function of distance along the multilayer, z, was used to calculate the refraction-corrected d-spacing of the multilayer, according to the Bragg relation, Equation 4.2.1. Figure 5.2.7 illustrates the results of the initial calculations used to derive a d-spacing gradient for the Monel/Ti multilayer. The nominal d-spacing of 34 \AA was required to vary by roughly $\pm 3\%$ over the 5 cm length of the optic.

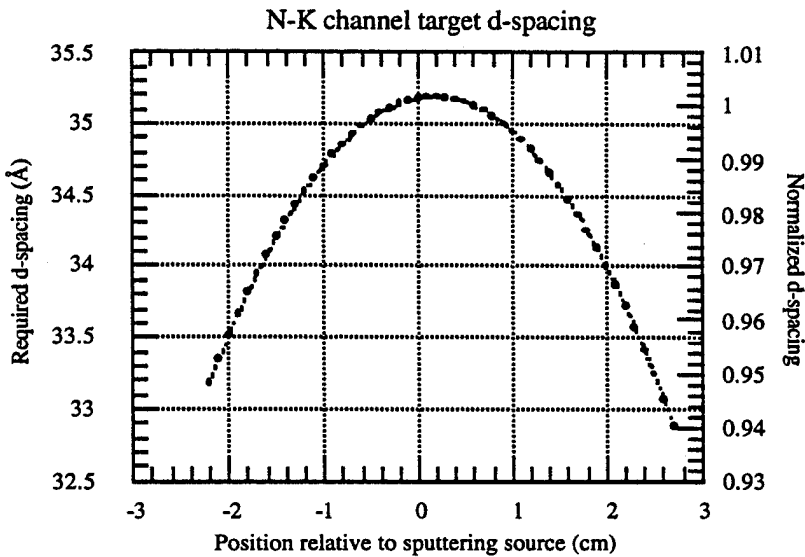


Figure 5.2.7. Required d-spacing gradient for Monel/Ti multilayer.

The d-spacing gradient was achieved by first sputtering Monel and Ti separately on glass plates and using optical density measurements to find the relative thickness of the deposition, as follows.

A simple two parameter model, which holds for sufficiently thick films (no interference between reflected beams) was used, which assumed that the transmittance of a film is given by,

$$T = (1-R) \cdot \exp\{-\alpha x\} \quad (5.2.1)$$

where R is reflectivity of the front surface, and α is an absorption coefficient for the sputtered film. If the optical density (OD) of a film is measured at two deposition rates, then,

$$OD_1 = -\log[T_1] = \log[1/(1-R)] + \alpha x_1 \cdot \log(e) \quad (5.2.2)$$

$$OD_2 = -\log[T_2] = \log[1/(1-R)] + \alpha x_2 \cdot \log(e) \quad (5.2.3)$$

where x_1 and x_2 are the two (unknown) deposition thicknesses. However, if the relative deposition rate, N , is known, then we also have,

$$x_2 = N \cdot x_1. \quad (5.2.4)$$

Subtracting Equation 5.2.2 from 5.2.3 eliminates the term depending on reflectivity, and solving for x_1 yields,

$$x_1 = [OD_2 - OD_1]/(N-1)\alpha \cdot \log(e). \quad (5.2.5)$$

Therefore, subtracting the optical densities from two different depositions removes the reflective term, and gives the relative thickness of either film. Figure 5.2.8 shows the resulting relative thickness of Monel and Ti films.

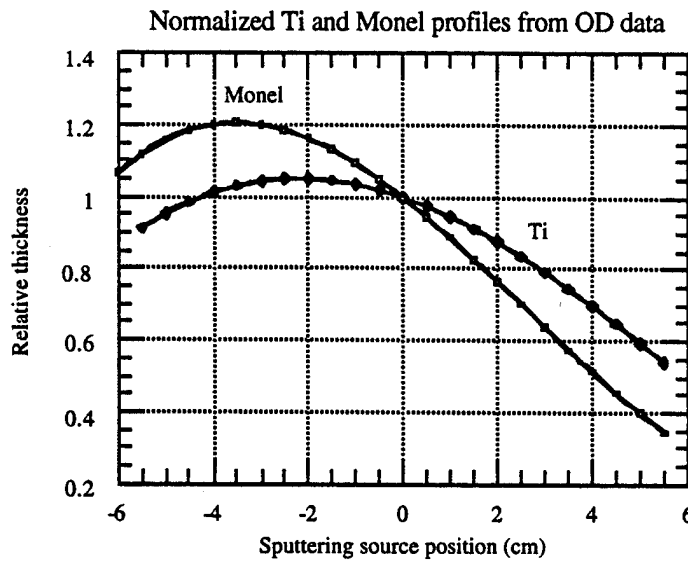


Figure 5.2.8. Sputtered profiles determined from optical density measurements.

These data were collected while the glass plates were rotating over the sputtering sources which results in a greater deposition towards the center of rotation (located at -25.4 cm). The absolute thickness of deposition was determined by measuring the diffraction pattern from a spot on the deposited film using Cu-K radiation. For example, Figure 5.2.9 shows the diffraction fringes

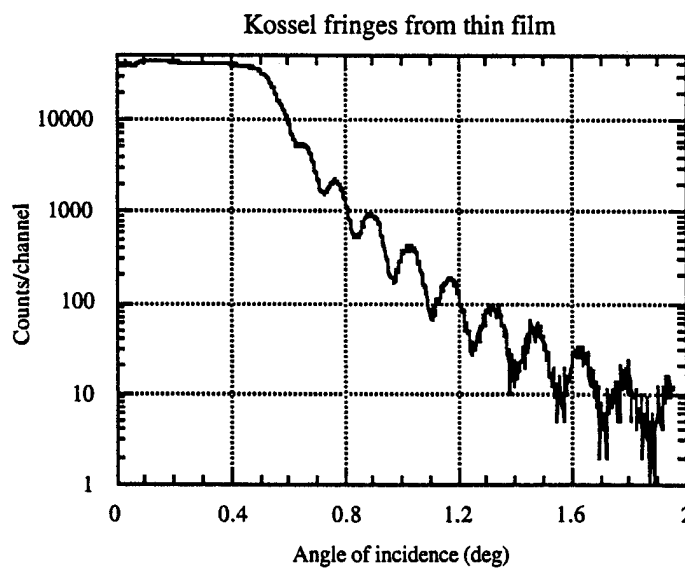


Figure 5.2.9. Diffraction pattern from thin W film used to determine film thickness.

produced by a thin film of W deposited on glass. The fringe spacings were modeled using a multilayer software code to determine the film thickness.

Several Excel spreadsheets were then used to design apertures which could be placed over the sputtering sources to modify the gradients of film thickness. After three iterations, the apertures were sufficiently accurate to produce films with the desired d-spacing gradient. At this point, a silicon wafer was substituted for the glass plates, and a multilayer structure was fabricated. The d-spacing was measured along the wafer using diffractometer scans and the techniques mentioned in Section 4.2.2, and the resulting gradient compared with the design.

The curve labeled 041595 in Figure 5.2.10 shows the first multilayer fabricated after developing the required gradient using optical density measurements. The absolute d-spacing was $\sim 3\text{\AA}$ too large, so further adjustments were achieved by changing the rate of rotation of the silicon substrate above the sputtering targets. The two succeeding depositions were able to match the required d-spacing gradient to within $\pm 0.1\text{\AA}$ of the target values.

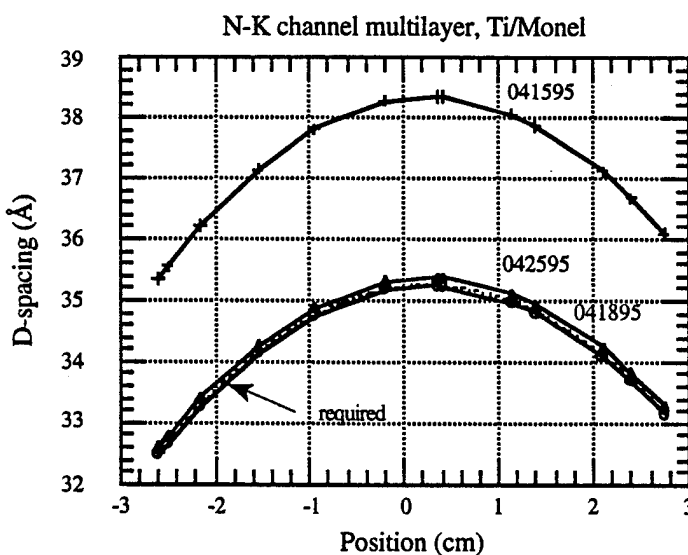


Figure 5.2.10. Convergence of d-spacing to desired value for Monel/Ti multilayer.

Deposition onto a silicon wafer was performed at the same time as the curved optic substrate to insure that the correct d-spacing value would be achieved. Previous measurements of the dependence of d-spacing on substrate curvature showed that for this application, the substrate curvature would not have a significant effect on the deposition.

Unfortunately, shortly after the multilayer was installed into the WDS instrument, it was found that the initial design had used a radius of curvature for the mirror substrate of 168 mm, which

differed significantly from the actual value of 235 mm. Therefore, the d-spacing gradient had to be redesigned, yielding the gradient shown in Figure 5.2.11.

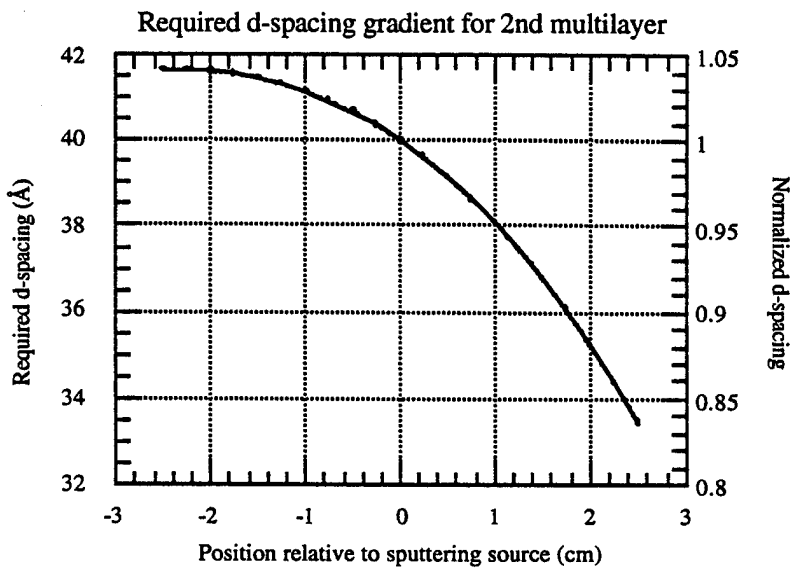


Figure 5.2.11. Redesign of multilayer d-spacing gradient.

This design had a nominal d-spacing of 37 Å, which was required to vary by roughly $\pm 8\%$ over the 5 cm length of the optic. At this point in time, the multilayer calibration studies had indicated a relatively low reflectivity at N-K for the Monel/Ti combination, which was attributed to a large roughness parameter, perhaps due to interdiffusion of the metal components. For this reason, a multilayer combination of W/Mg₂Si was chosen for the second fabrication effort, based upon previous experience with this combination where a smooth interface had been demonstrated. The process of developing the appropriate thin film gradients was started using W and Mg₂Si sputtering targets. However, after two depositions, the Mg₂Si target was found to have eroded through its 6 mm thickness at one location. Since a new target could not be purchased within the time frame of the project, the Ti target was reinstalled, and a W/Ti multilayer was fabricated instead.

The first multilayer deposition, labeled 102295 in Figure 5.2.12, was found to provide a satisfactory d-spacing gradient, but the absolute d-spacing was too large to be useful. Based on previous experience, the anticipated d-spacing was adjusted by resetting the sample rotation rate above the sputter targets by an appropriate factor. However, the resulting deposition on the optic substrate was found to be smaller than anticipated by 1.5 Å, when measurements were performed on the co-deposited silicon wafer substrate. This led to a predicted 26% decrease in throughput for the multilayer when mounted in the spectrometer.

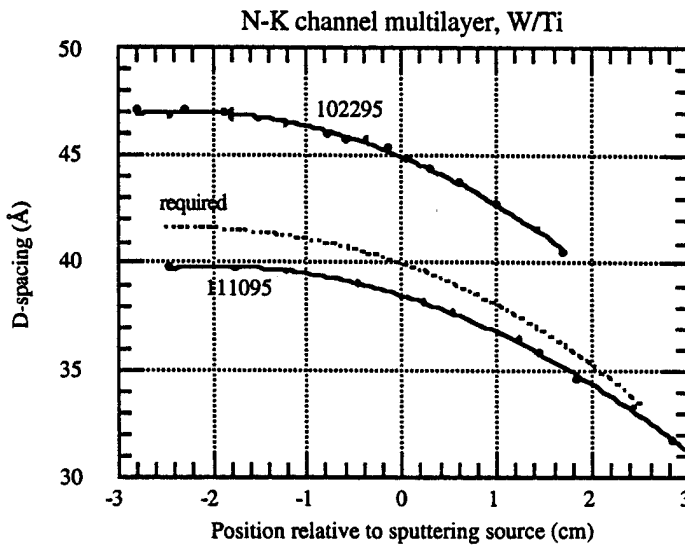


Figure 5.2.12. Convergence of d-spacing for W/Ti multilayer.

5.2.4 Optic Evaluation and System Integration

The WDS channel for N-K and Ti-L was aligned as follows. Initially, the lid to the chamber was removed and placed upside down on a bench to allow access to the internal adjustments.

The mirror substrate was mounted in a holder with two adjustable degrees of freedom, as shown in Figure 5.2.13. First, the holder had a spring-loaded screw which was used to adjust the tilt angle

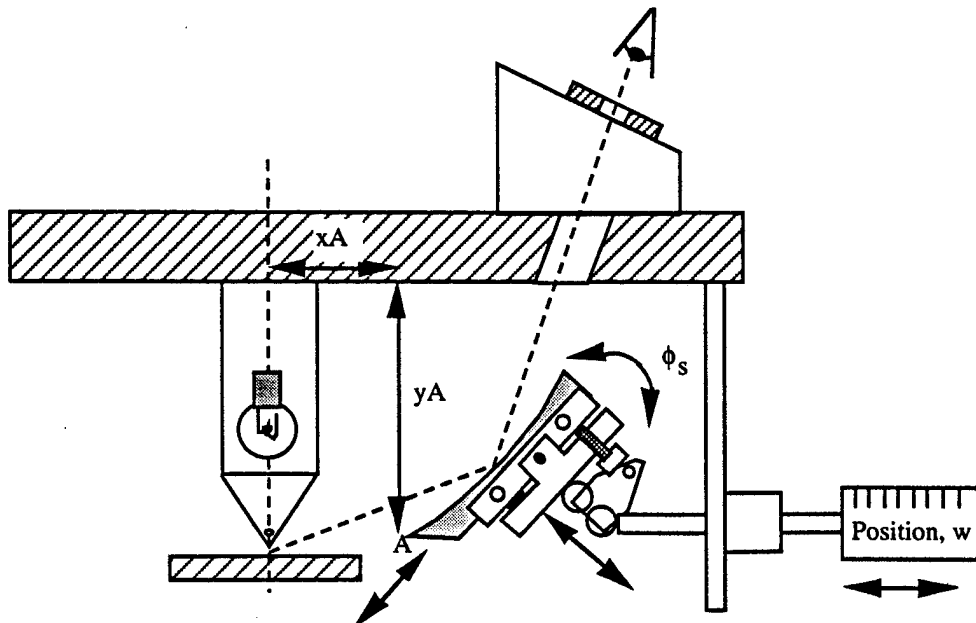


Figure 5.2.13. Schematic diagram showing adjustments used to align optic mirror.

of the optic, ϕ_s , to 45° with respect to the chamber lid. Next, two set screws were loosened to allow the mirror to slide within its holder. The mirror position was adjusted so that the distances x_A and y_A , measured from the leading edge of the mirror, A, corresponded to a point along the desired path of the mirror.

The lid was mounted back onto the chamber, and the x-ray tube was replaced with a collimated source of visible light which pointed straight down onto the sample. A black piece of paper with a small white spot was placed on the sample stage, and the stage was adjusted to place the spot beneath the visible light illumination. The detector was removed from the chamber lid and replaced by an identical proportional counter window, but without the boron hydride film or supporting grid. A final visual check was used to insure that visible light would be focused by the optic through the detector window as the position, w , was scanned from outside the chamber to cover the range of angles which would reflect N-K and Ti-L x-ray energies. Note that any small misalignments would result in a shift of the angle of incidence onto the multilayer away from the Bragg angle determined by the deposited d-spacing, but that the angle could be corrected by moving to a different position, w . For example, the estimated accuracy of $\pm 1^\circ$ for aligning the mirror angle, ϕ_s , could be corrected by shifting the mirror by an amount $\Delta w = \pm 1.2\text{mm}$.

The Monel/Ti multilayer was used to collect spectra before it was realized that the d-spacing gradient had been designed for a mirror of radius, 168 mm, instead of the actual mirror radius of 235 mm. Figure 5.2.14 shows the predicted reflectivity along the length of the fabricated

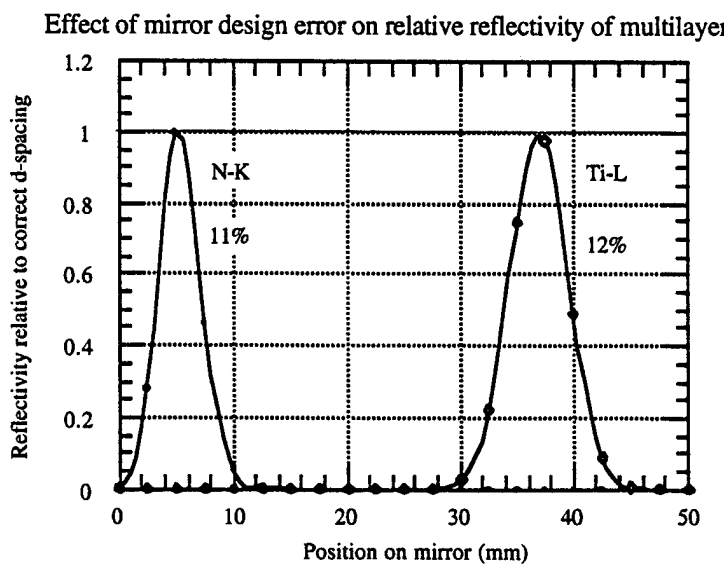


Figure 5.2.14. Predicted efficiency of Monel/Ti with incorrect d-spacing gradient.

multilayer relative to the correct design. Over a small part of the range of mirror motion, both N-K and Ti-L peaks are predicted to contribute to the detector signal. In effect, only a small portion (equivalent to a length of only 5.5 mm) of the total mirror length was effectively tuned to the N-K energy at any one mirror position, reducing throughput to 11% of the expected value for a correctly-designed multilayer.

The spectra shown in Figure 5.2.15 were collected for 1000 seconds with an excitation of 10kV and 1.0mA on the x-ray source, using either a silicon wafer or a 2.5- μ m-thick TiN sample on the stage. The TiN thickness was effectively “infinite” in the sense of producing the maximum possible N-K and Ti-L signals.

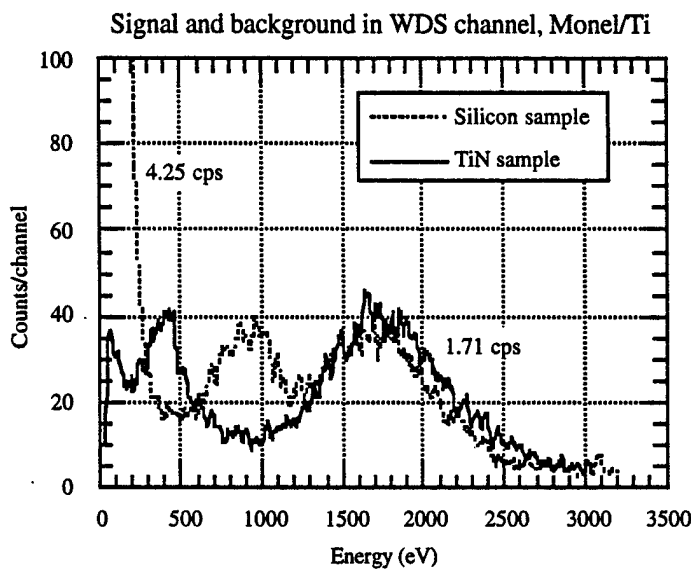


Figure 5.2.15. Spectra collected with Monel/Ti multilayer from silicon and TiN.

The spectrum from the silicon wafer displayed three peaks, at energies of ~100 eV, 900 eV, and 1600 eV, with a total count rate of 4.25 counts/s. The lowest energy peak, with the greatest observed count rate (1160 counts/channel at the peak), is attributed to Si-L radiation (91.5 eV) from the sample. The predicted reflectivity of Si-L from the top layer of Monel (a nickel/copper alloy) on the multilayer, at the 23° angle of incidence, is estimated at 6% [Henke, 1993], while the detector efficiency at this energy (see Figure 5.2.2) is about 30%. This peak would therefore be expected to be present in the proposed application for measuring thin TiN films on a silicon wafer. It could be preferentially suppressed by increasing the thickness of the aluminum coating on the counter window.

The peak at 900 eV was presumed to be from secondary fluorescence of the Monel in the multilayer by the incident Si-K radiation. The nickel/copper composition would give rise to peaks at 851 and 930 eV, which are not resolved by the detector. The third peak at 1600 eV is thought to

be Si-K scattered from the mirror and other chamber components. Note the absence of a significant Ti-L peak, which could result from secondary fluorescence of Ti in the multilayer by the incident Si-K radiation. This would be expected to be ~80 times lower than the Monel fluorescence peak, due to lower absorption of Si-K x rays and a lower fluorescence yield.

When the thick TiN sample was inserted into the chamber, the spectrum exhibited only two prominent peaks, at 400 eV and 1750 eV. The higher-energy peak was attributed to Si-K from the glass substrate for the multilayer, which is efficiently fluoresced by the Ti-K x rays. This hypothesis could have been further tested by collecting a spectrum at 5 kV excitation. However, the count rate was very low under this condition. The lower-energy peak at 400 eV was interpreted as a combination of N-K and Ti-L x rays reflected from the multilayer, since Ti-K from the sample would not be expected to contribute any significant fluorescence from Ti in the multilayer.

At this point, a comparison was made of the predicted and measured count rate due to the N-K and Ti-L reflected from the multilayer into the detector, as shown in Table 5.2.1. In section (1), the predicted fluorescence from the sample was taken from an Excel spreadsheet used to calculate fluorescence resulting from excitation by the Mo-L and continuum radiation emitted from the x-ray tube at a voltage of 5 kV. Then the various geometrical parameters, such as solid angle of radiation emitted from the x-ray tube and detector solid angle, as seen from the sample, were entered to yield a predicted net count rate for the Si(Li) detector. The value of 12.2 counts/s/watt for Ti-L and N-K was compared to the value deduced from an actual spectrum taken under those excitation conditions, Figure 5.2.16.

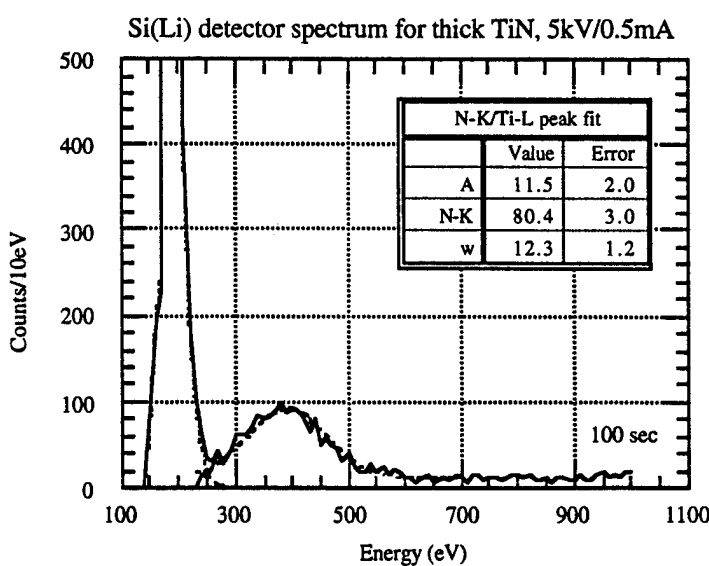


Figure 5.2.16. N-K and Ti-L emission from TiN sample measured with Si(Li) detector.

Table 5.2.1. WDS throughput calculations.

(1) Si(Li) detector count rates:

	N-K	Ti-La	Total	Units	Comment
Predicted (5kV)	1.98E+04	7.90E+03	2.77E+04	ph/s-sr^2-watt	Mo-L
	5.91E+03	2.37E+03	8.28E+03	ph/s-sr^2-watt	Continuum
X-ray tube	0.031	0.031	0.031	sr	
Detector solid angle	0.067	0.067	0.067	sr	
Detector efficiency	0.144	0.144	0.144	counts/ph	
Net	8.7	3.5	12.2	counts/s/watt	
Measured			7.1	counts/s/watt	
Estimated flux	435	174		ph/s-sr-watt	

(2) Proportional Counter count rates:

Mirror:				
angular range	0.311	0.311		radians
detector angle	0.125	0.125		radians
mirror fraction	0.5	1		
mirror solid angle	0.019	0.039		sr
Detector:				
grid fraction	0.79	0.79		
window absorption	0.46	0.46		
detector absorption	1	1		
combined efficiency	0.36	0.36		counts/ph
Reflectivity	0.04	0.04		
Expected: 5 kV	0.123	0.098		counts/s/watt
10 kV	0.468	0.374		
15 kV	0.709	0.567		
20 kV	0.910	0.727		
At 10kV/1.0mA	4.68	3.74	8.42	counts/sec

The measured count rate was 7.1 counts/s/watt, or about 58% of the predicted value, which appears to be consistent with the 5 kV data on Si-K and Al-K emission measured with the Amptek detector, Figure 5.1.8. The N-K peak could not be measured with the Si(Li) detector at 10 kV because of a low energy tail on the large Ti-K peak which obscured the small N-K peak.

Therefore it was assumed that the N-K emission at 10 kV would also be 58% of the predicted value.

Section (2) of the spreadsheet details the detector and multilayer mirror parameters required to determine the expected count rates using the WDS channel, resulting in predicted count rates of 4.7 and 3.7 counts/s for N-K and Ti-L, respectively. The measured count rate of 0.43 counts/s, for the peak shown in Figure 5.2.15, is about 9% of the predicted N-K count rate, which agrees well with the 11% efficiency of the multilayer due to the incorrect d-spacing distribution (Figure 5.2.14).

The W/Ti multilayer was also inserted into the chamber to test its performance. Figure 5.2.17 shows the predicted effect of the -1.5\AA d-spacing error (Figure 5.2.12) of the multilayer. The d-spacing offset was compensated by changing the mirror position by 1.3 mm, which should have yielded a predicted relative reflectivity of 74% compared with the ideal design.

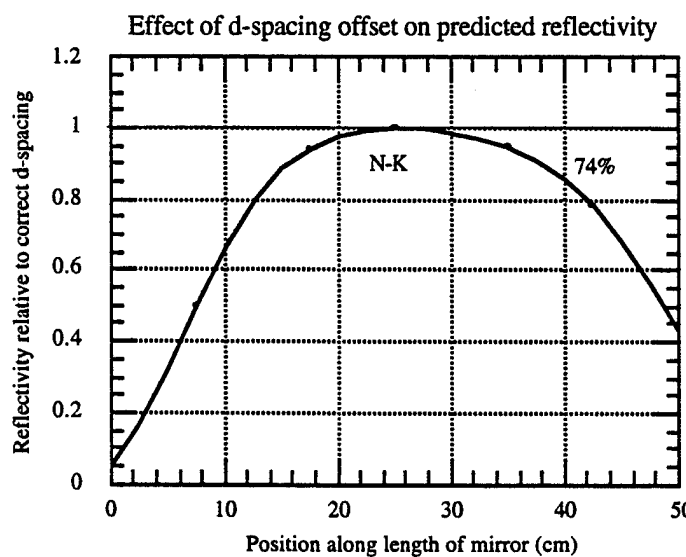


Figure 5.2.17. Predicted efficiency of W/Ti multilayer with d-spacing offset.

Two spectra were collected using the silicon and thick TiN samples, as shown in Figure 5.2.18. This time the silicon sample shows only the Si-L peak at 92 eV and the Si-K peak at 1740 eV, supporting the previous conclusion that the peak at 900 eV arose from fluorescence of Monel in the multilayer. The TiN sample now shows two peaks, corresponding to the N-K and Ti-L combination at 400 eV, and a broad peak at 2100 eV which includes both Si-K (1740 eV) and W-M fluorescence from the multilayer (2000 - 2400 eV).

An effort was made to find the multilayer position which optimized reflection for N-K and Ti-L. The estimated count rate with the W/Ti multilayer was expected to increase for N-K to ~2 counts/s, compared to 0.4 counts/s for the Monel/Ti multilayer, due to the improvement in d-spacing gradient. This may have been offset partially by a lower reflectivity for W/Ti at N-K, which was not directly evaluated.

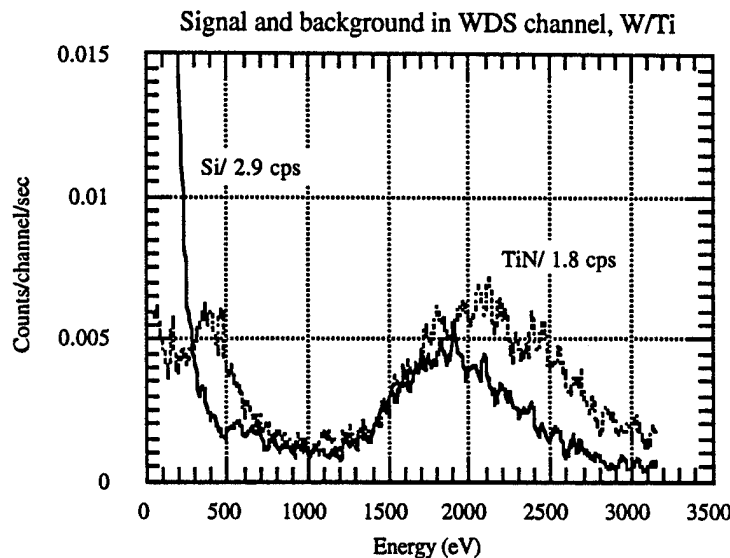


Figure 5.2.18. Spectra collected with W/Ti multilayer from silicon and TiN.

The multilayer position was scanned and the number of counts in the N-K/Ti-L region peak recorded as a function of position, as shown in Figure 5.2.19. The sample stage height was also varied over a 1mm range, to check the sensitivity to alignment. There was no significant deviation in the count rate from 0.4 counts/s, similar to the value observed with the Monel/Ti multilayer. The arrows represent the expected position for optimal reflection for a multilayer with the correct d-spacing. The absence of a clear peak was unexpected, and suggests that the system was not well aligned with the W/Ti multilayer. A better understanding of this result will require a more careful characterization of the W/Ti reflectivity at the energy of N-K x rays, as well as more effort devoted to insuring alignment of the multilayer mirror with sample and detector.

5.3 ENERGY-DISPERSIVE SPECTROMETER

5.3.1 Purchased Components

As outlined in Sections 3.3.3 and 4.3, it was decided that we would purchase a Si(Li) detector from GDE, Rocky Hill, NJ, to the specifications outlined in Table 4.3.1 (Section 4.3.2). This detector was supplied complete with a custom pre-amp and cables for a Canberra (Meriden, CT) amplifier. We purchased a Canberra Model 2024 amplifier, with Gaussian filter shaping and

switched shaping time constants from 0.25 to 8 microseconds. This is a research-grade amplifier, with high count-rate capabilities. It also has a Gated Integrator mode for even higher count rate applications. Matched with this, a Canberra Model 8715 ADC was purchased, which has a fixed conversion time of 800 nanoseconds. Both these units were purchased to allow high-count-rate studies to be performed. The 8 microsecond time constant was not optimal for getting the best resolution, so we obtained on loan a special Model 2026S Canberra amplifier, with a 24-microsecond time constant, for some resolution and low-energy tests.

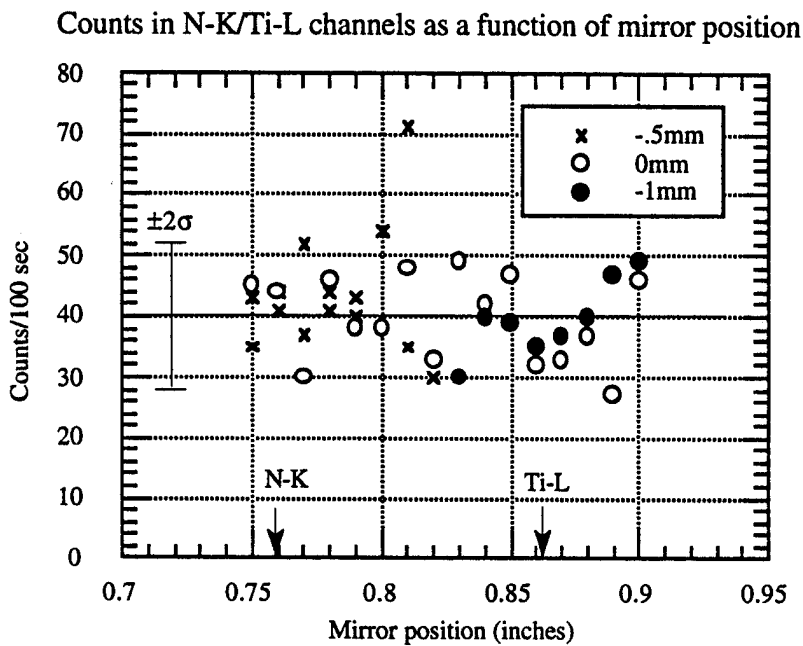


Figure 5.2.19. Combined N-K and Ti-L signal as a function of mirror position.

The electronics were mounted into a NIM-bin cabinet supplied by IXRF (Houston, TX), which also provides the high-voltage bias supply for the detector. We also purchased an IXRF multi-channel analyzer interface card to install into an Intel PC, and software for acquiring and processing spectra. We purchased an Intel Pentium-100-class computer from Gateway 2000 (N. Sioux City, ND), as the main data acquisition, display and processing unit.

5.3.2 System Integration

Because the detector is sensitive to light, it was mounted into the chamber prior to preliminary testing. No problems were encountered in mounting the detector. The detector slide mechanism worked, although a small amount of precessing was noticed as the detector was moved in and out. It was possible to bring the detector close to the x-ray source, as designed. Qualitatively, the alignment between the detector and tube looked good, after the tube was brought to the correct position. The exact alignment and actual angles need to be carefully measured and calculated with

a true engineering drawing. The main issue to be resolved will be the improvement of the solid angle of the detector. However, at this time, the issues are understood and not in the critical path.

We had been concerned about possible vibration effects, which can seriously degrade the Si(Li) detector resolution, but tests with the vacuum pump off and on had no effect on the measured resolution. The high-voltage supply and x-ray tube were expected to contribute to the noise in the system. However, there were no serious effects encountered (i.e., the resolution did not degrade with kV or mA, other than through count-rate effects). It also appears that no visible or infrared light is seen by the Si(Li) detector. In systems without a beryllium window, this can be serious problem, but, as expected, the beryllium window on the tube together with other factors (such as geometry and the coatings on the detector and tube windows) was sufficient to suppress this source of light, and also any electrons.

The setup of the Canberra electronics took some time because of the range of options available in the amplifier and, to a lesser extent, the ADC. Also there was some confusion in the manual on some of the switch settings. The settings were finally resolved, and good-quality spectra obtained at a variety of time constants. The important settings on the Canberra 2024 amplifier were as follows: the internal J6 jumper was set to DT (opposite to BSY); the Pile-Up Rejector (PUR) was set to ON; the amplifier mode set to UNIpolar (vs. GI); the input polarity to +; the restorer threshold set to AUTO; the Coarse Gain was set to 100°, and the Fine Gain to 0.387. The Canberra 8715 ADC was set with both the Gain and Range at 4K channels (no zero offset), the Peak Detect set to AUTO, and the Input mode set to PHA. Both the amplifier Pole/Zero and PUR, and the ADC Zero and Lower-Level Discriminator (LLD), were set as per the respective instruction manuals. The Canberra 2026S amplifier was also tested in place of the 2024. This had fewer front panel adjustments, and was very easy to install and set up. This had a specially installed 24 microsecond-shaping-time constant, for optimal peak resolution (at the expense of throughput).

The amplifier time constant was set to 8 microseconds for most measurements, except for some studies of throughput against time constant. It should be noted that these time-constant numbers are somewhat arbitrary, as the peaking time is about twice the front-panel value, and the overall peak-processing time is about four times that value. In fact, the IEEE has proposed an alternative term, "shaping index," to describe the complete time to process the peak, which would be independent of individual manufacturer's algorithms for their specifications.

Whenever the time constant was changed, it was necessary to re-adjust the LLD on the ADC to adjust the noise threshold. The detector pre-amplifier came with a cable for the Inhibit signal, which inhibits pulse processing during the Pulsed-Optical Reset (POR) event. A cable was added to the IXRF rear panel to provide this input to the rear of the amplifier. Another internal cable and BNC connector was provided to bring out the Incoming Count Rate (ICR) signal, which we then

connected to an Ortec NIM-bin ratemeter. The latter provided an analog signal which gave rapid response to changing of the tube controls or sample position. It was verified that this value corresponded to the acquired count rate, showing that the livetime clock and handshaking between the pre-amp, amplifier, ADC and the PC-MCA interface card was functioning correctly.

Software from IXRF was installed in the Pentium computer without any compatibility issues. This software enabled spectra to be acquired, saved and processed in a variety of ways.

5.3.3 EDS Detector/Electronics Evaluation

Only very weak radioisotope sources were available, so the resolution measurements on the Si(Li) detector were performed using the x-ray tube to fluoresce elemental standards. As we did not have a manganese standard (most detectors are specified with Fe-55 at the energy of Mn-K α , i.e., at 5.9 keV), we used samples of titanium and nickel, and interpolated to get a value of the FWHM resolution at 5.9 keV. The respective resolutions for nickel and titanium were 170 and 155 eV for the 8-microsecond time constant. This gave an interpolated value of about 162 eV at 5.9 keV.

Using the 2026S amplifier, and a 24-microsecond time constant, an improvement of about 5 eV in resolution was obtained, resulting in an estimated FWHM of about 157 eV at 5.9 keV. This is close to the specification of 150 eV, considering that a tube is being used to generate the spectrum, rather than an isotope. Using a tube has the effect of increasing the total system noise, which increases the peak FWHM. Also using the 2026S amplifier (at 24 microseconds), it was possible to see a well-separated peak of carbon, from a pure graphite sample, as the overall low-energy noise was reduced. By contrast, with a 8-microsecond time constant (Model 2024), the carbon peak was not completely separated from the low-energy noise peak.

It would not have been impossible to see boron with the latter arrangement, but with the 2026S amplifier it should have been possible. A pure boron nitride sample was analyzed, with the hope of seeing a boron peak, but it was not observed. This was, presumably, because the very low efficiency of excitation for the molybdenum transmission-target tube, the low fluorescence yield of boron, and the low transmission of boron x rays through the window and front layers of the detector (see Figure 4.3.3).

Overall the detector performed as expected, and enabled measurements of low-energy fluorescence for thin-films of interest, such as TiN, by measuring the peaks of Ti-L and N-K x rays, as well as the more conventional x-ray energies up to 20 keV, such as Ti K x rays. In terms of solid angle, the window grid presents a major source of hindrance in achieving the desired target value (0.10 steradians). MOXTEK is currently testing a version of their boron hydride windows (the same material that we used for the proportional counter) for mounting on the end caps of Si(Li)

detectors. This window does not require a grid (i.e., is self supporting), which would raise the usable area of the detector from 75 to 100%.

The vendor (GDE) also believes that the remaining 25% of the solid angle could be gained from modifying the end-cap design, and ensuring the maximum take-off angle (this needs to be done in concert with the tube geometry).

We also evaluated the silicon pin-diode detector, with an Fe-55 radioisotope source, which gave a FWHM resolution at 5.9 keV of about 275 eV (Figure 5.3.1), using the Amptek electronics (power supply, pre-amplifier and amplifier). This was somewhat higher than the quoted specification of 250 eV, and could probably be improved by using a better pulse processing system, with a longer shaping time. We experimented by mounting the detector on a metal plate, and cooling this with liquid nitrogen, which resulted in a measured temperature (with the built-in temperature monitor) of about -90°C. This did not appreciably affect the measured peak resolution.

5.4 SYSTEM INTEGRATION

5.4.1 Integration Issues

The stepwise integration of vacuum system, stage motion, x-ray tube, Si(Li) detector, and WDS spectrometer proceeded fairly smoothly with only a few modifications required on the finished assemblies. For example the x-ray tube turned out to have a cone angle of 78° rather than the 70° portrayed in an early design sketch, which was used to design the tube mounting fixture. As a result, when the x-ray tube was mounted on the chamber, the collimator was 2.7 mm higher than expected above the sample stage, leading to an increase in the projected spot size. Similarly, the Viton o-ring used to seal the chamber lid could not be fully compressed when the lid was bolted down, which increased the tube height an additional 0.3 mm. The sample stage could not compensate for the additional tube height, because it was limited by the lower side of the Si(Li) detector. These issues were resolved by re-machining the tube holder to lower the tube by ~3.0 mm.

Early testing of the x-ray tube up to voltages of 30 kV revealed insignificant increases in the radiation level above background behind the x-ray tube. In addition, although the operating temperature varied systematically between x-ray tubes, the maximum value recorded on any tube was only 36° C, after several hours of operation at 10 watts. The tubes were therefore run without any additional cooling equipment.

The high-voltage power supply was found to operate in a stable manner, but the in-line connectors used to switch the supply to different x-ray tubes were found to be unreliable, due to cold solder

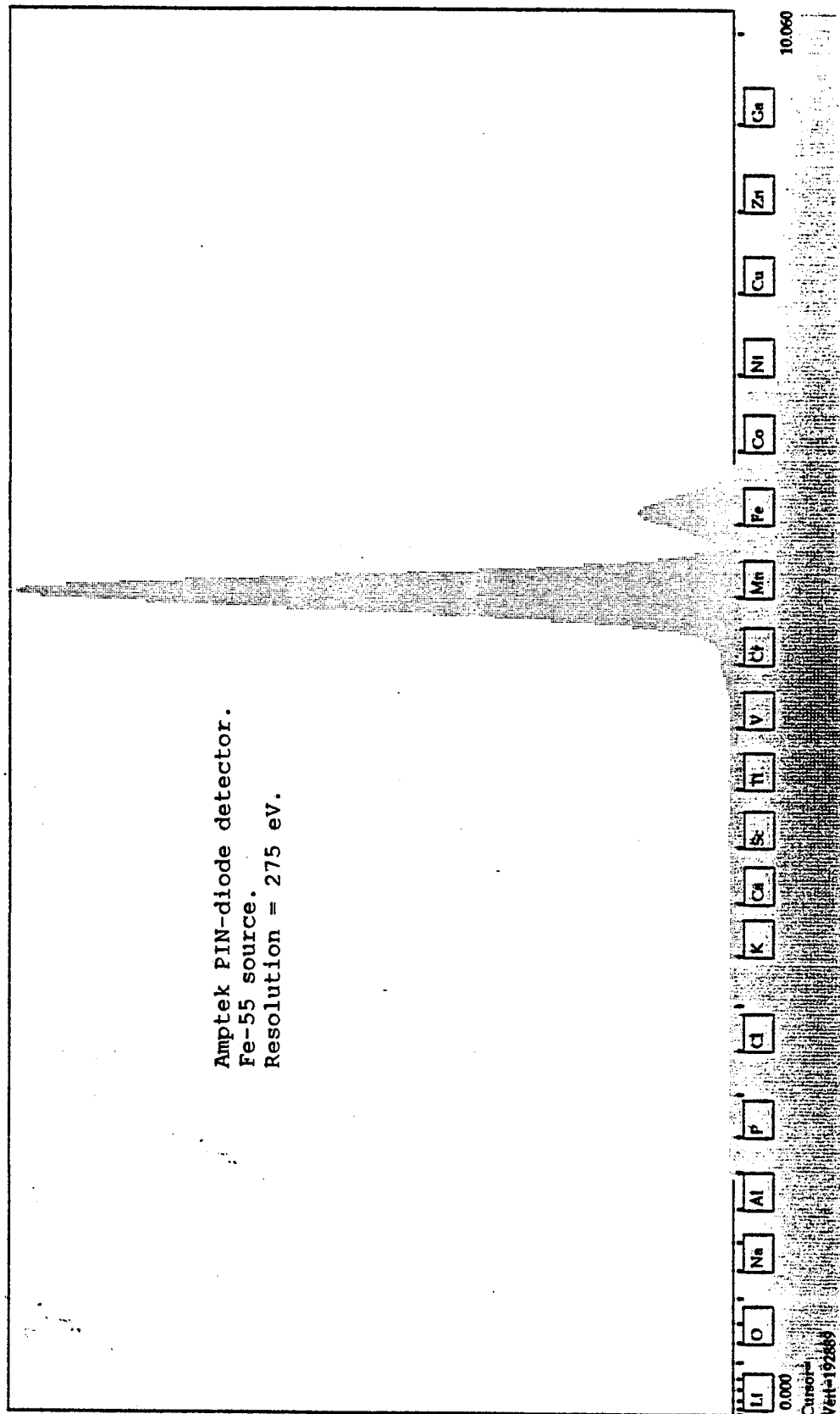


Figure 5.3.1. Fe-55 spectrum for Amptek XR-100T PIN-diode detector.

connections which repeatedly broke. A better method for maintaining a solid connection between the cables and connectors remains to be established.

The Si(Li) detector was found to conform well to the designed close-coupling geometry between source, sample, and detector. The detector could be advanced until it touched the x-ray source, and was then pulled back slightly to provide thermal insulation from the tube. The optimal positioning of the Si(Li) detector and sample stage for collecting sample fluorescence were mapped out, as shown in Figure 5.4.1. The detector position could be monitored with a scale reading external to the vacuum chamber. With the detector positioned as close to the x-ray tube as possible, the count rate was maximum at a stage height of -1.2 mm. Apparently, with the stage higher, the detector collimator began to obscure the line of sight between detector and the far side of the sample spot. As the detector was retracted, the count rate decreases steadily, as the collimator on the detector started to block the line of sight to the whole sample spot.

Note that the count rate was relatively insensitive to stage height over a range of ± 0.5 mm about the maximum. This was encouraging, because it meant that precise vertical positioning of the sample would not necessarily be required for precise x-ray measurements. A change of 0.25 mm near the peak maximum would result in a count rate change of only 0.25%, which is about the level expected for 1σ precision, from counting statistics. Figure 5.4.2 shows an expanded view of the count rate variation around the maximum value.

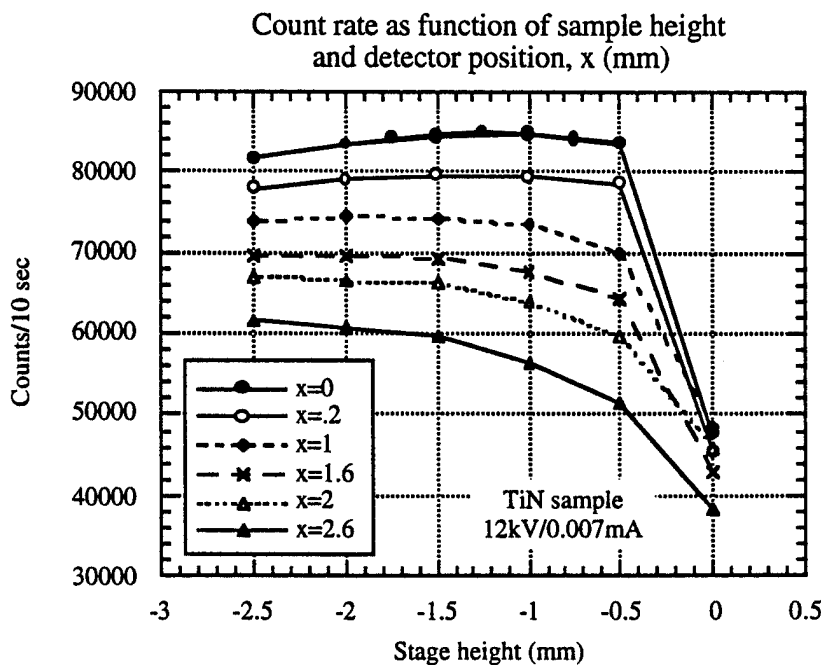


Figure 5.4.1. Variation in signal with stage height and detector position.

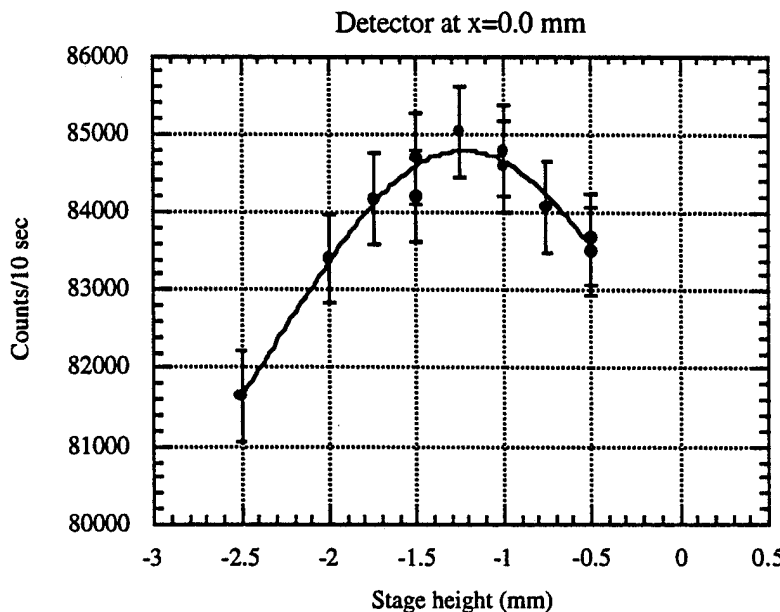


Figure 5.4.2. Variation in signal near stage maximum.

The stepper motor appeared to work well in the vacuum environment and was used to scan samples beneath the source to provide an indication of sample spot size. With the chamber door closed it was not possible to gauge the distance between sample and source, so a scale was calibrated on the rotary feedthrough to provide an indication of sample height. This was calibrated by placing samples of known thickness on the stage, and raising them until they contacted the collimator on the x-ray tube. With this calibration, a wire could be scanned beneath the source, yielding the fluorescence curves shown in Figure 5.4.3.

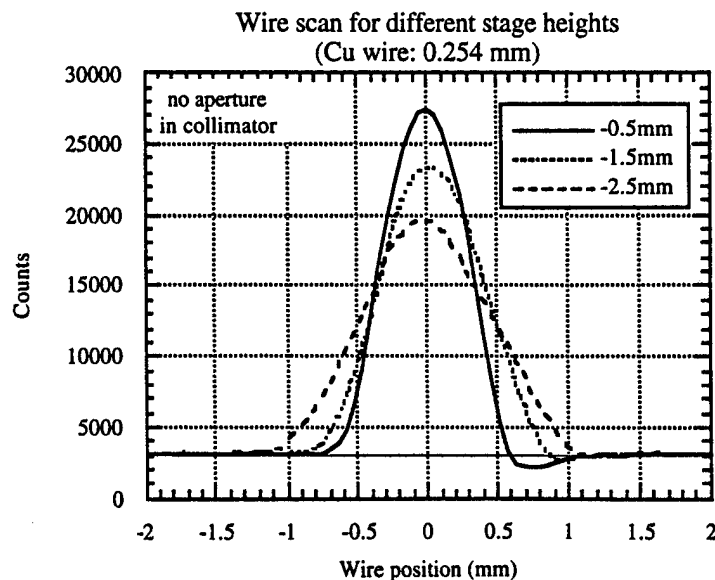


Figure 5.4.3. Scans of copper wire at three different stage heights.

After correcting for the wire diameter, the peak widths could be used to infer spot size as a function of stage height. Figure 5.4.4 illustrates the derived spot size for the collimator with no aperture inserted. The open diameter of the collimator was 1 mm, which agrees with the extrapolation of spot size to a sample height of 0 mm below the collimator.

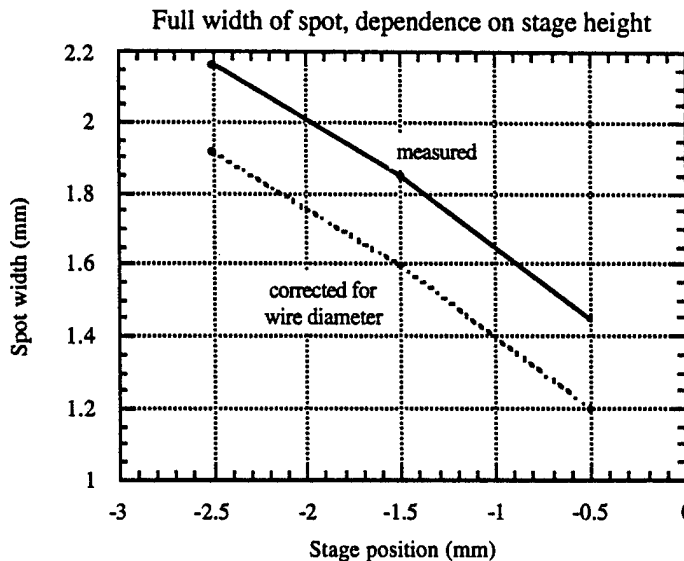


Figure 5.4.4. Extrapolation of sample spot size as a function of stage position.

5.4.2 System Performance

The performance of the x-ray tube was first evaluated with respect to the achievable spot size on the sample. The pinhole photographs (Figure 5.1.14) indicated a minimum focal spot size of $0.5 \times 0.9 \text{ mm}^2$, which was larger than the desired 0.15 mm design. Before the photos were made, the achievable spot size on the sample was estimated by scanning a thin wire through the focal spot, as shown in Figure 5.4.5, for two different sample heights.

The spot widths were corrected for the contribution of the wire diameter, and plotted as a function of collimator-sample distance, as shown in Figure 5.4.6. Also plotted were the predicted sample spot sizes for 1, 2, and 3 mm focal spot sizes and the $100 \mu\text{m}$ aperture used in the collimator. It can be seen that x-ray tube #1 was well fit by a focal spot size of just over 2 mm, which is in reasonable agreement with the 2.5 mm spot size shown in Figure 5.1.14.

One of the original goals was to produce a spot size of $100 \mu\text{m}$ using a $37.5 \mu\text{m}$ aperture in conjunction with a source with a $150\text{-}\mu\text{m}$ -focal spot. The smallest focal-spot size of 0.9 mm was achieved with tube #2 which, at the optimal working distance of 1.3 mm from the collimator (Figure 5.4.2), would produce a spot size on the sample of $267 \mu\text{m}$.

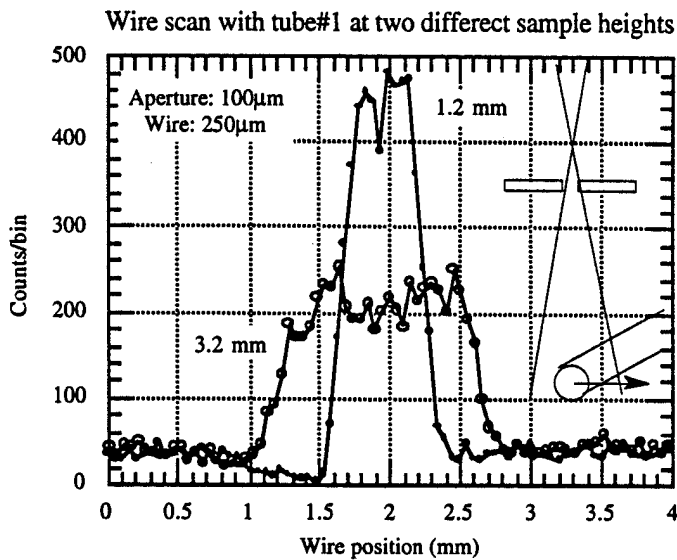


Figure 5.4.5. Dependence of sample spot size on sample-collimator separation.

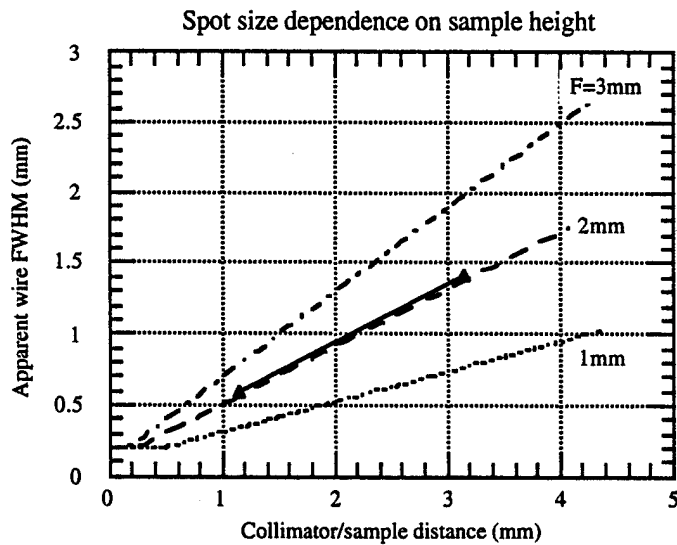


Figure 5.4.6. Estimate of focal spot diameter derived from measured spot diameters.

The EDS Si(Li) detector performance was evaluated by collecting spectra from various low Z element samples in order to determine energy resolution and noise floor. Figure 5.4.7 shows the spectrum collected (using the 8-microsecond time constant) from samples of carbon and boron, compared to the noise spectrum of the detector.

The noise floor at ~200 eV was typical for the optimized detector settings which were routinely used to collect spectra (Section 5.3.2). The carbon sample generated a well defined peak near the expected energy of 277 eV with an integrated count rate of 8.3 counts/s/watt, after removing the

detector noise component and summing counts up to 400 eV. It was not possible to discern a B-K peak at 183 eV in the presence of detector noise.

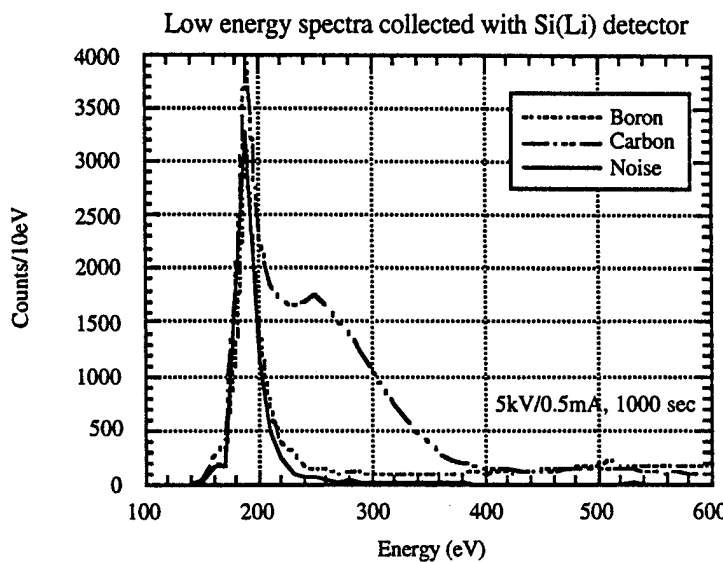


Figure 5.4.7. Spectra of boron and carbon samples collected with the Si(Li) detector.

The spectrum from a silicon wafer was also collected, as shown in Figure 5.4.8. The integrated count rate was measured to be 9,120 counts/s/watt. The carbon and silicon spectra were also used to gauge the overall system efficiency, including both the tube flux and the detector. The geometry used for the data collection, Figure 5.4.9, was used to determine the solid angle of flux hitting the sample and the collection solid angle for the detector.

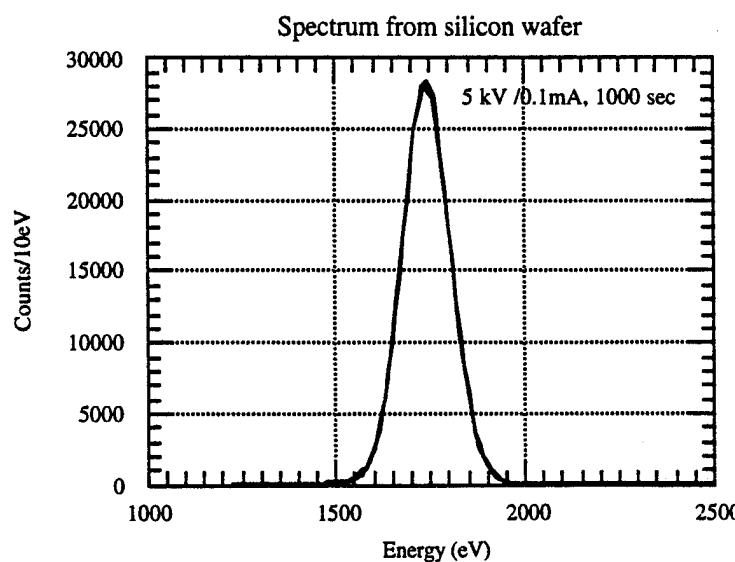


Figure 5.4.8. Spectrum from silicon wafer fit by a gaussian curve.

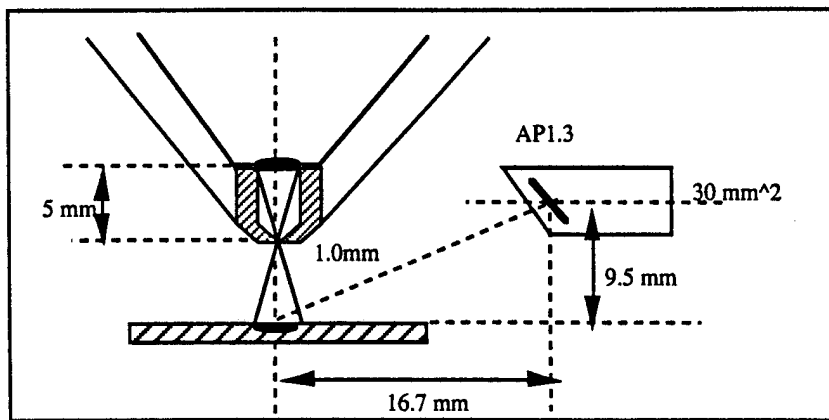


Figure 5.4.9. Geometry used to predict count rates for C-K and Si-K fluorescence.

The take-off angle and x-ray tube operating conditions were substituted into an Excel spreadsheet for predicting the x-ray tube spectrum. The detector efficiency was estimated using the spreadsheet illustrated below (ignoring the window absorption) in Table 5.4.1. Note the large effect of the silicon deadlayer (the inactive layer on the front side of the detector crystal). The Si(Li) detector efficiency for carbon is only ~10% compared to ~92% for the silicon radiation. The extremely low detection efficiency for B-K, ~1%, explains the inability to see any evidence for a boron peak in Figure 5.4.7.

Table 5.4.1. Si(Li) detector efficiency based on Si deadlayer and Au contact absorption.

Energy	Line	Contact $\mu(\text{Au})$ (cm $^2/\text{g}$)	Au contact trans.	Si deadlayer $\mu(\text{Si})$ (cm $^2/\text{g}$)	Si deadlayer trans.	Net detector efficiency	
0.0915	Si-L	33400	0.284	7640	0.702	0.199	
0.183	B-K	10400	0.676	84000	0.020	0.014	
0.277	C-K	15200	0.564	36800	0.181	0.102	
0.392	N-K	15400	0.560	16500	0.465	0.260	
0.452	Ti-L	13700	0.597	11800	0.578	0.345	
1.486	Al-K	2310	0.917	543	0.975	0.894	
1.740	Si-K	1660	0.939	350	0.984	0.924	
1.780	W-M	1400	0.949	330	0.985	0.934	
4.510	Ti-K	930	0.966	318	0.985	0.951	
8.400	W-L	190	0.993	54	0.997	0.990	
Si density		2.32	g/cm 3	Si deadlayer		2.0E-05	cm
Au density		18.85	g/cm 3	Au thickness		2.0E-06	cm

All the relevant information (including solid angles, detector efficiencies and window absorption) was then substituted into another spreadsheet for comparing the predicted and measured count rates of carbon and silicon at 5 kV excitation (Tables 5.4.2 and 5.4.3 show the results of these calculations). The same values for the silicon dead and gold contact layers were used, with a grid factor of 0.75 and tabulated absorption values for the MOXTEK AP1.3 window. The calculated values for the overall detector efficiency (including the window etc.) were 0.676 for Si-K x rays, and 0.046 for C-K x rays. These values are the same as those shown in a previous plot in Figure 4.3.3.

The geometry of Figure 5.4.9 was used to calculate the solid angles for both the source and the detector. The calculated solid angle for the source was 0.0314 steradians, and for the detector was 0.0666 steradians (assuming an active area of 30 mm² and a take-off angle of 30°). The latter does not include the grid factor for the window, and agrees well with the value supplied by the detector vendor (GDE). The tube anode was assumed to consist of 1.5 microns of molybdenum on 125 microns of beryllium.

Table 5.4.2. Count rates from silicon.

Voltage	Mo Continuum	Mo Characteristic	Charact./ Continuum	Predicted count rate	Measured count rate	Ratio
(kV)	(ph/sec-ster ² - watt)	(ph/sec-ster ² - watt)	Ratio	Net c/s/watt	c/s/watt	
5	2.48E+06	7.79E+06	3.1	1.45E+04	9120	0.63
10	9.28E+06	2.54E+07	2.7	4.90E+04		
15	1.37E+07	3.72E+07	2.7	7.19E+04		
20	1.70E+07	4.71E+07	2.8	9.06E+04		

Table 5.4.3. Count rates from carbon.

Voltage	Mo Continuum	Mo Characteristic	Charact./ Continuum	Predicted count rate	Measured count rate	Ratio
(kV)	(ph/sec-ster ² - watt)	(ph/sec-ster ² - watt)	Ratio	Net c/s/watt	c/s/watt	
5	7.66E+03	2.58E+04	3.4	3.2	9.88	3.07
10	1.58E+04	8.42E+04	5.3	9.6		
15	2.02E+04	1.23E+05	6.1	13.8		
20	2.44E+04	1.56E+05	6.4	17.3		

The predicted count rates for Si-K and C-K for the given geometry and excitation conditions were 1.45×10^4 and 3.2 counts/s/watt, respectively. The measured values were 63% and 307% of the predicted values, for silicon and carbon, respectively. The predicted value for carbon is much lower than the measured value, which could be explained by a silicon deadlayer which is actually thinner than the assumed value of 0.2 μm . For example, a deadlayer which was a third of the assumed value, would be ~ 3.1 more transmissive for carbon x rays. Other sources of this discrepancy could be in the model used for low-energy excitation, which was not originally designed for very low-energy excitation. Also, the molybdenum anode thickness is probably less than the value used for modeling.

The ED spectrometer was also used to determine the Ti and N signal levels from a thick TiN film. The Si(Li) detector does not have the spectral resolution required to distinguish Ti-L from N-K and thus the measured signal is a combination of these two emissions. Table 5.4.4 summarizes the results from Table 5.2.1 and compares the predicted and measured signal levels at 5 kV. Note that the N-source term for a thin TiN film is comparable to that produced by the thick TiN film at 5 kV. At higher accelerating potentials, the Ti and N signals were masked by a large low-energy background.

Table 5.4.4. Combined T-L and N-K count rates from thick TiN sample.

Voltage	Mo Continuum	Mo Characteristic	Charact./Continuum	Predicted count rate	Measured count rate	Ratio
(kV)	(ph/sec-ster 2 -watt)	(ph/sec-ster 2 -watt)	Ratio	Net c/s/watt	c/s/watt	
5	8.28E+03	2.77E+04	3.3	12.2	7.1	0.58

The performance of the WDS channel was evaluated by trying to measure the N-K/Ti-L signals generated by the thick TiN sample. The predicted signal levels for nitrogen, with most parameters now known, are shown in Table 5.4.5 (again taken from Table 5.2.1), for a thick TiN film and a ~ 1.5 -mm-diameter analysis area.

Table 5.4.5. N-K count rates from thick TiN sample.

Voltage	N-Source	Source Solid Angle	Optic Solid Angle	Predicted count rate	Measured count rate	Ratio
(kV)	(ph/sec-ster 2 -watt)	(steradians)	(steradians)	Net c/s/watt	Net c/s/watt	
5	2.57E+04	0.0314	7.6E-04	0.12		
10	9.78E+04	0.0314	7.6E-04	0.47	0.043	0.09
20	1.9E+05	0.0314	7.6E-04	0.91		

The performance of the WDS channel was found to be degraded by a large background signal when the x-ray tube was operated at 20 kV. This was interpreted to be a result of high energy scatter into the proportional counter, with subsequent electron emission from the detector walls which created a low energy tail of pulses. This problem was avoided by making measurements at 10 kV, where the expected N-K signal was estimated to be 0.47 c/s/watt (see Table 5.4.5). The measured N-K signal was only 9 percent of the predicted signal.

The low N-K signal was initially attributed to a mismatch between the d-spacing and the substrate geometry. We estimated that this mismatch could reduce the solid angle of the optic by as much as an order of magnitude. To investigate this hypothesis, we fabricated a second optic by coating the substrate with a W/Ti multilayer and the correct d-spacing distribution. This material combination was selected to improve the reflectivity of the coating. When the measurements were repeated using this new optic, we found that the N-K count rate was essentially unchanged. At present, we do not have an understanding of the reasons for this observation. Possibilities include a misadjusted mirror angle or a decreased reflectivity at N-K. In any event, further work must be done to clarify the reason(s) for low count rates and the absence of well-defined reflection peaks.

6.0 RESULTS AND DISCUSSION

6.1 SYSTEM EVALUATION

6.1.1 Performance vs. Requirements

In this project, we made substantial progress in the development of advanced x-ray analytical instrumentation in several areas. New tube and spectrometer technologies have been developed which show considerable promise for the analysis of semiconductor thin films. However, this development program could not be completed under this contract because of the cut made in funding.

Although we have made substantial progress, the system performance did not meet the planned requirements in two respects. First, the achieved x-ray tube focal spot size of just under 1 mm was about six times larger than the design goal of 0.15 mm. This impacts the previously defined figure of merit (Section 4.1.2),

$$F = [P d_s^2 / 4L_{0s}^2] [1 - (d_0 / d_s) (L_{1s}/L_{01})]^2 \quad (6.1.1)$$

which is proportional to the flux that can be deposited onto a sample spot of diameter, d_s , for a given power loading, P . The actual value of F achieved was 0.00013 with a power loading of 10 watts and a sample spot diameter of 0.27 mm. If we re-evaluate the commercial instrument (the Omicron) for the same sample spot diameter of 0.27 mm, the figure of merit increases to 0.00025, which is two times better than what was achieved in this project, at this spot size.

The instrument, at the present performance level, still fills a useful niche for larger spot sizes, as shown in Figure 6.1.1. The plot shows the calculated figure of merit as a function of sample spot size for the instrument as designed, for a commercially available instrument, and as achieved with the prototype. A third curve shows the expected small spot performance with the new collimator, which has not yet been demonstrated.

For spot sizes above 0.3 mm, the prototype instrument provides increased flux onto the sample spot, with a factor of 10 improvement for spot sizes close to 1 mm. Future work should be aimed at reducing the spot size on the anode, and in optimizing the geometry of the collimator assembly.

The second requirement, for a high efficiency WDS channel designed to discriminate N-K and Ti-L fluorescence from thin film samples, was also not demonstrated. Section 1.3.1 demonstrated that the key to making a precise WDS measurement of the TiN thickness was the development of a high efficiency x-ray collection optic. Our original objective for this project was to achieve a 1 Å precision (1σ) for the measurement of a 400 Å TiN films, by measuring the Ti-K, Ti-L and/or the

N-K signals at the maximum power loading of the x-ray source (10 watts) and in a time period of 200 seconds. For the cases where multiple layers exist, two or more of which contain Ti, it is necessary to use the N-K signal, especially if composition measurement is also required. The WDS part of the project, therefore, concentrated on the measurement of N-K, and the discrimination and measurement of Ti-L x rays.

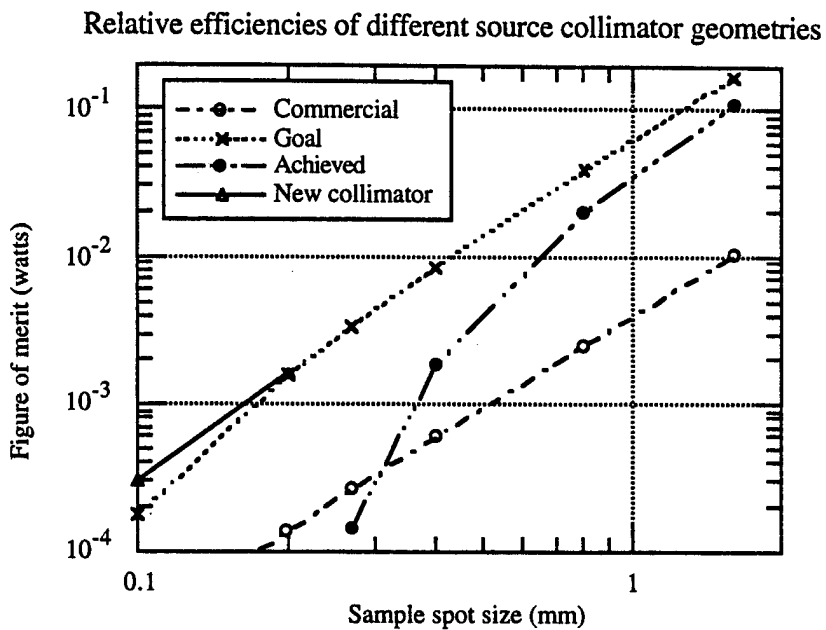


Figure 6.1.1. Comparison of figure of merit for prototype instrument with goal.

This high-efficiency optic should ideally have had a solid angle greater than 0.1 sr, achieved by having multiple large-area WDS channels (up to 5) tuned to the same spectral region. Our initial estimate of the feasibility for making the high-precision N-K measurement was based on Equation 1.3.1.

Three factors contributed to the poor performance achieved during this project. First, budget constraints led to a reduction in scope of the detector and multilayer designs used to implement the WDS, which affected the maximum achievable count rates. A second factor was the low reflectivity of the multilayer mirrors at N-K, which can be attributed to a comparatively large interface roughness for the material combinations used, Monel/Ti and W/Ti. This problem could be remedied by reverting to the use of well-characterized material combinations which are known to perform well in the range of small d-spacings. Finally, an apparent misalignment of the multilayer mirror, with a d-spacing error, precluded the ability to tune the whole multilayer to a single energy, which would have allowed the N-K and Ti-L energies to be distinguished. This problem can, in principle, be corrected by devising a better alignment procedure.

Although the source spot size was larger than expected, this did not affect the calculations for nitrogen detection with an analysis spot size of 1-2 mm. To summarize the results of Section 5.2.4, the as-designed WDS channel only achieved 9% of the predicted throughput capability, and the ability to distinguish N-K and Ti-L was not demonstrated.

While it was desirable to achieve a precision for 400-Å-TiN film, using an analysis spot diameter of 50 μm , it was realized early on that this objective, using either the Ti-L or N-K signals, could only be accomplished by using a comparatively large sample spot diameter of more than 1mm, due to the physical limitations of fluorescence production and detection. For example, given the x-ray tube design specified at the beginning of the project, the goal of a 0.25% precision in 200 seconds could be restated in terms of the net count rate required at the detector. Counting statistics alone required a minimum of $(1/0.0025)^2 = 160,000$ N-K counts in a 200 second period, or 800 counts/second. The predicted N-K fluorescence for a 400 Å TiN film was about 2×10^4 photons/s-W-sr², assuming 10 kV tube excitation. With the smallest available aperture size for the collimator of 37.5 μm , the *total* N-K fluorescence emission from the sample into a hemisphere would be only 68 photons/s, with an analysis spot size of 100 μm . This demonstrated the impossibility of achieving the goal for small spot sizes for very-low-energy XRF, at least using the proposed x-ray tube and spectrometer designs.

Increasing the aperture size to 1 mm, and hence the spot diameter to 1.6 mm, had the effect of increasing the total emitted fluorescence to about 48,000 photons/s. The problem was then to design a wavelength-dispersive spectrometer (required to adequately separate Ti-L and N-K x rays) which could detect 1.7% of the emitted radiation.

To a first approximation, the goal could be accomplished by perfect detection of all the x rays radiated into 1.7% of a hemisphere. However, given the practical limitations of the detector efficiency (initially estimated at 30%) and multilayer reflectivity (initially estimated at 10%) at N-K, this imperfect detection of 3% increased the required collection solid angle to about 56% of a hemisphere, indicating the difficulty of attaining the desired precision.

The next step was to design a single WDS channel, which was compatible with existing instrumentation, to measure the experimental precision. Based on a comparison between our predictions and the actual measurements, we could then extrapolate to a commercial design incorporating multiple WDS channels around the x-ray source. For a 10-watt power loading at 20 kV, our design was initially expected to achieve about 4.6 counts/s (assuming an LSM peak reflectivity of 10%, and a detection efficiency of 30%) at N-K for a 400 Å TiN layer, which translates to the acquisition of about 920 counts and a 3.3% precision for a 200-second counting time ($400 \text{ \AA} \pm 28 \text{ \AA} 1\sigma$). The prototype design occupied a 72° angle in the horizontal plane surrounding the sample, so it was reasoned that a total of 4 identical channels could be

incorporated into a chamber, while preserving space for the Si(Li) detector. The additional channels would increase the count rate proportionally and improve the precision to 1.6%. Although this would not achieve the required precision of at least 1% (or preferably 0.25%), we felt that improvements could be made in terms of the WDS geometry to increase the count rate by a factor of 4. Increasing the tube flux, or increasing the analysis spot size and/or increasing the analysis time could all serve to improve on this precision estimate.

Table 6.1.1 summarizes the key factors in the design and performance of the WDS channel. The column labeled "Ideal" refers to the initial specification designed to meet the most stringent requirement of 0.25% precision. Next, the "Initial Design" column refers to the initial concept layout done on paper. The "Final Design" refers to the design after final iteration with our subcontractor, to produce a working prototype compatible with our existing instrumentation. The "Measured/Predicted" column compares these final design predictions to the actual measured values.

Table 6.1.1. Predicted vs. measured WDS system performance for N-K x rays.

Parameter	Units	Ideal	Initial Design	Final Design	Measured	Measured/Predicted
Relative Source Flux	-	1	1	1	0.58	0.58
Source Solid Angle (1-2 mm spot)	sr	0.02	0.02	0.02	0.03	1.5
Detector Solid Angle	sr	0.42	0.1	0.039	0.019	0.49
LSM Peak Reflectivity	%	10	10	10	4	0.4
d-spacing error	-	-	1	1	0.11	0.11
Detector Efficiency	%	30	30	30	36	1.2
No. Channels	-	5	1	1	1	1
Total						0.022
Factor						45

A combination of the various factors, in the last column of Table 6.1.1, leads to a measured N-K signal level of only 2.2% of the predicted values (about 45x lower) for our prototype system. This means that the actual count rate for N-K, in a 400-Å TiN film, would be about $4.6 * 0.022 = 0.10$ counts/s at 20 kV and 10 W. In Table 5.4.5, we demonstrated a measured count rate of 0.043 counts/s/W at 10 kV for a thick TiN sample. For the 400-Å film, this is expected to translate to a value of $0.043 * (0.91/0.47) * 10/8.5 = 0.10$ counts/s at 20 kV and 10 W, consistent with the value derived from Table 6.1.1. The factor of 8.5 is the predicted ratio of the count rates for a 400-Å TiN film compared with the infinitely-thick film actually measured.

Using both the Si pin diode and Si(Li) EDS detectors, results were much closer to the predicted values. As shown in Figure 5.1.9, the measured count rates for Al and Si were between 0.5 and 2 times the predicted values. These variations can easily be explained by small errors in the tube spectrum models. The thickness of the Mo anode was probably thinner than specified (0.8 vs. 1.5 μm), but this may have been optimal for the analysis of TiN films, especially for the low-energy excitation. Future work on the tube should concentrate on possibly reducing the window thickness, if possible, as well as reducing the anode spot size.

6.2 APPLICATION TO SEMICONDUCTOR MATERIALS' ANALYSIS

6.2.1 Application to TiN Analysis

Despite the problems with background signal and multilayer misalignment, the projected precision of 3.3% for a 400- \AA -TiN film still seems plausible using our single-channel WDS prototype. There is reason to believe that correct alignment of the multilayer, the choice of a higher-reflectivity multilayer combination, and an improved detector design to reduce sensitivity to high energy x-rays, will improve the N-K count rate to better than 1 count/s. On the other hand, residual background levels (e.g., from Si-L) under the N-K peak will tend to somewhat decrease the precision.

However, as far as the EDS measurements were concerned, we met the expected goals in terms of precision. In this case, we used the Ti-K signal to calibrate and predict the thickness of TiN thin films, assuming that the TiN stoichiometry is constant. This is the procedure used presently, by XRF instrumentation, for process monitoring of these films immediately after their fabrication. These results are discussed further in Section 6.2.2.

6.2.2 Quantitative TiN Thin-Film Analysis

To test the performance of the system, for a real application, we used some thin-film TiN-on-Si-wafer standards kindly loaned to us by Intel Corporation (Santa Clara, CA). They provided three TiN standards with unknown composition, but with thicknesses determined by RBS (Rutherford Back-Scattering). These were analyzed using the energy-dispersive spectrometer, by analyzing the Ti-K signals, assuming the TiN composition to be consistent. The EDS spectra were acquired at 15 kV and 0.04 mA, for 100 (live-time) seconds each. The spectra were acquired in air to help suppress the Si count rate compared with the Ti count rate. Because an EDS detector and electronics are often operating in count-rate limited mode, one way to increase the signal of the analyte of interest is to filter out sections of the spectrum which are not of interest, and also tune the excitation conditions to preferentially excite certain analytes. The choice of 15 kV and the air atmosphere both contribute to preferentially detecting Ti-K x-ray lines, at the expense of Si-K lines from the substrate. This detector was particularly sensitive to low-energy x rays, because of the

thin window. The use of an aluminum filter would have improved the Ti/Si ratio even further, and would contribute to improving the precision.

The acquired spectra were processed with the IXRF software, which can automatically remove the background, and extract intensities by either simple peak integration or by fitting theoretical Gaussian peak profiles to all the lines for the selected element line series (e.g., Ti-K and Si-K). Because these films were extremely thin, self-absorption effects are minimal and all the intensity values fell on a linear plot through an origin of (0, 0). The titanium/silicon peak intensity ratios were also calculated. Often, for linear systems, there is an advantage in using peak ratios, because the ratio is usually independent of the tube flux (assuming any variations are due to current fluctuation, not voltage). This is important as it avoids the necessity of frequent recalibration. To monitor long-term behavior, a standard would normally be run with any unknown samples, to provide statistical quality control.

The net intensities and thickness values are shown in Table 6.2.1. A plot of count rate against film thickness is shown in Figure 6.2.1. A linear least-squares fit was made to the data points (constrained to pass through the origin), and calculated thickness "LS" tabulated against input values. Also, one of the samples was used as a calibration standard for the Fundamental-Parameter (FP) software. This software makes corrections for the physics interactions within the thin films. As stated previously, these effects are small for these films, but it provides another independent check of accuracy of the technique. The calculated values "FP" for the other two samples are also shown in Table 6.2.1. The calculated thickness are within the expected accuracy based upon counting statistics.

Table 6.2.1. Analysis of Intel TiN standards.

Given Thickness (nm)	Ti-K intensity (c/s)	Si-K intensity (c/s)	LS Thickness (nm)	FP Thickness (nm)
64.0	505	3493	63.8	Standard
86.0	687	3368	86.8	87.2
109.0	860	3192	108.6	110.2

In another series of tests, the absolute count-rate performance of the new instrument was measured, for the analysis of the TiN thin film which was 109-nm thick. The main purpose here was to determine the gain in flux compared to other commercial instrumentation. The count rates of Ti-K α and Si-K x rays were measured at different values of the excitation voltage (kV). These were measured with tube serial number 2, which had a spot size diameter of about 0.8 mm, which projected through a 1-mm collimator produced a spot size of about 1.2 mm. A similar, but not identical, TiN film (with a thickness of 112 nm) was measured on a commercial XRF (the Kevex Omicron) spectrometer at Intel Corporation, which had a an elliptical spot size, with major and

minor axes of 2.8 and 2.0 mm respectively. The Omicron spectra were acquired in vacuo (with a beryllium-window detector), and our results were obtained in air. However this should not affect significantly the results, although the titanium signal will be slightly attenuated in air. The Ti/Si ratios will be very different, of course, but since the count rates were normalized with respect to current (mA) this does not affect the results. The results were normalized, for comparison, by converting the count rates to counts per second per mA per mm^2 (analysis spot size) per nm film thickness (for these thin films the count rate is linear with thickness, as per Figure 6.2.1). The results are shown in Table 6.2.2:

Table 6.2.2. Measured count rates of Ti-K in TiN thin films on silicon.

kV	mA	Ti-K (c/s)	Si-K (c/s)	Flux c/s/mA/nm/mm ²	Omicron c/s/mA/nm/mm ²
10	0.10	842	4274	68	7.6
20	0.05	1413	4168	229	22.3

The value of 229 for the normalized count rate at 20 kV compares with a value of 22.3 on the Omicron spectrometer, which is equivalent to a gain of 10.3 in flux per unit area per mA. Similarly at 10 kV, there is a gain of about 8.9 in flux per unit area per mA. These values are close to the expected gains (agreeing with those in Figure 6.1.1), and would be twice as much if we had the 0.10 steradians available (as originally specified) in our EDS detector.

A stability run was also made using one of the TiN samples (thickness 86 nm). About 330 measurements were made, in sequence, with 100 seconds acquisition per point. The variation in the Ti-K counts is shown in Figure 6.2.2. The average Ti-K counts in 100 seconds were 125,890. The 1-sigma standard deviation of 375 counts is close to the theoretical standard deviation (based on Poisson statistics) of 355 counts. This translates to a relative standard deviation of 0.3%, and an equivalent thickness variation of 0.26 nm, which is within the requirements of the semiconductor industry (typically less than 1% relative for TiN).

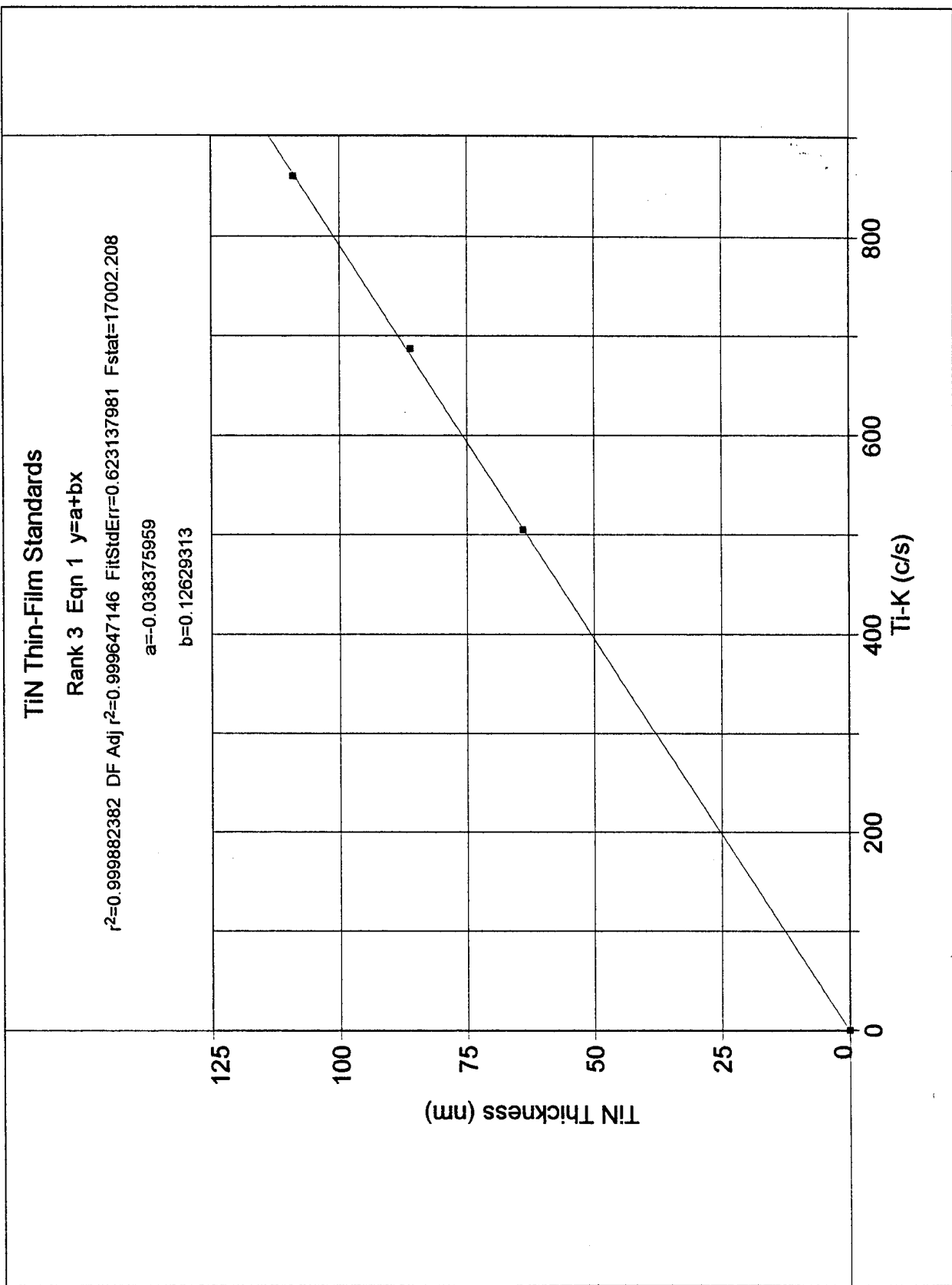


Figure 6.2.1. Plot of Ti-K count rate against TiN film thickness.

TiN/Si Stability Run

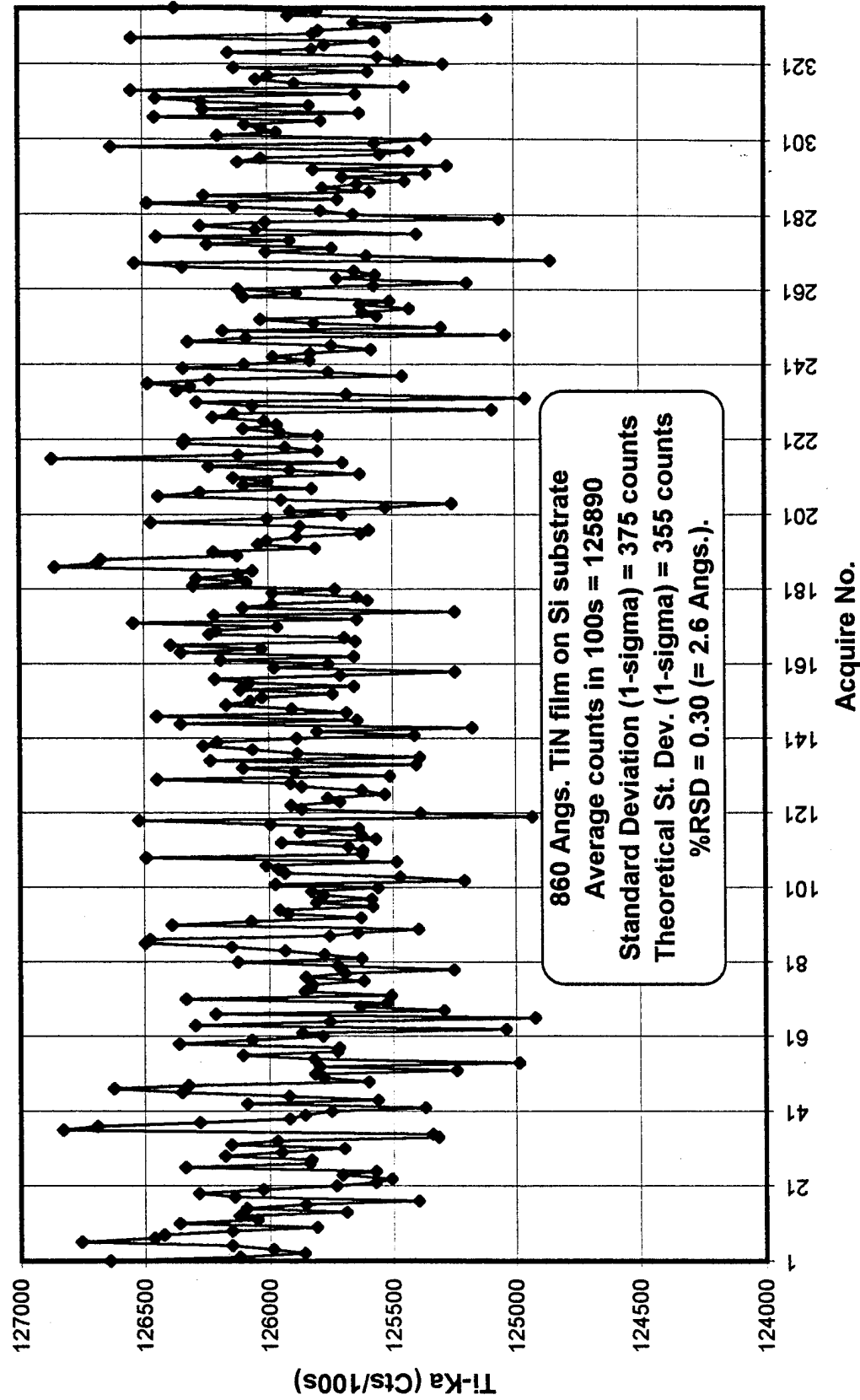


Figure 6.2.2. TiN/Si repeatability measurements.

7.0 CONCLUSIONS AND RECOMMENDATIONS

We have analyzed the detailed requirements for composition and film-thickness measurement for semiconductor thin films. The requirements for smaller analysis spot sizes, higher flux sources, light-element analysis and high-throughput analysis, were used to drive the specifications of a prototype instrument to test the actual performance realizable in practice. The prototype instrument was actually a collection of three different prototype sub-assemblies with a newly designed close-coupled geometry of source, sample and spectrometers. The three prototype items were (a) a new low-power thin-window transmission-target x-ray tube, (b) a new design of focusing wavelength-dispersive spectrometer, with limited scanning capabilities, and (c) a new Si(Li) detector for low-energy x-ray fluorescence.

The main conclusions and recommendations from this work are as follows:

- We successfully demonstrated the expected flux performance from the transmission-target x-ray tube. Further refinements could include: (a) tuning the ideal thickness of the transmission-target material (Mo) and reducing the window (Be) thickness, for the optimum excitation of low-energy x-ray fluorescence. On a per watt basis, we were able to demonstrate a figure-of-merit increase of performance of a factor of 10 over the best commercial instrument currently available.
- We successfully demonstrated that passive cooling was sufficient for this design and power of x-ray tube. The local temperatures, near the target, did not exceed 36 °C. Further work is only needed here, if the spot-size reduction causes stress damage to the target/window material.
- We did not demonstrate the goal of a spot size on the tube anode of 150 μm . The smallest spot size we produced was about 0.8 mm. A top priority for future should address this issue, while maintaining sufficient brilliance to generate the fluorescent count rates required for semiconductor thin-film analysis. Also, further work needs to be done to optimize the collimator design and minimize the spot dimensions on the sample.
- The combined tube, power supply and detection systems were sufficiently stable to meet at least the short-term repeatability requirements of the semiconductor industry. Analysis over a 16-hour period demonstrated a 0.25% 1σ precision.
- We evaluated and fabricated several multilayer candidates for the focusing optic for a WDS channel. Although the peak reflectivity is low for N-K x rays, the materials have the potential to meet the requirements for both N-K and Ti-L x-ray analysis on a single WDS

unit. Further work is required to fully characterize the material properties and deposition procedures used, to improve the multilayer reflectivity.

- We did not demonstrate the required efficiency for the WDS unit, to be able to meet the predictions of this design. We were a factor of about 45 lower than the predicted performance for this design. We believe this is because of: (a) a multilayer reflectivity which was 40% of the predicted value, (b) a d-spacing error which reduced the performance by about a factor of 10, and (c) a geometric alignment error which caused the N-K x rays to only be “seen” by 50% of the mirror. However, further work is needed to fully characterize these findings, and provide optimal solutions. Also, background signal levels were higher than expected, which will also require further work to characterize and reduce. We still believe that four WDS channels will be required to meet the needs of industry for TiN analysis.
- The Si(Li) detector, and associated electronics, performed close to expectation. The main deviation of the available solid angle could be recouped by modifying the end cap, and using a newer x-ray transmissive window (boron hydride) which does not require a grid support structure. Future systems should consider the alternative of an HPGe detector, if liquid nitrogen can be used as the coolant. For environments where liquid nitrogen is problematic, then consideration should be given to either Si(Li) detectors with Peltier cooling or other less-expensive solutions such as silicon PIN diodes and similar detectors.

Other more general recommendations for future development of this instrument should include a general engineering overhaul of the design to optimize geometries and improve the manufacturability. Also, other features such as optical viewing of the sample, computerized sample motion, wafer handling options (robotics, clean-room compatibility), and user interface software need to be added to complete a full engineering demonstration of the instrument.

8.0 REFERENCES

Armagliato, A., Dori, L., Garulli, A., and Venturi, P., "X-ray microanalysis of nitrogen in the presence of titanium with an automated electron microprobe," *J. Microsc. Spectrosc. Electron.*, 7, 593 (1982).

de Boer, D.K.G., "Calculation of X-Ray Fluorescence Intensities from Bulk and Multilayer Samples," *X-Ray Spectrometry* 19, 145 (1990).

Boher, P., Houdy, P., Kuhne, P., Muller, P., Barchewitz, R., Delaboudiniere, J. P., and Smith, D.J., "Tungsten/Magnesium Silicide Multilayers for Soft X-Ray Optics," *J. X-ray Sci. and Tech.*, 3(2), 118 (1992).

Bull, H.B., "An Introduction to Physical Biochemistry," p.71, F.A.Davis Co., Philadelphia, 2nd Ed., (1971).

Carpenter, D.A., and Taylor, M.A., "Fast, High-Resolution X-Ray Microfluorescence Imaging," *Adv. X-Ray Analysis*, 34, 217 (1991).

Christensen, F.E., Shou-Hua, Z., Hornstrup, A., Schnopper, H.W., Plag, P., and Wood, J., "X-Ray Study of State-of-the-Art Small d-Spacing W/B₄C Multilayers," *J. X-ray Sci. and Tech.*, 3(1), 1 (1991).

Condon, E.U., "Heat Transfer," in *Handbook of Physics*, p.5-62 (ed. Condon, E.U. and Odishaw, H.) McGraw-Hill, New York, 2nd Ed., (1967).

Cross, B.J., and Wherry, D.C., "X-ray microfluorescence analyzer for multilayer metal films," *Thin Solid Films* 166, 263 (1988).

Diebold, A. et al. "Metrology Roadmap: Supplement to the Semiconductor Industry Association Roadmap," (1995).

Davis, C., Moslehi, M.M., Bowling, A., and Luttmer, J.D., "Microelectronics Manufacturing Science and Technology: Equipment and Sensor Technologies," *Texas Instr. J.*, 9(5), 20 (1992).

Doering, R. R., "The MMST program: An overview," *Solid State Technology* 37(1), 31 (Jan. 1994).

Dyson, N.A., "X-rays in atomic and nuclear physics," p.316, Longman Group Limited, London, (1973).

Feng, L., Cross, B.J., and Wong, R., "New developments in FP-based software for both bulk and thin-film XRF analysis," *Adv. X-Ray Analysis*, 35, 703 (1992).

Fiori, C.E., Swyt, C.R., and Myklebust, R.L., "Desktop Spectrum Analyzer V2.0.1," NIST, Gaithersburg, MD 20899, (1993).

Franco, E.D., et al., "Microelectronics Cluster Tool Sensor Development," Final Report for ARPA contract # DAAH01-91-C-R155 (1992).

Herglotz, H.K., and Reilly, C.D., "X-ray generator having an anode formed by a solid block with a conical bore closed by a target foil," U.S. Patent # 3,584,219 (1971).

Henke, B.L., Gullikson, E.M., Kerner, J., Oren, A.L., and Blake, R.L., "Design and characterization of x-ray multilayer analyzers for the 50-1000 eV region," *J. X-ray Sci. and Tech.*, 2, 17 (1990).

Henke, B.L., Gullikson, E.M., and Davis, J.C., "X-ray Interactions: Photoabsorption, Scattering, Transmission, and Reflection at $E = 50 - 30,000$ eV, $Z = 1-92$," *Atomic Data and Nuclear Data Tables*, 54(2), 181 (1993).

Herglotz, H.K., "Miniature X-Ray Equipment for Diffraction and Fluorescence Analysis," *Ad. X-Ray Analysis*, 16, 260 (1973).

Hershyn, W., "Thin-target x-ray tubes for elemental analysis," *Res./Dev. Mag.*, 26(8), 32 (1975).

Hoffman, S.A., Thiel, D.J., and Bilderback, D.H., "Applications of single tapered glass capillaries: submicrometer x-ray imaging and Laue diffraction," *Optical Engineering* 33(1), 303 (1994).

Holliday, J.E., "Soft X-Ray Emission Bands and Bonding for Transition Metals, Solutions and Compounds," in *Soft X-Ray Band Spectra* (Ed. D.J. Fabian), p.126, Academic Press, New York (1968).

Holman, J.P., "Heat Transfer," p. 253, McGraw-Hill, New York, 4th Ed., (1976).

Huber, A.C., Pantazis, J.A., and Jordanov, V.T., "High Performance, Thermoelectrically Cooled X-Ray and Gamma Ray Detectors," paper presented Intl. Conf. Application of Accelerators in Research and Industry, Denton, TX (Nov. 1994).

Huang, T.C., "Thin-Film Characterization by X-Ray Fluorescence," *X-Ray Spectrometry* 20, 29 (1991).

Kevex Semicron brochure, Fisons Instruments, Valencia, CA (1994).

Kirby, R.E., Wherry, D., and Madden, M., "Low Energy X-Ray Fluorescence Spectrometry," *J. Vac. Sci. Technol.*, A11, 2687 (1993).

Madden, M.C., and Cox, J.N., "High precision measurement of phosphorus in thin glass films using x-ray fluorescence," SPIE Vol. 1186 "Surface and Interface Analysis of Microelectronic Materials Processing and Growth," p.22 (1989).

Maissel, L.I. and Glang, R., "Handbook of Thin Film Technology," McGraw-Hill, New York, (1970).

Marshall, G.F., "Monochromatization by multilayered optics on a cylindrical reflector and on an ellipsoidal focusing ring," *Optical Engineering* 25(8), 922 (1986).

McMaster, W.H., Del Grande, N.K., Mallett, J.H., and Hubbell, J.H., "Compilation of X-Ray Cross Sections," UCRL-50174 Sec. II Rev. 1, Lawrence Radiation Laboratory (1969).

Moslehi, M.M., et al., "Single-wafer processing tools for agile semiconductor production," *Solid State Technology* 37(1), 35 (Jan. 1994).

Pantazis, J., Huber, A., Okun, P., Squillante, M.R., Waer, P., and Entine, G., "New, High Performance Nuclear Spectroscopy System using Si-PIN Diodes and CdTe Detectors," *IEEE Transactions Nuclear Science*, 41(4), 1004 (1994).

Powell, R.L. and Childs, G.E., Thermal Conductivity, in *American Institute of Physics Handbook*, p.4-154, (ed. Zemansky, M.W.) McGraw-Hill, New York, 3rd Ed., (1972).

Rybka, R. and Wolf, R. C., "Application of layered synthetic microstructured crystals for WDX microanalysis of ultra-light elements," Proc. 27th Microbeam Analysis Society Meeting, Los Angeles, CA, S190, (1993).

Sareen, R.A., "Developments in X-Ray Detectors and Associated Electronics: A Review of the Technology and Possible Future Trends," *J. X-Ray Sci. & Tech.*, 4, 151 (1994).

Savage, D.E., Kleiner, J., Schimke, N., Phang, Y.-H., Jankowski, T., Jacobs, J., Kariotic, R., and Lagally, M.G., "Determination of roughness correlations in multilayer films for x-ray mirrors," *J. Appl. Phys.*, 69(3), 1411 (1991).

Schuster, M., and Gobel, H., "Parallel-beam coupling into channel-cut monochromators using curved graded multilayers," *J. Phys. D: Appl. Phys.* 28, A270 (1995).

Spiller, E., and Rosenbluth, A.E., "Determination of thickness errors and boundary roughness from measured performance of a multilayer coating," *SPIE 563, Applications of Thin-Film Multilayered Structures to Figured X-Ray Optics*, 221 (1985).

Stull, D.R., "Vapor Pressure, in American Institute of Physics Handbook," p.4-315, (ed. Zemansky, M.W.) McGraw-Hill, New York, 3rd Ed., (1972).

Takacs, P.Z. and Church, E.L., "Figure and finish of grazing-incidence mirrors," *Nucl. Instr. Meth.* A291, 253 (1990).

Toda, K., Kohno, H., Arai, T., Araki, Y., Hamili, G., "Sensitivity improvement and stabilization for ultra light element analysis by x-ray spectrometry," *Adv. X-Ray Analysis*, 37, 629 (1994).

Underwood, J.H. and Barbee, Jr., T.W., "Synthetic Multilayers as Bragg Diffractors for X-Rays and Extreme Ultraviolet: Calculations of Performance," p.170, in *Low Energy X-ray Diagnostics*, AIP Conf. Proc., Monterey, CA (1981).

Vrebos, B.A.R., and Kuiper, G.T.J., "Areas for improvement in XRF analysis of low atomic number elements," *Adv. X-Ray Analysis*, 36, 73 (1993).

Zaitz, M-A., "Small area x-ray fluorescence analysis of multilayer thin metal films," *Adv. X-Ray Analysis* 37, 219 (1994).

Zulliger, H.R., and Stewart, J.R., "X-ray Fluorescence Analysis with Transmission-Target Tubes," *Adv. X-Ray Analysis* 18, 278 (1975).